Technische Universität München
Fakultät für Elektrotechnik und Informationstechnik

Control, monitoring and management of a WDM-PON using pilot tones

Dipl.-Ing. Markus Roppelt

Vollständiger Abdruck der von der Fakultät für Elektrotechnik und Informationstechnik der Technischen Universität München zur Erlangung des akademischen Grades eines

Doktor-Ingenieurs (Dr.-Ing.)

genehmigten Dissertation.

Vorsitzender:		Univ.-Prof. Dr.-Ing. habil. Erwin Biebl
Prüfer der Dissertation:	1.	Univ.-Prof. Dr.-Ing. Norbert Hanik
	2.	Priv.-Doz. Dr.-Ing. Stephan Pachnicke Technische Universität Dortmund

Die Dissertation wurde am 17.10.2013 bei der Technischen Universität München eingereicht und durch die Fakultät für Elektrotechnik und Informationstechnik am 30.01.2014 angenommen.

Abstract

Future access technologies require higher bandwidth than today's technologies. A promising candidate to full-fill this requirement is wavelength division multiplexing (WDM)-passive optical network (PON). This work describes how the usage of pilot tones enables the development a low-cost WDM-PON.

In this thesis, a new pilot tone generation method, which is based on a modified 8B/10B encoder, is introduced. The new generation scheme is experimentally demonstrated using a field programmable gate array (FPGA), and its performance is compared to existing generation methods.

Then, a centralised network wavelength control using individual pilot tones is presented which allows a optical network unit (ONU) to tune itself to its target channel. The centralised network wavelength control allows to remove the wavelength reference (etalon) from all ONUs and thus to reduce the overall costs.

Further cost savings on the ONU side can be gained by omitting the thermoelectric cooler (TEC) and reducing the calibration effort. Instead, generic equations and/or interpolation of the calibration data can be used. The work explains how the two concepts can be applied to two different laser types: Digital supermode - distributed Bragg reflector (DS-DBR) lasers and sampled grating Y-branch (SG-Y) lasers. Both concepts can also be used with the former introduced centralised network wavelength control and will subsequently also be experimentally demonstrated jointly.

Finally, a new method incorporating a second wavelength reference (etalon) is introduced. The new method provides a large lock-in range of an arbitrary target channel frequency. The theory of the new method is explained, and its usage will be demonstrated. This grid-less wavelength locking is not limited to access networks can be used in several application, e.g. flexgrid with a very small channel spacing.

Acknowledgement of public funding

The research leading to these results has received funding from the German ministry for education and research (BMBF - Bundesministerium für Bildung und Forschung) under Grant 13N10864 (ADVAntage-PON) and from the European Community's Seventh Framework Program (FP7/2007-2013) under grant agreement 249025 (ICT-OASE).

Contents

1 Introduction

1.1 Passive optical networks

Today, telecommunications networks can be roughly divided into three main parts: core, metro and access networks. In the core network, also called backbone, the high-speed wavelength division multiplexing (WDM) equipment is used. Then, towards the end user, metro systems are used to aggregate the traffic from different locations for transmission in the core network. Finally, within the access part, end-user connectivity is established. Passive optical networks (PONs) are used as residential access technology to provide this end-user connectivity. PONs are seen as a future replacement for xDSL variants, e.g., asymmetric digital subscriber line (ADSL) and very-high-bit-rate digital subscriber line (VDSL), and also as a replacement coaxial television (TV) cable networks., e.g., Data Over Cable Service Interface Specification (DOCSIS).

1.1.1 Basic terminology

In a passive optical network, several users are connected to a central point via a single fibre. This point-to-multi-point (P2MP) architecture allows service providers to share a part of the fibre plant between various users. The shared part is called feeder fibre, and the part running to each user is called drop-line or distribution fibre. Finally, in the remote node (RN), the two parts are connected together, see Figure 1.1a. Together, feeder fibre, distribution fibre and the remote node, are called optical distribution network (ODN). The terminus passive in PON means that no active powered equipment is used in the outside plant between the central office (CO) and the optical network units (ONUs). ONUs are also called customer premises equipment (CPE). According to ITU G.983.1, see [1], the term optical network termination (ONT) is only used when the optical network part is terminated on the costumer premises (FTTH) and the term ONU is used when the device provides (directly or remotely) a user-side interface of the ODN. Within this work the term ONU will refer to both ONTs and ONUs. Depending on how far the fibre reaches into the network, different names, which all follow the naming scheme "fibre-to-the-X", can be used:

- Fibre-to-the-business / building (FTTB)
- Fibre-to-the-curb (FTTC)
- Fibre-to-the-cabinet (FTTCab)
- Fibre-to-the-home (FTTH)
- Fibre-to-the-node / neighbourhood (FTTN)
- Fibre-to-the-premises, includes FTTH and FTTB (FTTP).

Figure 1.1b shows FTTCab, FTTC, FTTB and FTTH. For FTTCab and FTTC, the last mile to the costumer is realised via a copper line, with technologies like xDSL or hybrid fibre coax (HFC). In these two cases, it is common that multiple network terminations (NT) are connected to a single ONU. In FTTH and FTTB, however, the fibre runs to costumer home. Either the ONU sits in the basement (FTTB), or the distribution fibre is running directly to the room where the end device is located. Note that no exact separation as when to use which FTTX naming variant exists. The same deployment can have different names for different operators.

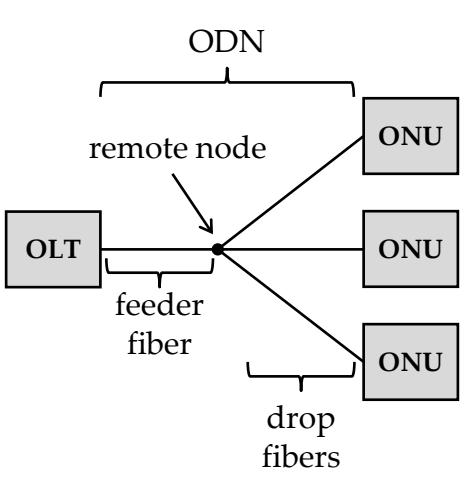

(a) Basic PON architecture

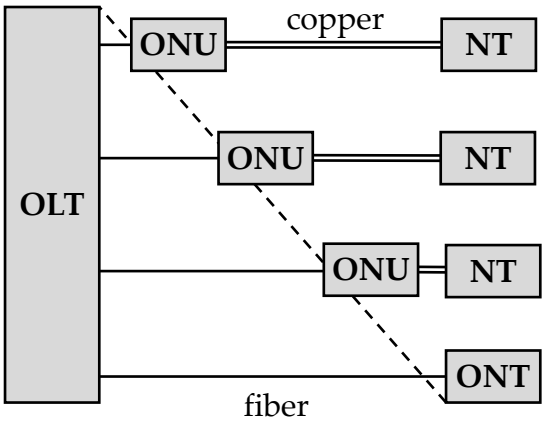

(b) FTTX in the access part of a network from top to bottom: FTTCab, FTTC, FTTB, FTTH

Figure 1.1: Basic PON architecture and FTTX in the access part

1.1.2 Bandwidth demand

Residential access bandwidth has been increasing in the past for 30 years. This effect of continuous bandwidth growth has been described by Nielson [2], who made a prediction that residential access speeds will grow by 50% per year. This prediction is often compared

to Moore's law for the number of transistors on integrated circuits. The exponential growth can be seen from Figure 1.2 and was true from the late 1980s until now. Also today, no change of this growth in demand can be seen as future services can easily fill bandwidths in excess of 100 Mb/s. One of today's key bandwidth drivers is high-definition video streaming, see [3]. Therefore, it can be foreseen that also currently deployed systems will reach their limits and won't be capable of delivering the future services.

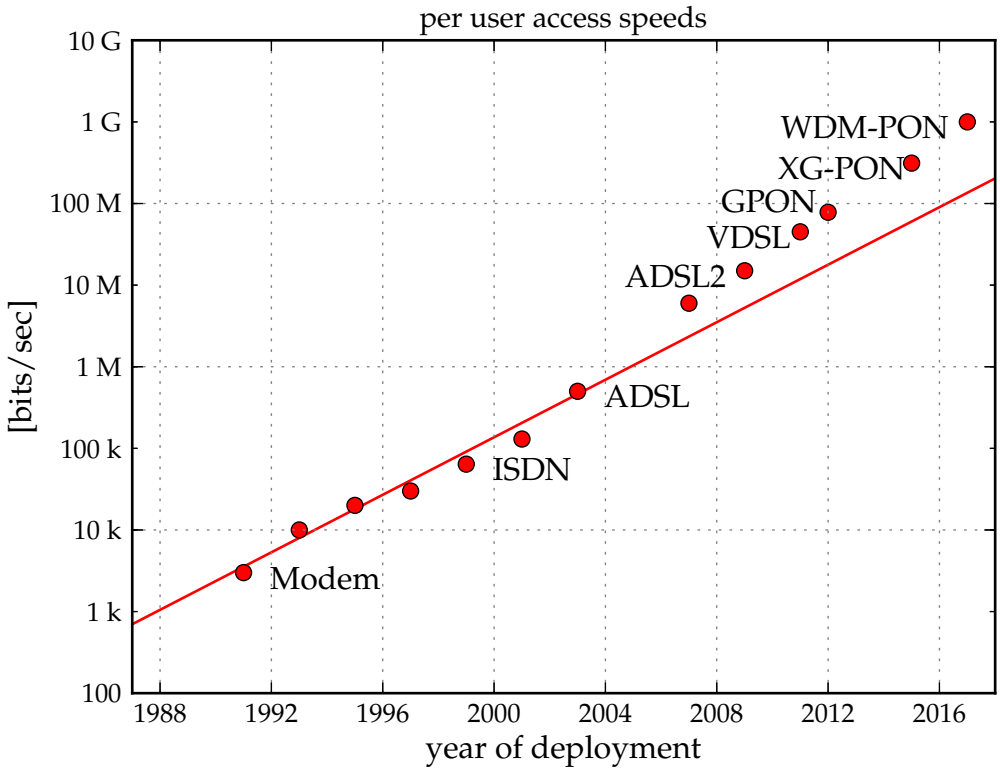

Figure 1.2: Nielsen's Law of Internet Bandwidth [2] growth with technologies enabling these speeds (uncontended bandwidth) and showing a growth of 50% per year

1.2 PON systems

In the literature, many different PON systems have been proposed: optical code division multiple access (OCDMA)-PON [4], orthogonal frequency-division multiple access (OFDMA)-PON [5], space division multiplexing (SDM)-PON [6], frequency division multiplexing (FDM)-PON [6], WDM-PON [7], and finally many variants of the standardized time division multiple access (TDMA)-PON. Figure 1.3 gives an overview of

the most relevant variants which use a passive fibre infrastructure, structured by remote node design, technology and realisation. Currently, three approaches are commercially pursued: TDM-, WDM- and Hybrid-PONs. Therefore, these three main variants for a next generation optical access (NGOA) network are described hereinafter and marked with a bold frame in Figure 1.3.

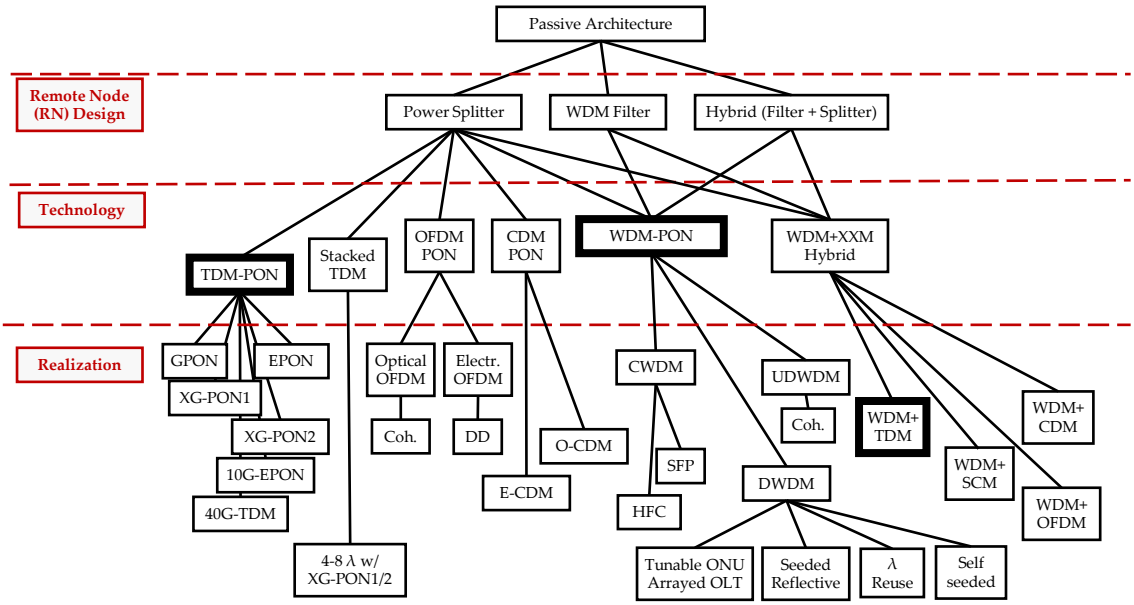

Figure 1.3: System concepts NGOA networks with passive fibre infrastructure, based on [8].

1.2.1 TDMA systems

Today, mainly Ethernet PON (EPON) [9] and Gigabit PON (GPON) [10] systems are deployed, see [11]. Both systems are based on TDMA, use a power splitter in the remote node and are single fibre working (SFW) systems. In order to distinguish the traffic between different ONUs in downstream direction, the OLT always sends packet containing information to which ONU the packet is addressed. Every downstream packets is received by all ONUs, but only the ONU with the matching target address processes the packets. In upstream direction, the ONUs cannot send continuously because simultaneous transmission of two or more ONUs would result in uncorrectable errors at the OLT. Instead, the OLT attributes time slots for each ONU when it is allowed to send. The rest of the time, the ONU laser has to be turned off. See Figure 1.4a for the attribution of time slots to different ONUs. For a complete explication of the media access protocol for GPON, see [10], [12]. The power splitter in the remote node can have splitting ratios up 1:128. Alternatively, topologies with two stages are possible, e.g. in the first stage

a 1:8 splitter followed by 8 power splitters each again having 1:8 split. This two-stage topology then allows to aggregate a total of 64 ONUs on one feeder fibre. Depending on the splitting ratio and the fibre length, the optical line budget from the OLT to the ONUs is different. A higher system budget results in higher component costs. In order not to use over-dimensioned and thus too expensive components for deployments with a low system budget, different reach classes have been defined. For GPON, ODN losses between 28 and 32 dB have been standardized in ITU G.984.2, see [10].

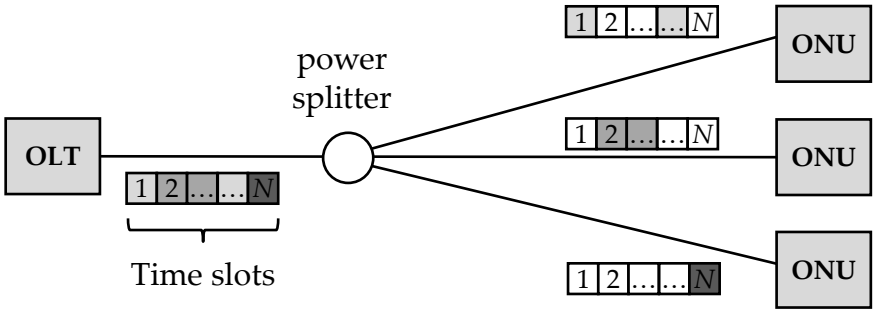

(a) Power split TDMA-PON

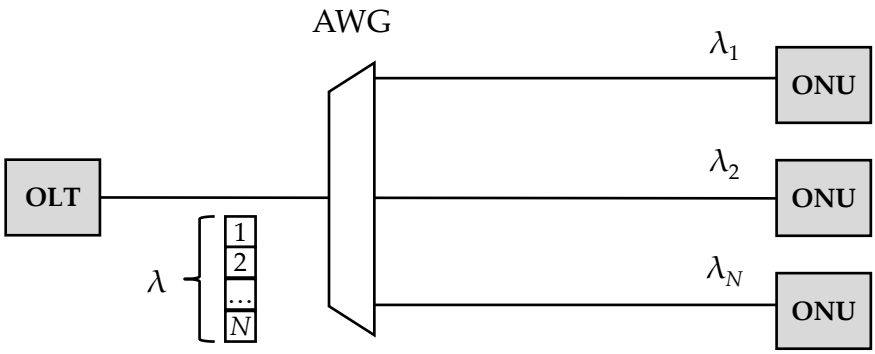

(b) WDMA-PON with an AWG in the RN

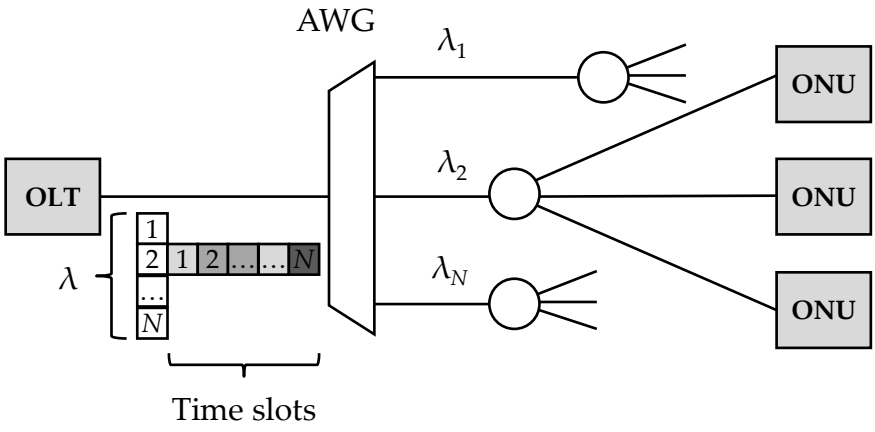

(c) Hybrid WDM-TDMA-PON with an AWG in the RN

Figure 1.4: PON systems: a) TDMA-PON, b) WDMA-PON, c) WDM-TDMA-PON

The OLT sends packets at a specific line rate (physical layer gross bit rate). Table 1.1 shows the line rates of various standardized PON systems. An ONU continuously receives all packets from the OLT and only processes the packets addressed to itself. In TDMA systems, as in all shared media systems, the maximal downstream (DS) and upstream (US) data transfer rate (commonly known as bit rate) is available for every ONU, however not at the same time. In the highest demand case, in which all ONUs want to have the maximal data transfer rate, the resulting data transfer rate for one ONU is the line rate divided by the numbers of ONUs connected to the same OLT. Note the final throughput payload data rate an ONU can obtain is lower then the data transfer rate due to the overhead data in the frames. All standardised TDMA systems have a complex protocol frame with a, compared to standard Ethernet, large overhead.

The average data transfer rate, also called bandwidth, for a single ONU is subject to bandwidth allocation and fairness rules which are implemented in the OLT. Using prioritisation and scheduling, the available bandwidth can be attributed dynamically between different ONUs, which is an advantage for lower line rates (up to 10 Gbit/s). However the burst property is not desirable when increasing the total throughput rate, e.g., to 40 Gbit/s, as all ONUs need to be running at this speed, which implies high cost.

standard	max. downstream line rate	max. upstream line rate [Gbit/s]	
	Gbit/s	normal	alternative
BPON [1]	0.622	0.155	
1G-EPON [9]	1.25	1.25	
GPON [10]	2.5	1.25	2.5
XG-PON [13]	9.95	2.5	5.0
10G-EPON [14]	10.31	10.31	1.0

Table 1.1: Parameters of TDMA-PON standards

1.2.2 WDM-PON

In a WDM-PON, the ONUs are addressed by different wavelengths. In most configurations, an arrayed waveguide grating (AWG) is installed in the RN, see Figure 1.4b, however, it also possible to design a system with a power splitter in the RN. If an AWG is used, the system is called wavelength routed (WR)-WDM-PON and if a power splitter is used, it is called a wavelength selected (WS)-WDM-PON. In a WR-WDM-PON, the wavelengths in downstream direction are separated by the AWG, see Figure 1.5. Each ONU then only receives one wavelength. In a WS-WDM-PON, every ONU receives the complete spectrum and must filter out the attributed channel. This can be done

either by a tunable filter, see [15], or by coherent detection, see [16]. In the following, mainly WR-WDM-PONs will be considered because of the lower insertion loss (IL) of the AWG and the immaturity of low-cost tunable filter techniques. The lower insertion loss is achieved because the AWG demultiplexes the different downstream channels in the wavelength domain. Today's 40-port modules have IL $<\sim$6 dB as compared to 32-port power splitters with $\sim$16-17 dB. Due to this lower IL, a WR-WDM-PON allows longer distances, or the same distances can be achieved by components with less demanding requirements which lead to cheaper components.

Athermal AWG

As described before, the RN with the AWG is normally placed in the outside plant where no energy supply is available or wanted, and thus no temperature control can be provided. Therefore it is important that the AWG can work properly within a temperature range for outdoor components, e.g., -40...+85°C for the so-called "extended industrial range". There are also other temperature ranges depending on the application, e.g., "commercial grade" is -20...+55°C and "military grade" is -55...+125 °C. Athermalization can be achieved by different methods, see [17] for an overview.

The spectral distance of two refractive orders of an AWG filter is described by the free spectral range (FSR). In different orders of the AWG, the channel spacing isn't equal and normally the C-Band is fixed to 100 GHz. The other refractive orders have slightly larger / smaller channel spacings which are not "on grid" any more with respect to the nominal 100-GHz ITU-T wavelength grid, which is defined in [18]. This offset to the ITU-T wavelength grid is depending on the technology and the design parameters of the AWG and can be expressed by

$$\frac{\text{grid}(n)}{\text{grid}(n+1)} = \frac{f_0}{f_0 + FSR} \tag{1.1}$$

with the grid being defined in Hz and f_0 the frequency in the C-band.

In order to have a common grid between different vendors ITU-T recently approved ITU-T G.698.3, see [19], which defines a channel grid of 100 GHz in the C-band and 97.15 GHz in the L-Band. Table 1.2 shows the low measured insertion loss of several refractive orders, and Table 1.3 shows the athermalization. Both measurements have been done with commercially available AWGs. It can be seen from the measurements that up to 10 orders can be used with low insertion loss, and also that the temperature range is large. This enables use of further orders for additional services which is called multi-band usage. It should also be noted that the extension of the AWG from 40 ports at 100 GHz to

80 ports at 50 GHz will only add small additional insertion loss (∼1 dB additional).

Order	Band	Channel grid [GHz]	Wavelength [nm]	Typ. IL [dB]
−2	U	94.7	1616 - 1642	4.01
−1	L	97.3	1574 - 1599	4.01
0	C	100	1533 - 1558	4.24
1	S	102.5	1494 - 1519	4.27
...				
7	O	118	1299 - 1320	4.02

Table 1.2: Measurement results of a 32-port athermalized AWG incl. connectors

Temperature	Insertion Loss [dB]		
	Min.	Max.	variation
−40	4.072	4.862	0.789
0	3.873	4.369	0.495
40	3.773	4.291	0.518
80	4.276	4.818	0.541

Table 1.3: Measurement results of a 40-port athermalized AWG according to ITU-T G.698.3 [19] over all ports in C-Band (195.9 - 192.0 THz) incl. connectors

WDM-PON with reflective transmitters

In a wavelength-seeded reflective WDM-PON, the upstream optical carrier for all ONUs is generated at the OLT and sent toward the ONU, where the carrier is modulated by a reflective optical device. For this task, either a reflective semiconductor optical amplifier (RSOA), a reflective electro-absorption modulator (REAM) or an injection-locked Fabry-Perot laser diode (IL-FPLD) can be used. It also possible to have mixed devices, e.g. a REAM-semiconductor optical amplifier (SOA)

In order to completely remove the downstream modulation from the upstream traffic, the reflective device must be operated in the saturation regime [20], which leads to power budget limitations. Several publications propose solutions to overcome this limitation: reducing the downstream modulation-index [21], alternating continuous wave (CW) light with modulated data slot [22], broadband light source seeding from the OLT [23], and also applying a special optical line coding for down- and upstream [24]–[26]. Various technology options are available as a seed source: broadband light sources (BLSs) like a light emitting diode (LED) or an erbium doped fibre amplifier (EDFA) can be used, which

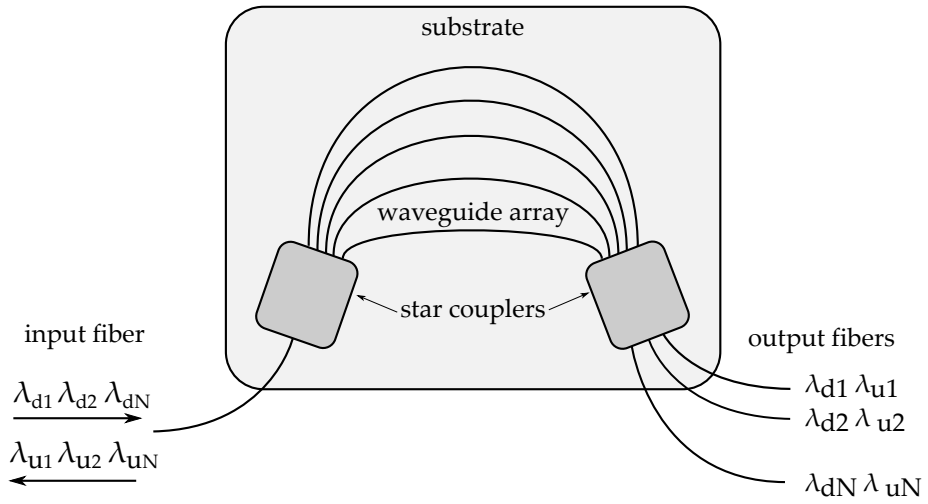

Figure 1.5: Arrayed Waveguide Grating (AWG) schematic functionality

are then spectrally sliced by the AWG in the RN. Alternatively, a multi-frequency laser (MFL) can be used which directly generates the desired wavelengths.

Apart from using the downstream signal, self-seeding systems have been proposed, see [27], in which however the optical link budget has to be small to function properly.

WDM-PON with tunable laser

In this WDM-PON variant, the upstream optical carrier is generated by a laser in the ONU. In theory it would be possible to use lasers with different fixed wavelengths at each ONU. But this so-called coloured approach implies high effort for operational issues (especially for planning and provisioning and spare-parts keeping) and is therefore not favoured by network operators. Instead, it becomes necessary that each ONU is equipped with a full band tunable laser that is capable of tuning to any wavelength within the upstream range. Such lasers are widely deployed in today's core WDM systems. Although being commercially available, it is not possible to use these tunable laser technology in a PON context because of their high price. In order to meet the price requirement of the residential market, ways of lowering the cost of the whole tunable transceiver have to be found, which will be described in Chapter 4.

1.2.3 Hybrid WDM/TDMA-PON

The combination of the WDM and TDMA approaches is the so-called Hybrid WDM/TDMA-PON, which is also called TWDM. Its standardisation is currently (mid-2013) discussed in FSAN and ITU SG15 Q2 under NG-PON2 and will be published as the G.989.x recommendation. The system is seen as a smooth migration step from existing

TDMA towards higher capacity systems which aggregate more clients on a single feeder fibre. A solution for not using tunable filters at the ONU is the usage of an ODN consisting of two stages, see [28]. In the first-stage RN, an AWG is used to demultiplex the wavelength, and in the second stage a (already installed) power splitter is then used to enable the TDMA of various ONUs, see Figure 1.4c. Alternatively, when using tunable filters at the ONU, also pure power splitter based topologies are possible. In a hybrid system, the insertion loss for seeded-reflected technologies is too high, and therefore tunable lasers at the ONUs need to be used.

1.2.4 Evolution of PON standards

First trials of PONs were done in the late 1970s, see [29] for a historical review. Since the late 1990s, mass deployments of commercialised systems were rolled out. Most of these installations so far have been done in Asia-Pacific and in North America. In Europe, up to now active optical network (AON) has a larger market share than PONs, but this is expected to change as nearly all big European network operators have started deploying GPON. All important standards were published by two standards bodies: International Telecommunication Union (ITU) and Institute of Electrical and Electronics Engineers (IEEE). In addition, the full service access network (FSAN) has to be mentioned as pre-standardisation body as its findings are later used in ITU. For a timeline of PON standards, see Figure 1.6. Up to now, all standardized PON systems are power splitter

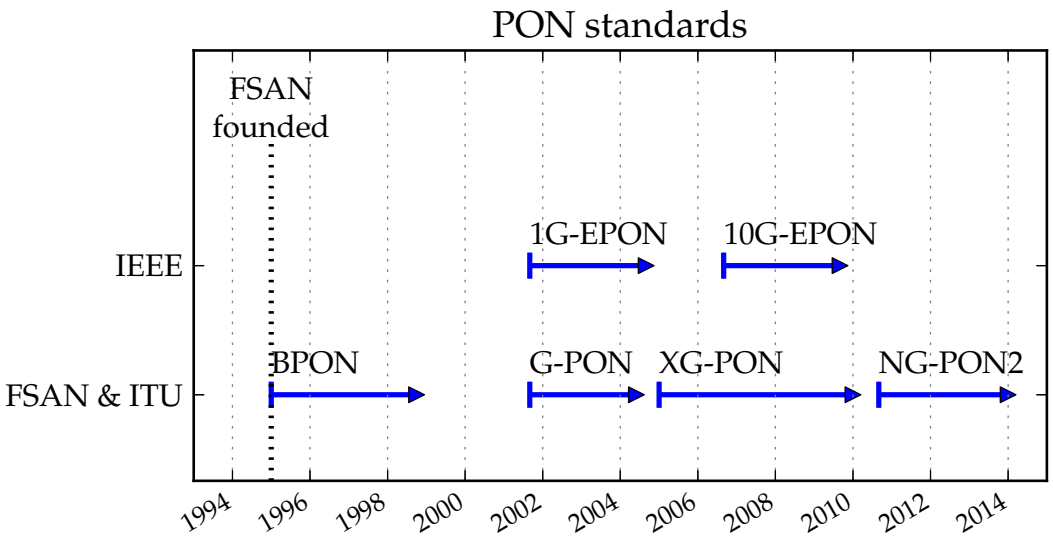

Figure 1.6: Evolution of PON standards: from beginning of study group to first publication of standard; including the targeted standardisation date of NG-PON2 [30]

based. For GPON, 10-Gigabit-capable passive optical network generation 1 (XG-PON1), upstream/downstream wavelength bands have been defined in order to achieve coexistence between the different versions. Compatibility between GPON and XG-PON1 for example can be achieved by installing a WDM splitter in the downstream at the CO and a wavelength blocking filter (WBF) at the ONU to optically multiplex or demultiplex wavelength bands for the different versions. Figure 1.7 shows that it is possible to migrate from one system to another without changing the ODN. Additionally, to facilitate the later migration, G.984.5 recommends to preinstall low-cost WBF at the GPON ONUs.

EPON and GPON cannot coexist in the same ODN as their wavelength plans overlap. Both systems define the 1490 nm for downstream and 1310 nm upstream. For future systems, it is possibly allowed to break with the coexistence with older systems as otherwise the available spectrum would be very small, if all coexistence requirements need to be fulfilled. Apart from the coexistence, it may also be allowed at a given point to replace the power splitter in the RN by an AWG.

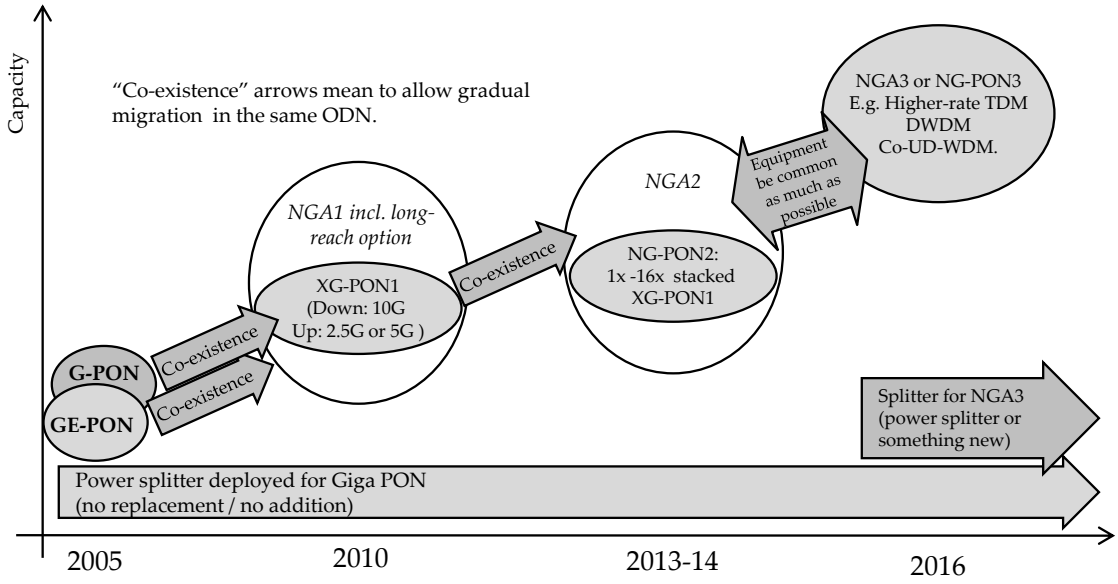

Figure 1.7: Migration to, and coexistence with current and future PON standards, based on [31, Figure 4]

1.3 PON Monitoring & Control for WDM-PON

For a practical WDM-PON deployment, it becomes necessary to detect and preferably also localize failures during installation and operation. In today's backbone network, many monitoring functions are already used and can possibly also be used in WR-WDM-PONs. However, many approaches cannot be applied directly to a WR-WDM-PON as their costs are too high or some other PON requirements are not met, e.g. power budget and operation wavelength. In general, the monitoring and control methods can be differentiated into the following three categories:

- fibre fault monitoring and localization
- optical performance monitoring (OPM)
- operations, administration and maintenance (OAM)

1.3.1 Fault monitoring and localization

In WR-WDM-PON, an operator needs to detect and localize fibre failures, e.g., fibre cuts or breaks. Fibre cuts can occur in all parts of the passive infrastructure of the WR-WDM-PON. In backbone WDM-systems, optical time-domain reflectometers (OTDRs) are used for fault detection and localization, see [32]. These commercially available OTDRs are not suitable for WDM-PONs as they operate on a single or on several selectable wavelengths and thus cannot detect fibre failures after the RN's AWG where the downstream wavelengths are demultiplexed.

Several solutions have been proposed to overcome this problem. A direct approach is to replace the fixed wavelength laser in the OTDR with a tunable one, see [33]–[35]. Instead of a tunable laser, [36] proposed the combination of a wavelength-locked Fabry-Perot laser and an optical bandpass filter for the generation of the OTDR pulses on different wavelengths. Further, solutions which re-use existing light sources have been proposed. [37] localizes fibre failures by reusing the downstream lasers for the generation of OTDR pulses. The OTDR pulses are used instead of the normal data traffic and are only used when an upstream channel is affected by a failure.

Instead of the generation of a dedicated wavelength at the OLT, the wavelength selectivity for monitoring different channels can also be achieved by using the spectral slicing property of the RN's AWG. At the OLT, a BLS generates a signal with covers the spectrum of all channels. This broadband signal is then spectrally sliced in the RN, reflected at the ONUs and received at the OLT. The reflectors are located near the ONU location and are passive components that reflect the light in the monitoring band, see [38].

Different implementations to spectral slicing methods were proposed by [39], [40]. Note that optical reflectors can also be used in combination with an OTDR to facilitate fault recognition and to achieve better measurements.

A completely different approach is to install additional fibres for monitoring purposes, see [41]. This however makes a massive change to the outside fibre plant necessary and is very cost intensive. An overview and also additional (less relevant) methods can be found in [12], [42].

1.3.2 Optical performance monitoring

The OTDR-variants are rather expensive, require a long measurement time, and depending on the implementation are service interrupting. Therefore it is essential to be capable to monitor optical parameters like the wavelengths and optical powers of WDM signals during operation.

Optical power

In general, monitoring of optical power is easy to achieve. It can, for example, be achieved via a tap-coupler and narrow-band with photo diode (PD). In WDM-PON, where different wavelengths are multiplexed, the optical power monitoring could be achieved by an arrayed monitor, as proposed by [43]. This, however, adds an additional complex component to the system.

In all optical systems, the measurement of the received optical power can be done in-line by monitoring the received signal strength indicator (RSSI) port of the transimpedance amplifier (TIA) in the OLT, see [44]. At the OLT in a WDM-PON, all channels are optically separated by the demux AWG and electrically processed. There, it is possible to monitor the optical per channel power via the RSSI ports of the TIAs.

For a TDM-PON, the signal strength of all ONUs can be measured at the RSSI port at the OLT. The measurement must be synchronised with the media access control (MAC) for mapping of signal strength to ONU. However, the measurement time of one burst transmission may not be sufficient to achieve high accuracy. [45] proposed therefore to average the measurement over several bursts from the same ONU.

In a WDM-PON, depending on the channel count, a multitude of electrical signal has to be terminated and digitized which may not be the preferred choice for space and complexity reasons.

Previously, [46] proposed that the optical powers of WDM signals can also be monitored by using pilot tones, which enable the usage of a single PD for monitoring all WDM channels. The optical power can then be estimated by multiplying the detected amplitude

of its pilot tone by the optical modulation index, see Section 2.1 for more details on pilot tones.

Wavelength

To monitor the operating wavelengths of WDM signals, [47], [48] proposed methods mostly utilising tunable filters such as acousto-optic tunable filters. Here, a small-band filter is swept over the complete spectrum and measures the optical spectrum. The optical frequency resolution is determined by the filter bandwidth. Again, pilot tones can be used to identify the channel under consideration within an optical multiplexed signal.

Another approach for the wavelength measurement is to use a temperature-tunable etalon filter. Here, the resonance peaks of the periodic etalon filter, which are matching the channel grid, are used to calculate an optical frequency offset value, see [49]. Section 3.3.1 will explain the principle operation of etalons and the calculation in detail. The usage of an etalon in combination with pilot tones for WDM multiplexed signals was first reported by [50] and again by the same author in [51]. The principle and its application within a WR-WDM-PON will be explained in Chapter 3.

Other parameters

Other parameters of the optical signal can be monitored as well. [52] gives a complete overview of the monitoring of transmission parameters. The list includes:

- effects of self-phase modulation [52]
- polarization-mode dispersion [52]
- optical path and channel identification [52]
- timing misalignment [52]
- chromatic dispersion (CD) [52], [53]
- wavelength registration [53]
- signal-to-noise ratio (SNR) [52], [53].

These parameters are however not as important during operation as power and wavelength for WR-WDM-PONs. For example, the chromatic dispersion influence is negligible for typical PON distance up to 40 km and modulation speeds of $\sim$1 GHz. The other parameters require expensive equipment to be measured precisely, which contradict the low-cost idea of PON systems.

1.3.3 Operations, Administration and Maintenance

For completeness, also monitoring and control functionality, which are used in higher layers, are mentioned. The OAM functionality designed for PON systems must be aware of PON specific properties and able to coexist with other management solutions. Most of the functionality is derived from older protocols like synchronous optical network (SONET) and asynchronous transfer mode (ATM). OAM refers in general to the tools and utilities to install, monitor and troubleshoot a network. The information can be embedded into the header of a data frame or be transmitted as separate OAM frames. The functionality can include:

- frame loss ratio
- frame delay
- frame delay variation
- network discovery
- link monitoring
- remote fault detection
- remote loopback.

For example, in GPON systems, dedicated physical layer OAM (PLOAM) frames are used to synchronise the timing between different ONUs to ensure error free functioning.

In this work, the focus of control and monitoring will be on efficient wavelength and power monitoring, which is a done on the physical layer.

1.4 Outline of chapters

This section gives a short overview over the following chapters. First, Chapter 2 will give an overview of the generation and reception of pilot tones. In Chapter 3, these pilot tones will be used in a WR-WDM-PON concept to monitor and control the wavelength and the received optical power of the ONUs, including the usage of a centralised etalon.

Chapter 4 will then evaluate the possibilities of the usage of (partly) uncooled tunable lasers in PON systems. Chapter 5 will show how to lock the lasing frequency to an arbitrary frequency, which exists in a grid-less system or in an unequal spaced grid. Finally, Chapter 6 will summarize the work and give an outlook on possible future fields of investigation.

2 Pilot tone generation & detection

Pilot tones are widely used in optical telecommunications. Mostly, pilot tones are used to provide additional low bit-rate information on a high-speed modulation channel. This additional information can be used to provide low complexity optical performance monitoring, see [54] for examples, and simple OAM services. The advantage is that in order to retrieve the low-speed information, no complete demodulation of the optical high-speed data has to be done. Reception of the pilot tone data can be done by a low-speed photo diode, which is less complex and thus more cost-effective. E.g., a receiver with bandwidth of 2 MHz is much cheaper than a receiver with 10 GHz. For a general description of pilot tone applications and generation schemes, see [54]. In the following, different pilot tone generation and detection methods and their impact on the transmitted high-speed signal will be described.

2.1 General description and definitions

The typical eye opening of an optical signal with pilot tones is shown in Figure 2.1. Depending on the implementation, either only the 1-level P_1, see Figure 2.1a, or both the 1- and 0-level P_0 are broadened, see Figure 2.1b. This widening of the levels is the modulation index of the pilot tone and is given in percentage. Here and in the following, the definition for the pilot tone modulation index m will be used as:

$$m = \frac{\Delta P}{P_1 - P_0} = \frac{\Delta P}{P_{\text{eye}}} \tag{2.1}$$

according to Figure 2.1a, where P_{eye} is the eye opening of the signal. Note that the pilot tone power amplitude ΔP is defined as the amplitude of the sine and not the peak-to-peak value and is expressed in %. The optical power of the sinusoidal pilot tone can then be expressed by:

$$P_{\text{opt}}(t) = P_{\text{avg}} \left(1 + m \sin\left(\omega t\right)\right) \tag{2.2}$$

with P_{avg} being the average optical power of the signal without a pilot tone and ω the frequency of the tone. Equation (2.2) can also be written like

$$P_{\text{opt}}(t) = P_{avg} + \Delta P \sin(\omega t) \tag{2.3}$$

where ΔP expresses the power amplitude of the sinusoidal tone.

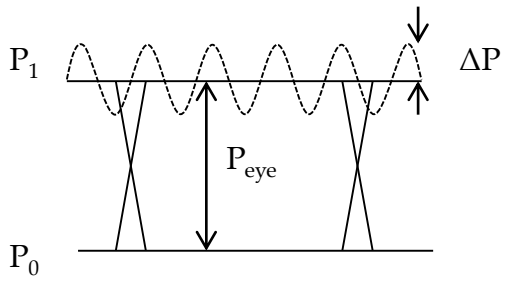

(a) Eye opening and amplitude definitions with only 1-level modulation

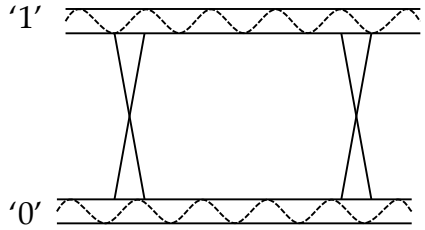

(b) Eye opening with 1 and 0-level modulation

Figure 2.1: Pilot tone and eye diagram openings

2.1.1 Degradation of data signal

In the following subsection, the influence of the pilot-tone on the high-speed data will be investigated.

Theory

As the data-signal levels are no longer strict "1" or "0", degradation of the transmitted data is seen. Assuming that both levels have a mean value of μ_0 and μ_1 and are Gaussian distributed with a standard deviation of σ, their distribution f can be expressed as

$$f(x;\mu,\sigma^2) = \frac{1}{\sigma\sqrt{2\pi}} e^{-\frac{1}{2}\left(\frac{x-\mu}{\sigma}\right)^2}. \tag{2.4}$$

The bit error rate (BER) can be calculated via the integral of falsely detected "1" and "0". As seen from Figure 2.2, both integrals range from $\pm\infty$ to the decision threshold s, the BER is then expressed by

$$\text{BER}(s,\mu_0,\mu_1) = \underbrace{\frac{1}{2}\int_{-\infty}^{s} f(x;\mu_1,\sigma^2)\,dx}_{\text{1 detected as 0}} + \underbrace{\frac{1}{2}\int_{s}^{\infty} f(x;\mu_0,\sigma^2)\,dx}_{\text{0 detected as 1}} \tag{2.5}$$

Using the Gaussian error function erf, see [55],

$$\operatorname{erf}(x) = \frac{2}{\sqrt{\pi}} \int_0^x \mathrm{e}^{-t^2}\, dt, \tag{2.6}$$

Equation (2.5) can be expressed as follows:

$$\mathrm{BER}(s, \mu_0, \mu_1) = \frac{1}{2} + \frac{1}{4}\left[\operatorname{erf}\left(\frac{s-\mu_1}{\sigma\sqrt{2}}\right) - \operatorname{erf}\left(\frac{s-\mu_0}{\sigma\sqrt{2}}\right)\right]. \tag{2.7}$$

Assuming the case shown in Figure 2.1a, where only the 1-level is modulated with a sinusoidal signal $\cos(\phi)$ centred around the average power $\overline{\mu_1}$ and the 0-level constant zero, one gets:

$$\mu_1(\phi) = \overline{\mu_1} + a_i \cos(\phi) \tag{2.8}$$

Then, the average BER can be calculated as:

$$\overline{\mathrm{BER}(s, \mu_0, \mu_1)} = \frac{1}{2\pi} \int_0^{2\pi} \mathrm{BER}(s, \mu_0, \mu_1(\phi))\, d\phi. \tag{2.9}$$

The second case, as shown in Figure 2.1b, shows a worse performance as the eye opening is further decreased because of the widening of both levels. As it provides no notable advantage over modulating only the 1-level, it is therefore not further considered.

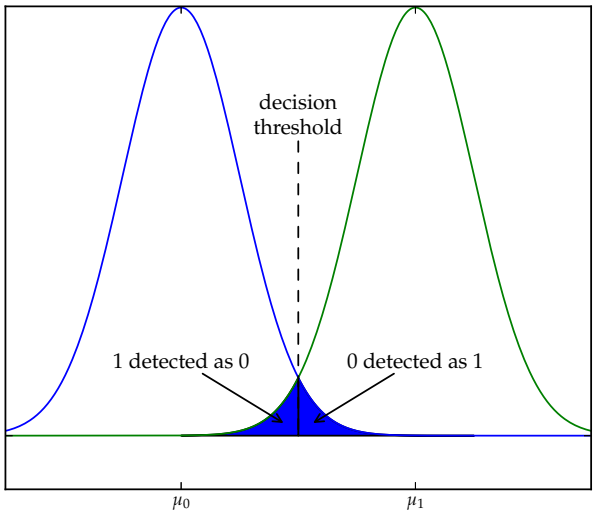

Figure 2.2: Probability of 1 and 0-level

Numerical simulation

It must be mentioned that Equation (2.9) does not consider the frequency of the pilot tone. Smaller frequencies $\leq 30\,\text{kHz}$ are corrected in real implementations by the receiver's automatic gain control in the limiting amplifier (LA), e.g., [56] specifies a low frequency cut-off of 30 kHz. This rejection is necessary to filter out baseline wander. To reflect this in the simulation, two different detection algorithms of the threshold value have been implemented: hard and optimum threshold. The hard decision threshold s_{hard} is set to

$$s_{\text{hard}} = \frac{\overline{\mu_0} + \overline{\mu_1}}{2}. \tag{2.10}$$

This means that the receiver does ignore the low-frequency pilot tone and sets its threshold to the average received power. In the second case, the receiver is capable of following the power variation introduced by the pilot tone and sets the decision threshold s_{opt} always to the optimum point which is

$$s_{\text{opt}} = \frac{\overline{\mu_0} + \mu_1(\phi)}{2}. \tag{2.11}$$

Figure 2.3 shows the numerical simulations with the values of Table 2.1. It can be seen that a modulation index of 0.1 has only a small influence on the BER. The influence can be quantized by calculation of the Q-factor. The equivalent Q-factor of a BER can be calculated from the BER Equation (2.9) by using

$$\text{BER} = \frac{1}{2}\,\text{erfc}\left(\frac{Q_{\text{lin}}}{\sqrt{2}}\right). \tag{2.12}$$

with the erfc, the complementary error function, defined as

$$\text{erfc}(x) = 1 - \text{erf}(x). \tag{2.13}$$

The Q-factor is expressed in logarithmic scale

$$Q_{\text{dB}} = 20 \log Q_{\text{lin}}. \tag{2.14}$$

The Q-factor penalty is the difference between the amplitude index 0 and the simulated value. As seen from Figure 2.4, in the hard-threshold worst case, the highest Q penalty is 1.0 dB for a modulation index of 0.1. This penalty is acceptable in many scenarios, where it can be compensated by the available system budget. The results are well aligned with [57].

parameter		value
noise variance	σ_{th}^2	$\left(3.87 \times 10^{-8}\right)^2$ W = 1.497×10^{-15} W
average 0-level	$\overline{\mu_0}$	0 mW
average 1-level	$\overline{\mu_1}$	−33 dBm
PD responsivity	R	0.8 A/W

Table 2.1: Simulation parameters

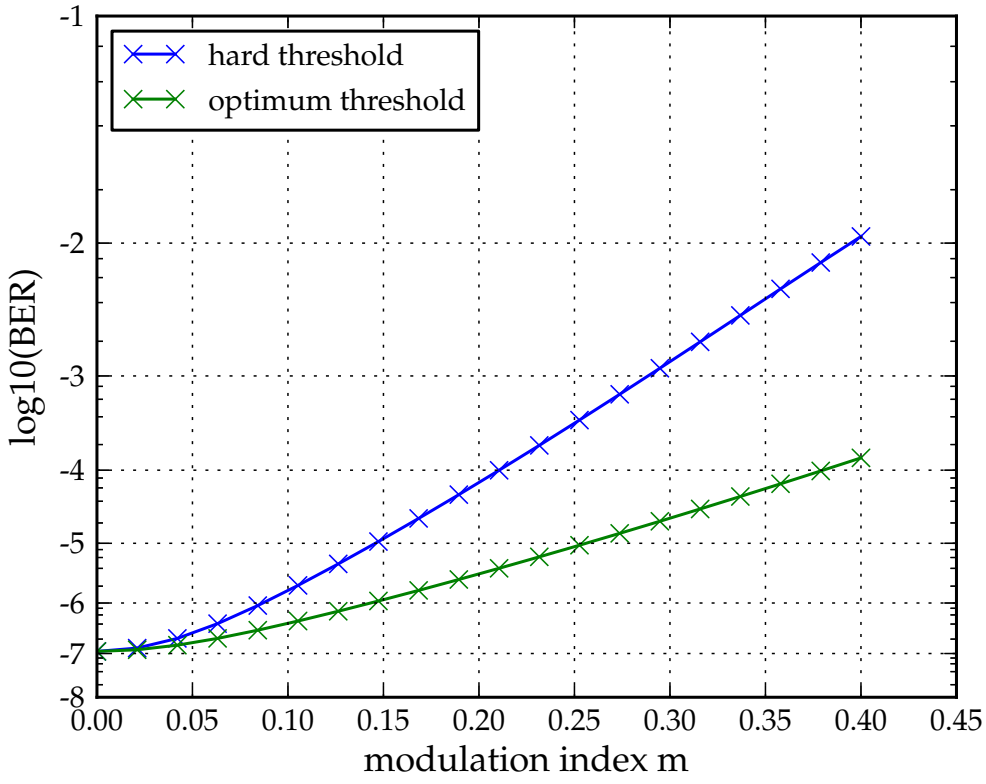

Figure 2.3: BER for different modulation index using the parameters from Table 2.1

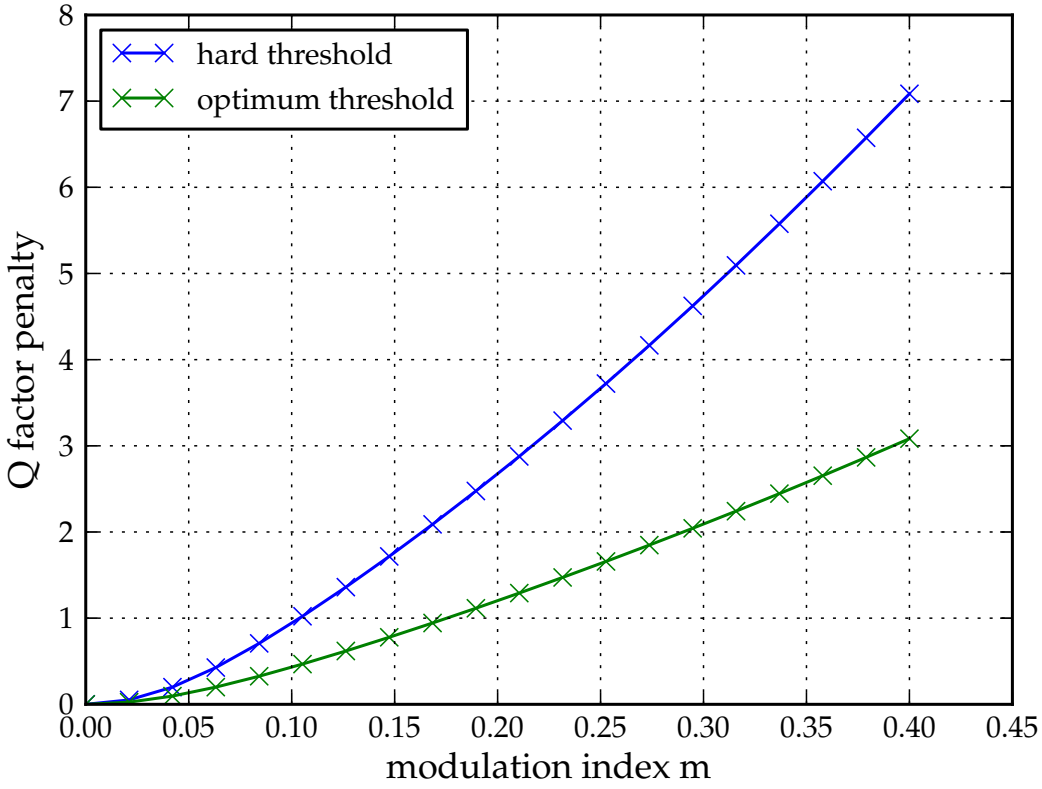

Figure 2.4: Q factor penalty for different modulation index using the parameters from Table 2.1

2.2 Implementation options for pilot tone generation

In this section, standard methods how to generate a pilot tone will be described. Then, a new method for generation of a pilot tone by changing the encoding scheme of the transmitted data will be described. At the end, a comparison of the performance of the presented methods and their functionality on system level will be done.

2.2.1 Standard methods

Several methods for pilot-tone generation are known, e.g., [54]. Hereinafter, the two most commonly used methods are described: bias modulation of the laser diode and optical modulation using an external variable optical attenuator (VOA). In most cases, the pilot tone is generated by adding a pilot tone current to the laser bias current. As the schematic in Figure 2.5a shows, the modulation is normally done via a bias tee in the electrical domain before the laser diode. Due to the integration of sub-components, this functionality is often integrated in the laser driver, e.g. [58]. This enables the application of the pilot tone (in the laser driver) to the high-speed data signal at 1-level only. The resulting output eye can be seen in Figure 2.1a. By only modulating the 1-level, the eye degradation caused by jitter and extinction-ratio variations of the data signal are minimized as compared to the method where both 0 and 1-level are modulated.
An alternative method for the generation of pilot-tones is the usage of an external VOA. In the VOA, an incoming optical signal is attenuated by electrically controllable attenuation. By replacing the static electrical signal with the desired pilot-tone signal both, the optical 0 and 1-levels are modulated. When placing the VOA directly after the laser, the eye diagram shows only the broadening of the 1-level. The broadening of the 0-level cannot be measured, as the signal at this point still has a high extinction ratio, with a very low absolute 0-level. As calculated in the former subsection, the superposition of the data

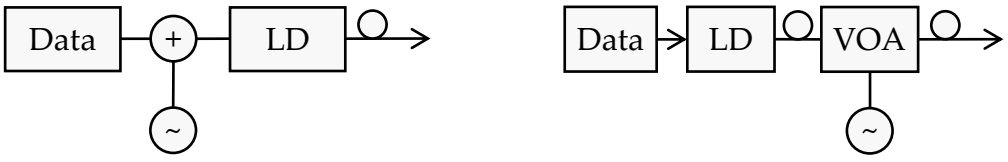

(a) Pilot tone modulation at the laser bias

(b) Pilot tone modulation with an external VOA

Figure 2.5: Standard pilot tone generation methods

and pilot-tone results in a closure of the eye opening at the receiver. This can be seen in Figure 2.6 which shows a measurement using an external VOA. The exactly same eye-diagram can be measured, if the bias generation method is used.

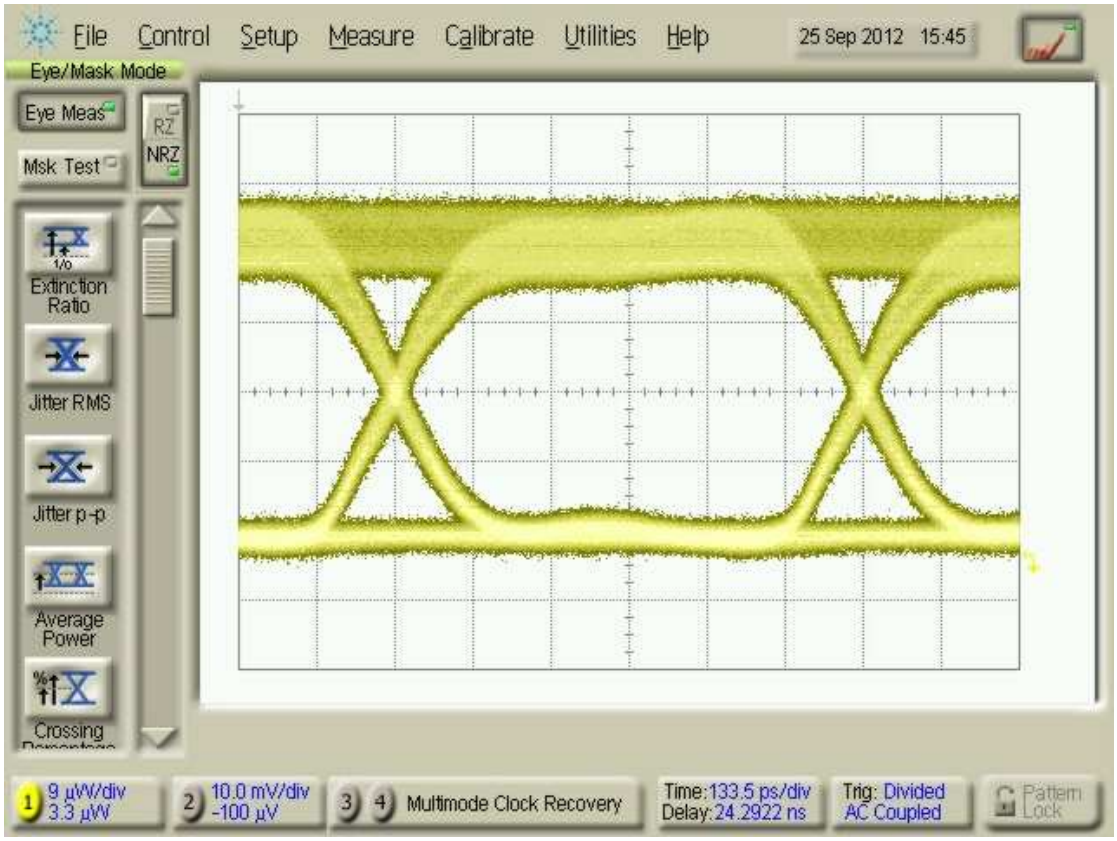

Figure 2.6: Eye opening at the receiver with a pilot tone modulated on the 1-level using the external VOA method

2.2.2 Data disparity modulation

In many applications, the digital data is encoded or scrambled prior to transmission. This is done in order to achieve DC-balance, bounded disparity, and to generate bit transitions, which allow the clock recovery to work properly. Examples include encoding which avoids long sequences of ones or zeros. One implementation is the so-called 8B/10B coding. This method is well-known and used in several protocols like Gigabit Ethernet (GbE), Fibre Channel (up to 8G-FC), Serial Digital Interface (SDI) video, and InfiniBand (up to quad data rate, QDR). 8B/10B encoding was first proposed by [59] in 1983 and first standardized in ANSI X3.230-1994 [60]. Note that 8B/10B implementation in the Ethernet protocol (IEEE 802.3z as defined in [61]) is the most common one. Newer, higher-speed versions of the Ethernet protocols ($\geq$ 10 Gbit/s), mostly use 64B/66B encoding for enhanced bandwidth efficiency.

In 8B/10B line coding, an 8-bit data word is encoded into a 10-bit transmission word which has a minimum of 4 "ones" and a maximum of 6 "ones". The deviation from the ideal average of 5 "ones" of a single 10-bit transmission word is equalized by encoding the following 8-bit data word in the proper 10-bit transmission word, resulting in a maximum running disparity (RD) of +/- 1. The RD is the value which reflects if the former data word was encoded with a positive (RD+) or negative (RD-) disparity. The following 10-bit data word is then encoded using the opposite disparity. Table 2.2 shows a part of the RD- and RD+ mapping. The 10-bit data words are generated by a combination of two 5B/6B NRZ-codes and one 3B/4B NRZ-code. When the pilot tone is used for optical

Code Group Name	8-bit data word	RD–	RD+
D0.0	000 00000	100111 0100	011000 1011
D1.0	000 00001	011101 0100	100010 1011
D2.0	000 00010	101101 0100	010010 1011
D3.0	000 00011	110001 1011	110001 0100
D4.0	000 00100	110101 0100	001010 1011
...			
D1.1	001 00001	011101 1001	100010 1001
D2.1	001 00010	101101 1001	010010 1001
D3.1	001 00011	110001 1001	110001 1001
...			

Table 2.2: Part of 8B/10B encoding table

path monitoring or low speed overhead data transport, the optical signal is detected by a low-bandwidth photo diode. The average power of the data signal has to vary so that after filtering with an electrical low-pass filter (LPF) the pilot tone can be detected.

Following this principle, the 8B/10B encoder was changed so that the distribution of ones and zeros in the data stream modifies the average power and therefore also varies the optical signal. The method works by selecting the 10-bit code words from the proper 8B/10B encoding table.

For instance, if the target power is at 0.55 relative to the peak signal power, all 10B-words in a frame of several (e.g., 16) words are taken from the RD- table, resulting in all 10-bit code words having 5 or 6 "ones". If the average power value to be achieved is at 0.45, the 10B-code words are taken from the RD+ table, such that all 10-bit words have 4 or 5 "ones". Values between 0.45 and 0.55 are achieved by using fixed (RD- or RD+) tables for a fraction of the frames, while the remaining fraction is encoded using the standard 8B/10B encoding process. By using this method, nearly arbitrary short-time evolution of the average power can be impressed onto the optical signal, for instance sinusoidal tones.

At the receiver, the 8B/10B encoded words can be decoded using standard 8B/10B decoding tables. While disparity errors will occur, the resulting 8-bit data word is still correct. This new method can be applied using standard optical transceivers (e.g., small form factor pluggable (SFP), 10 Gigabit Small Form Factor Pluggable (XFP)). As the pilot tone is generated in the line encoder logic, no changes to the optical hardware are required. Figure 2.7 shows the implementation of the 8B/10B pilot-tone scheme with an external modulator.

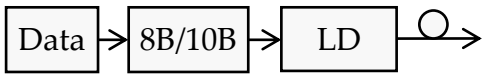

Figure 2.7: Pilot tone modulation of the encoding disparity

Implementation

In order to experimentally validate the performance of the new generation method, an algorithm was implemented on a field programmable gate array (FPGA). A Xilinx Kintex 7 FPGA was programmed to generate a sinusoidal pilot tone in the range between 0.1 and 1.1 MHz. The incoming high-speed (1.0 Gbit/s) Gigabit Ethernet stream is segmented into slots of 16 8B-words, which are encoded to yield a sample point of the tone signal to be generated. The equivalent sample rate of the tone signal is therefore $\frac{1\,\mathrm{GHz}}{16 \cdot 8} = \sim 7.8\,\mathrm{MHz}$. For each of the slots, the 8B/10B encoding algorithm selects the encoding table such that the accumulated disparity in the slot corresponds to the target value of the sampled sinusoidal tone signal, meaning that the amount of 10B words taken from the RD- / RD+ table was then calculated on the fly to approximate the desired value. As the incoming data are random, the target disparities cannot always be achieved within the slots. This

can result in a higher noise level of the tone signal, however, the algorithm tries to achieve the target value as fast as possible and then switch back to the normal encoding scheme. This resulted in a good overall performance, although not every slot can be encoded with its target value. The implementation can generate arbitrary patterns up to a frequency of 3.9 MHz. The core implementation very high speed integrated circuit hardware description (VHDL) code does not contain any Xilinx-specific parts which would prevent the code to be ported to any other FGPA vendor's hardware. The only vendor specific part is the code for addressing the multi-Gigabit transceivers (MGTs) which needs to be adapted for every FPGA model anyhow, see Figure 2.8 for a detailed schematic view of the FPGA.

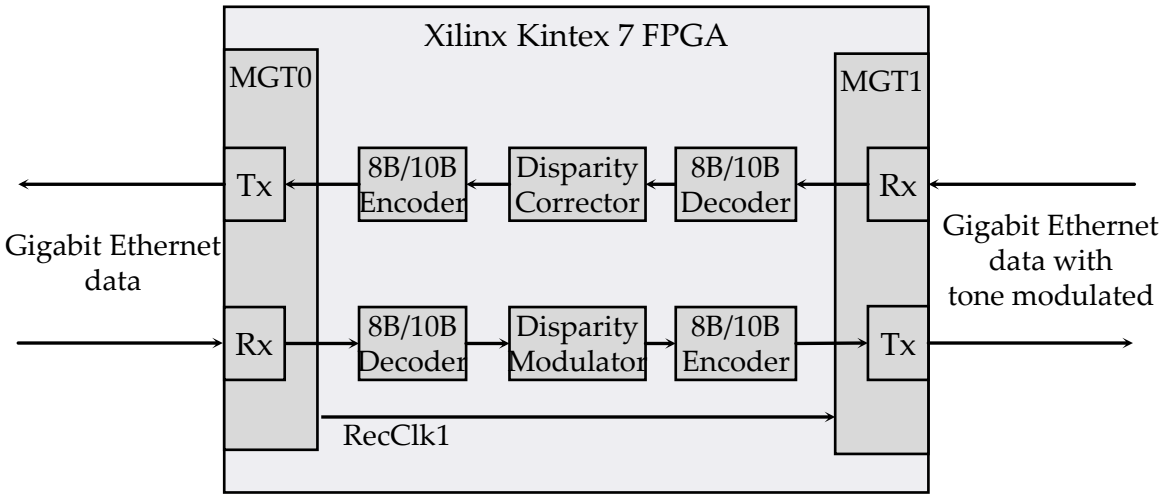

Figure 2.8: Schematic view of the FPGA with the modified 8B/10B encoder in TX direction (MGT0 $\rightarrow$ MGT1) and the according disparity correction in RX (MGT1 $\rightarrow$ MGT0)

Performance

Different to the standard pilot tone generation methods, the disparity modulation does not lower the eye opening of the signal. This can be made clear when looking at the laser output power vs. injection current (P-I) curve, see Figure 2.9. When operating the data modulation under normal conditions ($I_0 > I_{th}$) the extension ratio over time does not change. However, the average transmitted power slightly changes. This, however, cannot be seen in the eye-diagram, Figure 2.11. Only after the signal is low-pass filtered, the pilot tone can be detected, see Figure 2.10.

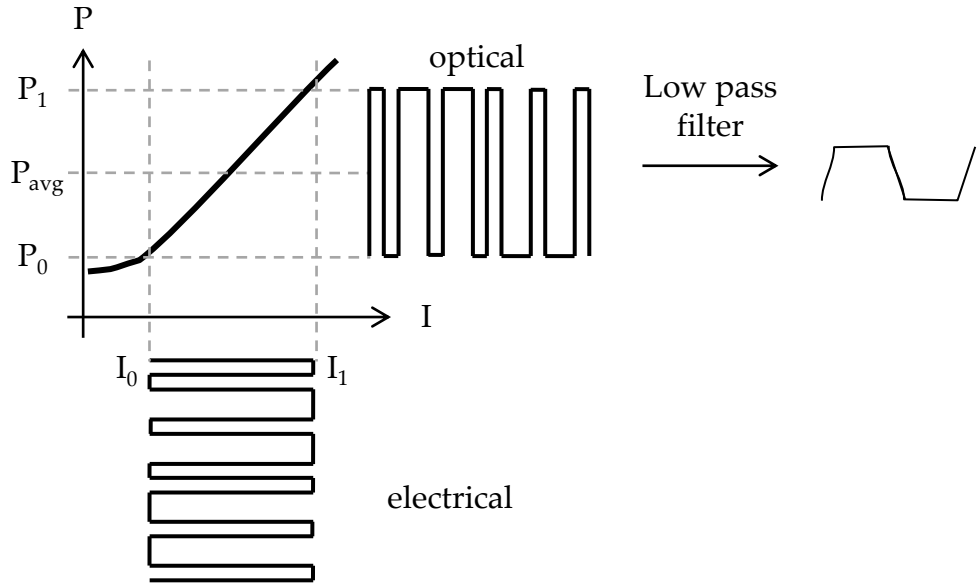

Figure 2.9: P-I laser curve with the disparity modulation

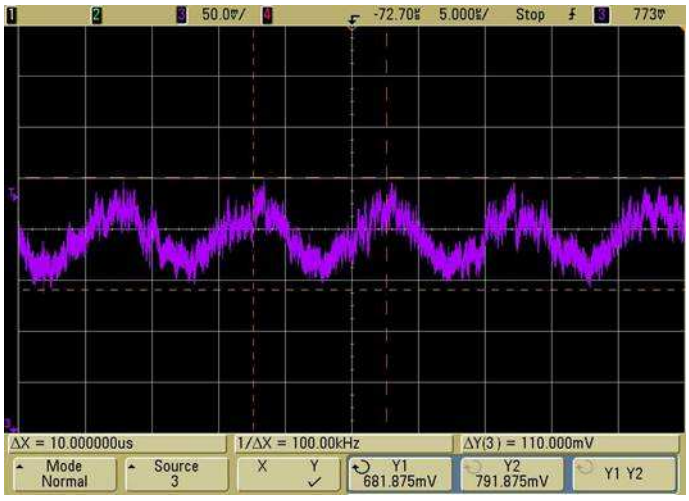

Figure 2.10: Disparity-generated sinusoidal tone with a frequency of 100 kHz at optical level of −28.5 dBm, additionally low pass filtered

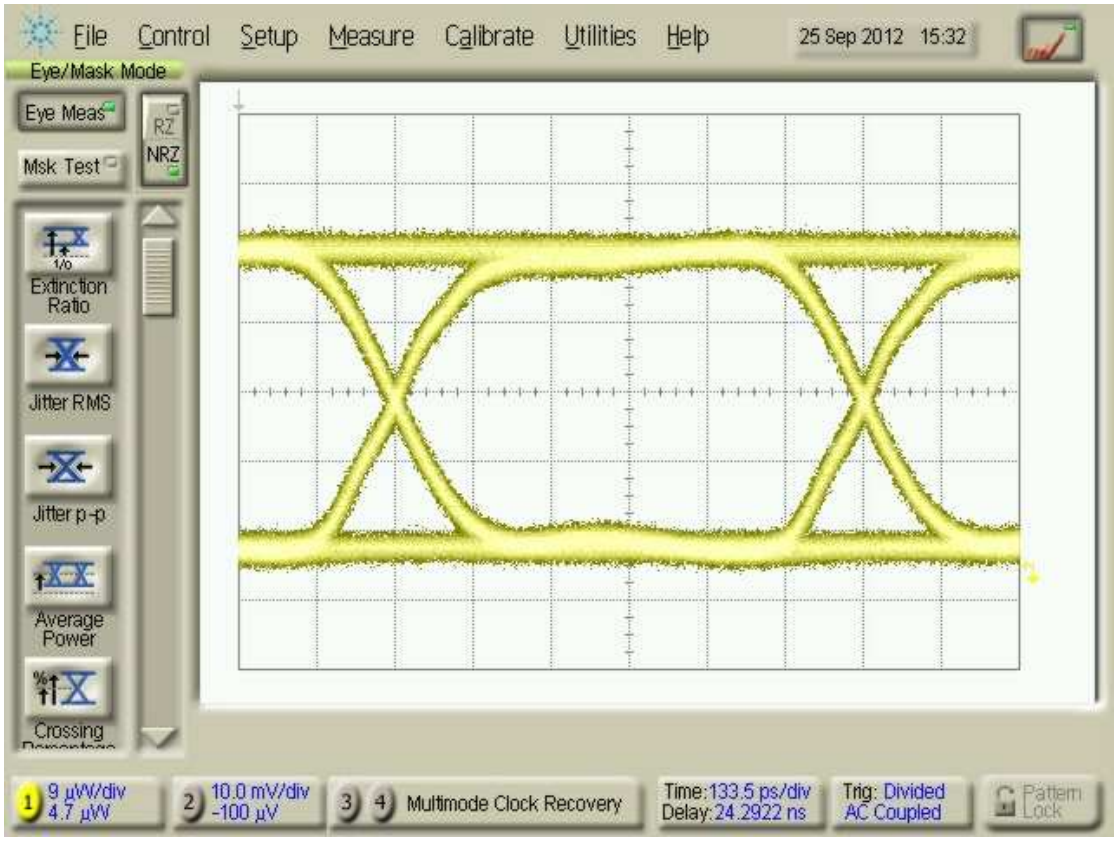

Figure 2.11: Eye opening with disparity modulation

2.2.3 Experimental comparison of pilot tone generation methods

The newly implemented method was experimentally compared to the conventional bias-modulation and external-VOA methods. With the setup shown in Figure 2.12, all methods could be realized to compare the results under similar conditions. A data stream (compliant random pattern (CRPAT)) was generated by an Ethernet protocol tester and sent to the FPGA board. To demonstrate the new pilot modulation scheme, the modified 8B/10B encoding was applied, while for the other two modulation schemes, standard 8B/10B encoding was performed in the FPGA. The output of the FPGA was used to drive a Mach-Zehnder modulator (MZM).

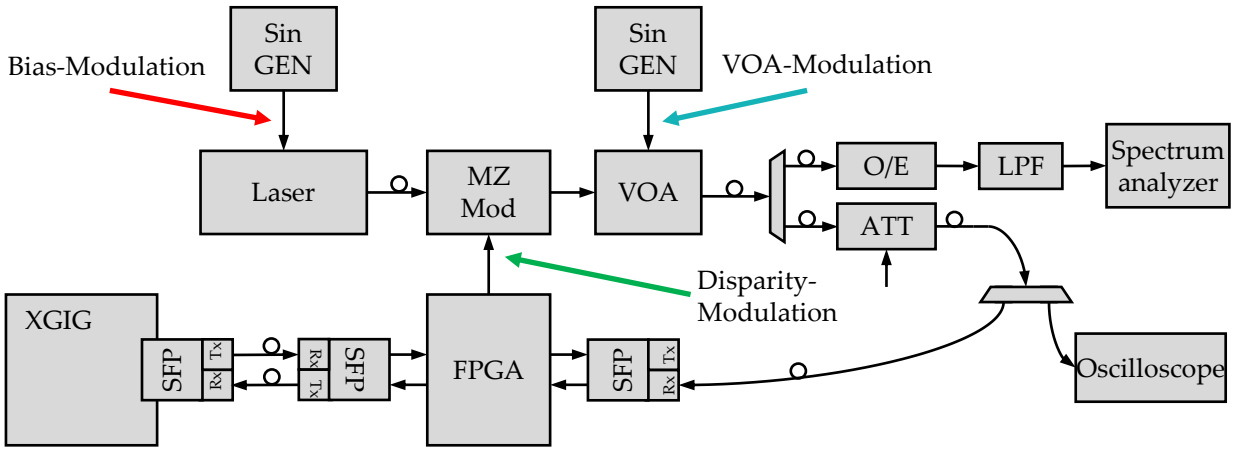

Figure 2.12: Experimental setup

Alternatively, instead of the modified 8B/10B encoding, either the bias of the transmitter laser was modulated or the VOA input was driven using a Function Waveform Generator. The VOA was a single-channel silicon VOA from Kotura (SVOA100). A fraction of the modulated optical signal was received by a low-bandwidth photo diode and observed on an electrical spectrum analyser. The optical signal was attenuated, received in a standard Gigabit Ethernet SFP receiver and sent to the FPGA, where the modified 8B/10B encoding was removed to meet the standard input expectation of the protocol tester. This step was needed as the Ethernet protocol tester (Finisar Xgig-C021) would interpret disparity errors as bit errors. For all cases, a pilot tone with a constant modulation index of 10% was generated over a range of 0.1 to 1.1 MHz. For completeness, also a reference measurement without a pilot tone was done. The laser used in the experiment was a tunable sampled Y-branch laser, see Section 4.2.2.

As seen from Figure 2.13, the bias-modulation shows the typical pilot tone penalty which can also be see in Figure 2.3. The performance of the VOA method shows an even higher penalty than the bias modulation method, due to the non-linear tone distortions which led to higher harmonics of the tone signal modulation onto the high-speed data. As

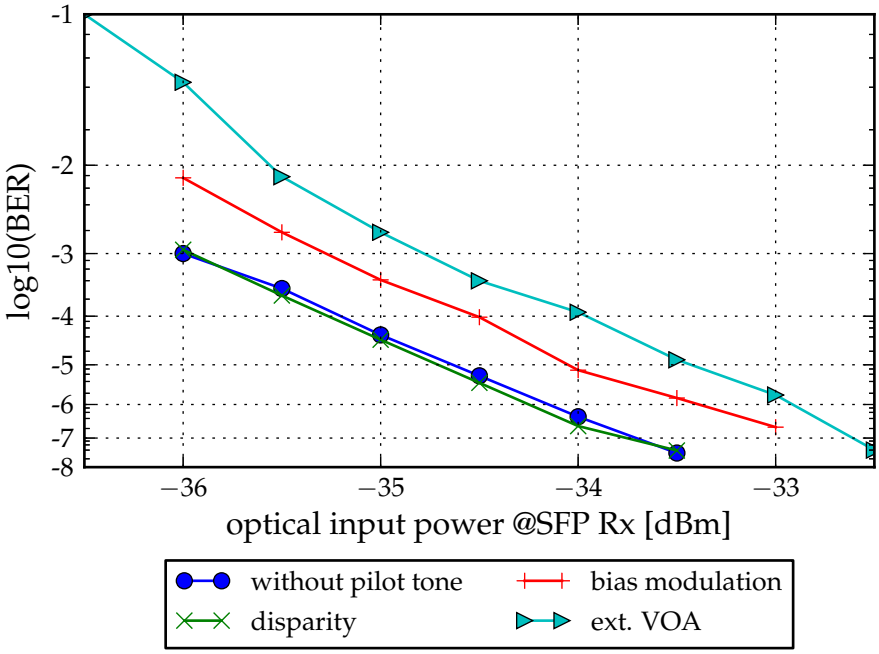

Figure 2.13: Experimental results; 10% of modulation index

expected, the FPGA method shows a similar performance as the case without modulation. Also the suppression of the harmonics was measured, which were generated by the different methods, in order to quantify the error in the presence of multiple tones.

Additionally to the BER, the electrical spectrum was measured to derive a quality measure for the generated tone. The laser bias and the VOA methods show a constant suppression ratio over all tone frequencies. For both methods, the second harmonic was the most significant with a suppression of ∼50 dB (bias) and ∼28 dB (VOA). However in the disparity-modulation case, the second harmonic was very low (suppression ratio $>$ 40 dB), while the third harmonic became the most significant one. It is well known that rectangular signals only have components of odd-integer harmonic frequencies. As shown in Figure 2.14, the suppression ratio of the third harmonic changes with frequency and is only 12.6 dB for a tone frequency of 1.1 MHz ($3f_0 = 3.3$ MHz). However, as only tone frequencies up to 1.1 MHz are considered, third harmonics of tone frequencies over 366 kHz would not fall into the tone frequency spectral range and will be filtered out at the receiver.

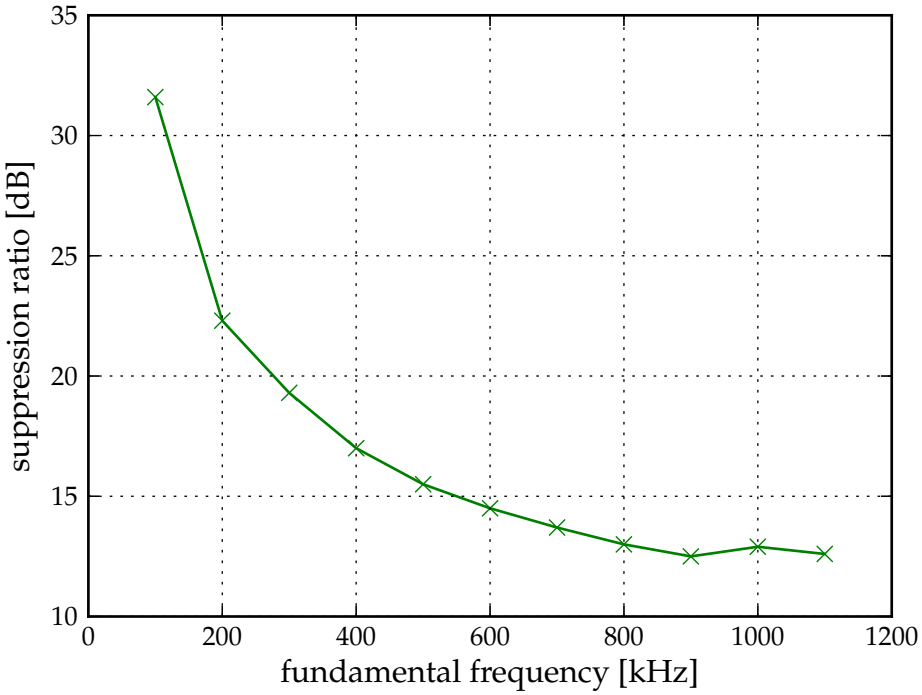

Figure 2.14: Third harmonic ($3f_0$) suppression ratio of the FPGA method

2.3 Comparison of the generation methods on system level

In the section above, different methods how to generate pilot tones were described. In this section, the focus is on the system / application side. The focus lies on the transmission of a low bit-rate service channel which is imprinted onto a high bit-rate data (or payload) channel from one network node to another. The reception of such a service channel adds small cost as the pilot tone data can be received by a low-bandwidth and thus low-cost photo diode. The information contained in the service channel could be any property of the optical signal under consideration, e.g. wavelength, the high-speed modulation format. The objective is that the information contained in the pilot tone helps to make the receiving side more "intelligent". Example usages of these OAM services are fault detection, status exchange and verification of the network during the installation which are operation and maintenance

The data of the service channel is modulated onto the pilot tone. All known modulation schemes could be implemented: frequency, amplitude and phase modulation. Throughout the thesis, only phase modulation will be considered, in particular, binary phase shift keying (BPSK). Several facts favour the use of BPSK: First, the modulation format is well known and easy to implement. Second, the amplitude can be made constant by applying phase transition with constant amplitude. A constant amplitude results in a constant

eye degradation. Using amplitude modulation results in time-dependent high-speed data bit-rate error changes caused by the varying pilot-tone amplitude. Third, in a WDM system with more than one channel and simultaneous reception of all pilot tones, the pilot-tones do not overlap spectrally, if the multiplexed signal is monitored. Fourth, BPSK has a 3 dB better SNR tolerance than on-off keying (OOK). Summing up all the arguments, a system with the parameters in Table 2.3 is used in the following. Finally, Section 3.5 shows how a fixed-amplitude pilot tone can be used for laser wavelength control.

Parameter	Value	Note
Modulation format		BPSK
Modulation depth	2 - 10%	Peak power variations (i.e., sub carrier amplitude) divided by average power w/o modulation
Data rate	1125 Bit/s	
Channel spacing	10 kHz	
Frequency range	100 - 1100 kHz	resulting in 101 frequencies
Frequency stability	$\pm$ 300 Hz	

Table 2.3: General pilot-tone system specification

2.3.1 Bias modulation

As described, the generation of the bias modulation has to be done electrically. Thus, the mechanism for pilot-tone generation must be located in front of the laser driver and laser diode. Both components are physically located in the transceiver (e.g., SFP, XFP) of a node. Therefore, both the transceiver and the node must have this capability to transmit / receive a pilot tone (and pilot tone data). This must already be considered during system design as later changes are most likely impossible. Figure 2.15 shows a complete system with pilot tones in both direction (A->B and B->A). It is also possible that under certain conditions unidirectional functionality is sufficient so that the hardware effort could be reduced.

2.3.2 VOA modulation

VOA modulation is done in the optical domain. Therefore, the VOA can be located at node A or anywhere along the fibre between node A and node B, see Figure 2.16 for a set-up where the VOA is between node A and B. Here, node A can use a standard transceiver without any pilot tone capability. By the usage of a VOA, an existing system can be upgraded without the change of existing transmitter hardware. The main drawback of

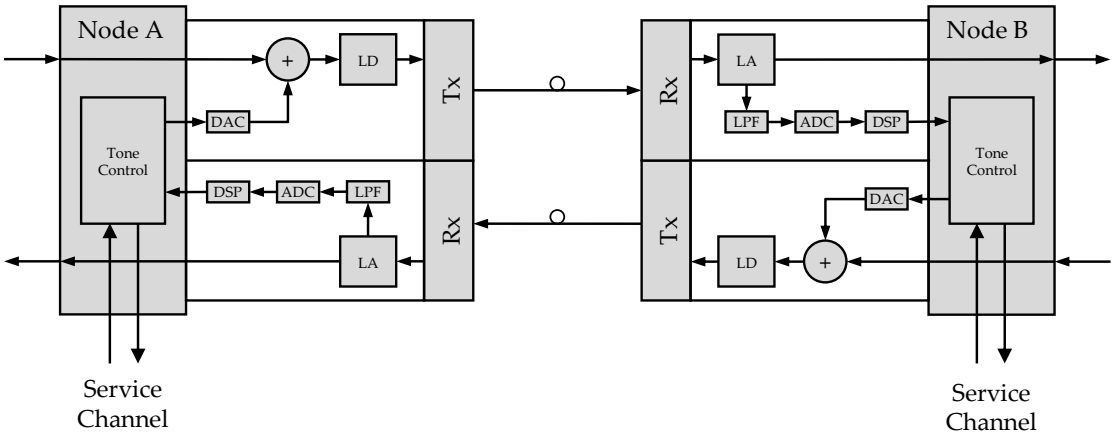

Figure 2.15: Bias pilot tone system view with generation and reception at nodes A and B

the VOA modulation is the insertion loss. For a higher modulation depth, the working point needs to be at lower base attenuation. In the set-up, the working point for 10% modulation index was a base attenuation of $\sim$4 dB. Another issue of the VOA is the negative effect on the overall availability as a problem caused by the VOA can be service affecting on the high-speed data transmission signal.

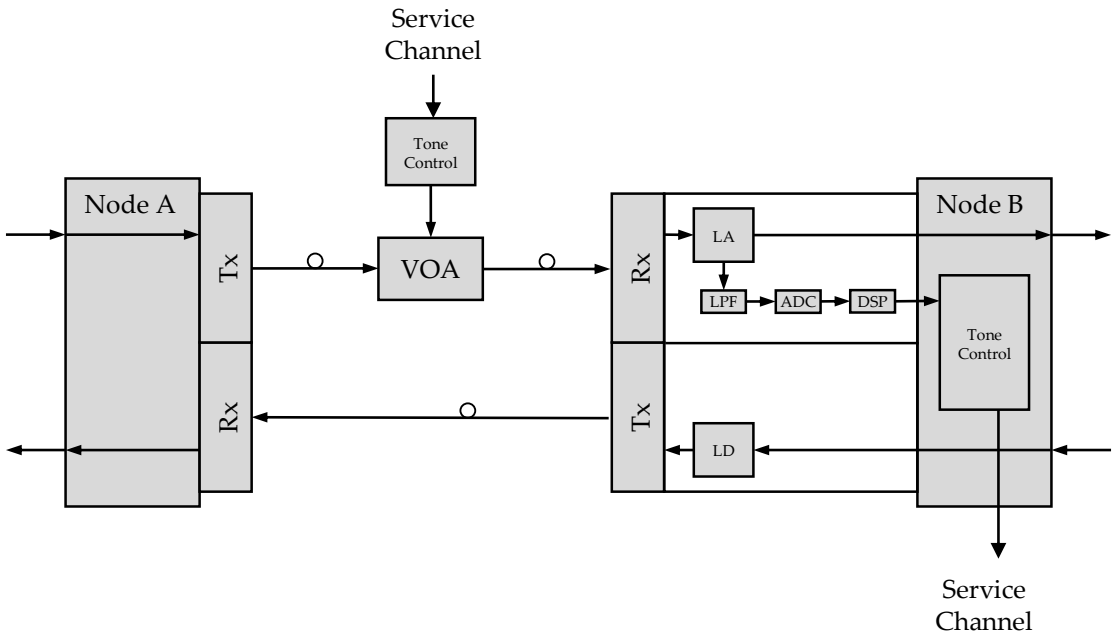

Figure 2.16: VOA pilot tone system view with generation between nodes A and B and reception at node B

2.3.3 Disparity modulation

The comparison results show that disparity modulation has no penalty on the high-speed data signal. This advantage, however, comes at a drawback, as a non-standard Ethernet stream is generated. This has two impacts: a special line encoder has to be implemented, and the receiver must be aware that the received stream will contain disparity errors. A possible workaround is to change the receiver such that it ignores disparity errors. One major advantage, however, is that no change in the pluggable transceiver needs to be implemented, see Figure 2.17. This means that in a node with a disparity line encoder a pluggable optical transceiver with standard electrics and optics can be used.

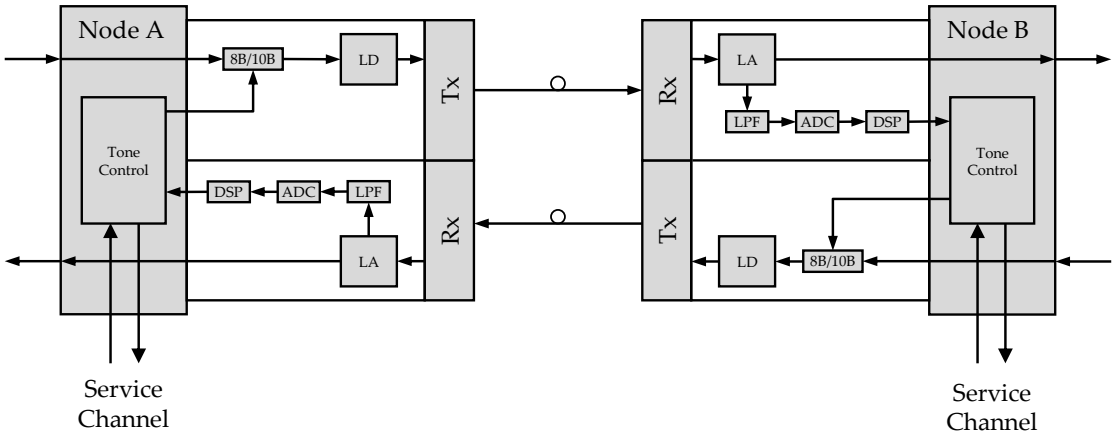

Figure 2.17: Disparity pilot tone system view with generation and reception at nodes A and B

2.3.4 Comparison conclusion

Each of the three methods presented has advantages and disadvantages. The bias method may be chosen, if the system can be designed from scratch so that all pilot-tone functionality can be integrated. The VOA method is preferable for upgrades of existing systems or where the pilot tone must be introduced between two nodes. Finally, the disparity modulation has advantages when standard optical transceivers are used. There is no general recommendation, and the usage of any method must be chosen within the system context, therefore, Table 2.4 can be used to select the most appropriate method.

In addition to the described scenarios, a pilot tone can also be received at a monitor location. This monitor location is common to all system methods as only pilot-tone data is analysed, and the high-speed data is not demodulated.

Method	Advantages & disadvantages
Bias	+ Can be integrated in the node - Requires changes to node and transceiver design - Eye opening penalty increase
VOA	+ Allows addition of pilot tone between nodes + Can be added as an upgrade to an existing system - Lowers fibre plant availability, if implemented "in between" two nodes - Adds additional loss - Eye opening penalty increase
Disparity	+ Standard transceivers can be used + No penalty on eye opening - Requires 8B/10B encoded data - Low suppression of third harmonic for higher pilot tone frequencies - Data stream gets invalid with regard to standard Ethernet protocol

Table 2.4: Pilot tone comparison

2.4 Multi-tone detection

Until now, in this chapter only systems with one pilot tone have been described. In this section, a WDM system in which several pilot tones are transmitted over a single fibre will be described.

2.4.1 Optical signal properties

For the following simulation, a WDM system with the following properties will be assumed: On a single fibre, N optical channels each with an optical power of P_i are multiplexed. To each optical channel, a unique pilot tone with a known modulation index and thus a known power amplitude ΔP_i is applied. Figure 2.18 shows a set-up of the system under consideration. Furthermore, the correspondence between the optical channel and the pilot tone frequency ω_i is known. Then, the multiplexed pilot tone signal P_{mux}, which can be seen after taping out a small part of the multiplexed signal and low-pass filtering, can be expressed by

$$P_{\text{mux}}(t) = \sum_{i=0}^{N} P_{\text{opt,i}}(t) = \sum_{i=0}^{N} P_{\text{avg},i} + \Delta P_i \sin(\omega_i t)\,. \tag{2.15}$$

with $P_{\text{opt,i}}$ as defined in Equation (2.3). The splitting factor of the tap is depending on the system design because a trade-off has to be done. When a high percentage (> 15%) of the incoming signal is coupled out, the pilot tones can be more easily received but also the signal is lowered by this high percentage. Vice-versa, if only a small percentage is coupled out, the data signal has only small loss but the reception of the pilot tones is more challenging. A typically ratio for wavelength and power monitoring are couplers with small percentage, e.g. 90%/10% or 95%/5%.

The low-pass filter cut-off frequency must be chosen higher than ω_N and preferably as low as possible to avoid noise from the data transmission spectrum. The optical power P_i of each channel can now be calculated by detecting the amplitude ΔP_i of the spectrum at each pilot tone frequency ω_i and multiplying it with the modulation index m. This means that by calculation of the amplitude spectrum of the low-pass filtered signal the amplitude of all optical channels can be calculated in one step.

Note that this principle will be used for the tuning algorithms explained in the next chapter. There, the power-amplitude dependency will be used to detect whether an optical transceiver is correctly tuned to its target channel. In this section, the accuracy of different amplitude spectrum calculation methods will be evaluated.

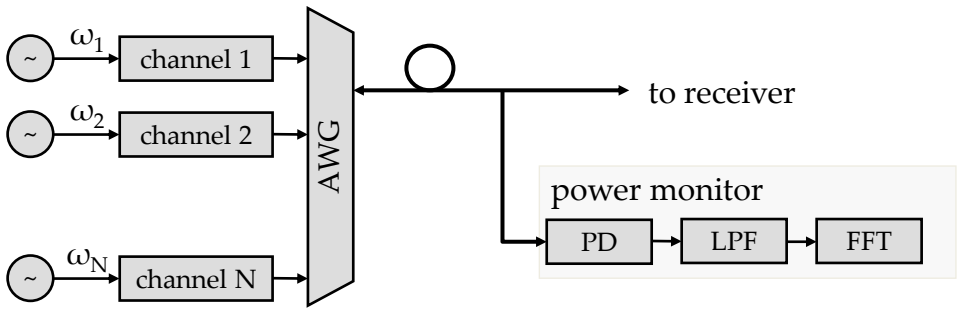

Figure 2.18: Simulated system to monitor optical channel powers of an optical WDM signal

2.4.2 Signal parameter estimation

Estimating parameters (amplitude, phase and frequency) of sinusoids in the presence of noise is a basic problem in signal processing and has been the object of many publications, e.g. [62]. Especially, the detection and estimation of small amplitudes near to large ones in the spectrum is a challenging task as the high amplitudes effect the exact estimation of the lower amplitudes. This translates to an optical channel with a high optical power next to an optical channel with a very low power. A classic approach is applying a window function, e.g. [63], to the incoming signal and to calculate the digital Fourier transformation (DFT), preferably via the fast Fourier transformation (FFT). However, the early published window functions were not suitable for a higher dynamic ranges and only useful for amplitude detection and not for amplitude estimation. The dynamic range is the ratio between the largest and smallest values of the signal. In [64] and [65], new windows were presented, which solve these weaknesses. Figure 2.19 shows the transfer functions of the 4 windows used in the simulations:

- Nuttall3a and Nuttall4c [64]
- high dynamic range flattop (HFT) windows: HFT116D and HFT248D [65] .

In the following, numerical simulations were done to determine the SNR tolerance for different window types and finding the optimal algorithm dimensions.

2.4.3 Simulation details

For the numerical simulation, the simulated input signal consists of 96 sinusoids with frequencies from 100 kHz to 1050 kHz with a channel spacing of 100 kHz which match the range defined in Table 2.3. The frequency deviation is assumed to be random uniformly distributed with a maximal deviation of ± 300 Hz. The sinusoid phases are assumed

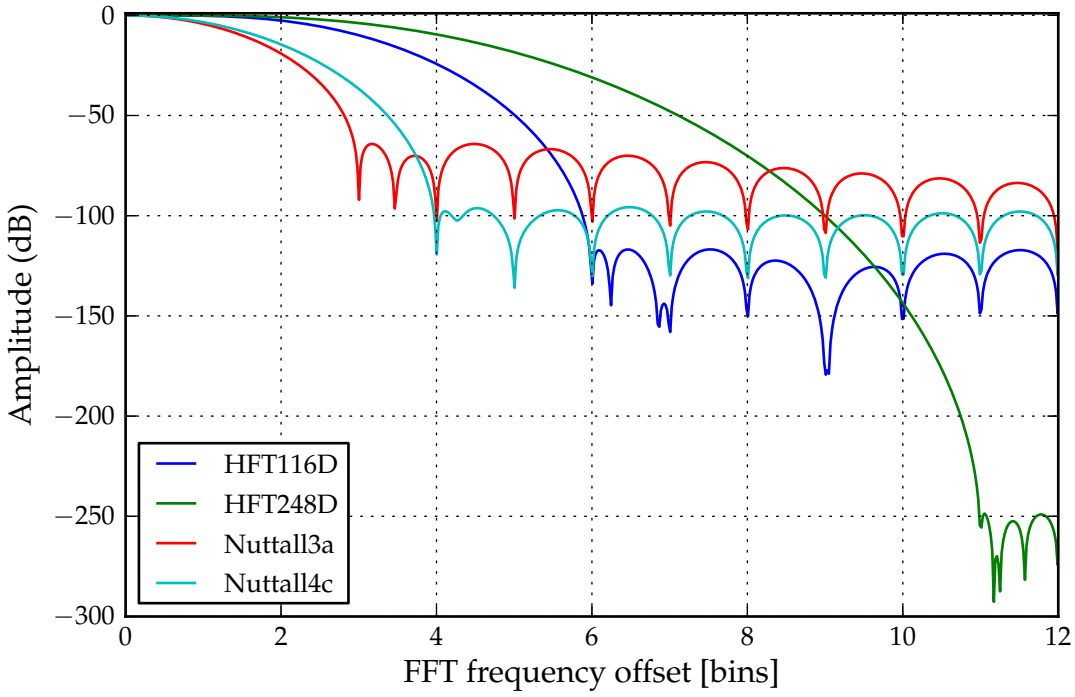

Figure 2.19: Transfer function of the window functions in the frequency domain

random and uniformly distributed. However, as the simulation results reveal, the distribution of the phases has no detectable influence on the amplitude estimation. Neither the likewise added limited analog-to-digital converter (ADC) resolution to 16 bit adds a mentionable additional error if the noise is within a reasonable level and the dynamic range of the input signal is ≤ 20 dB. In the following, two cases for the power amplitude distribution will be considered. The first case is the most challenging with an alternating series of minimal and maximal amplitudes (worst case). For the second case an uniformly distributed random distribution of amplitudes is assumed (random case).

Dynamic range and amplitude resolution

A window function has a certain dynamic range up to which it can be used reasonably. The dynamic range is limited by the scalloping loss of the FFT. Therefore, the rejection of the side lobes is the dominant factor in dynamic range simulations. Figure 2.20 shows the maximum amplitude error for the 4 window functions over a dynamic range of the input signal from 0 dB to 35 dB without noise. For a dynamic range below 25 dB, all windows show an amplitude error < 0.5 dB. As seen from Figure 2.20 the HFT windows perform way better than the Nuttall windows (0.001 dB vs 0.15 dB). The rapid raise of the amplitude error over 25 dB dynamic range is caused by the limited amplitude resolution and

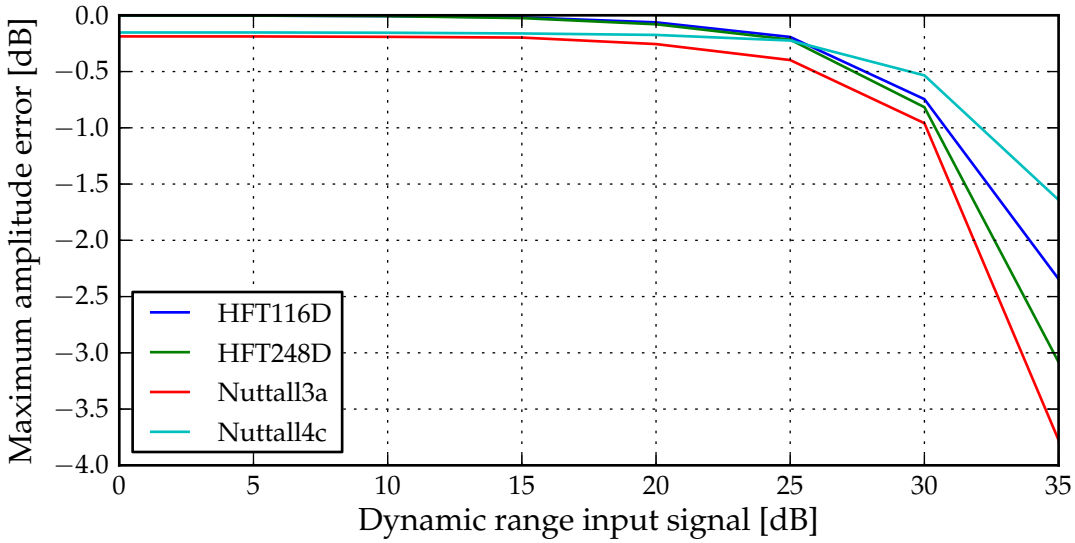

Figure 2.20: Simulation results varying the dynamic range of the input signal with the 4 window types; simulation without noise

not by the side lobes of the windows. Simulations with unlimited amplitude resolution in the time domain show that the side lobe caused error starts to become higher for a dynamic range above 35 dB. In the following simulations, the dynamic range will always be kept constant at 15 dB and therefore 10 dB under the margin.

SNR sensitivity

One of the most important factors for evaluation of a window function is the performance of the window in presence of noise. Therefore the parameters of Table 2.5 were used for simulation.

The simulation for each window was repeated 100 times, with white Gaussian noise and random frequency offset. Figure 2.21 shows the results for both cases: worst amplitude distribution case is shown in Figure 2.21a and random amplitude distribution in Figure 2.21b. It can be seen in the worst case that for a low SNR the Nuttall windows have better results than the HFT windows. For a high SNR however, the HFT windows are more suitable, as their maximal amplitude error is lower. This behaviour can be explained by looking at the spectral domain of the two window types, see Figure 2.19. The Nuttall windows have a smaller main lobe, so they "collect" less noise, but their side lobe suppression ratio is lower than HFT windows, and therefore the best achievable performance is worse. Even with higher SNR and without noise the Nuttall windows have an error of $\sim$0.5 dB. The results for the random amplitude distribution show a

similar performance of the windows, see Figure 2.21b, of course the error values are smaller. Additional to the maximum amplitude error also the average amplitude error over all tones has been calculated. Figure 2.22 shows the results for both cases. The big difference between maximum and average error is caused by the fact that mainly the small amplitudes get affected by noise and leakage. The error for the big amplitudes is negligible. The difference between the worst and the random cases originates mainly from the fact that the worst case has more small amplitudes, which are affected by noise.

parameter	value
FFT Length	$2^{12} = 4096$
sample rate	4096 kHz
dynamic range	15 dB
ADC resolution	16 bit

Table 2.5: ECC frame content from OLT to ONU

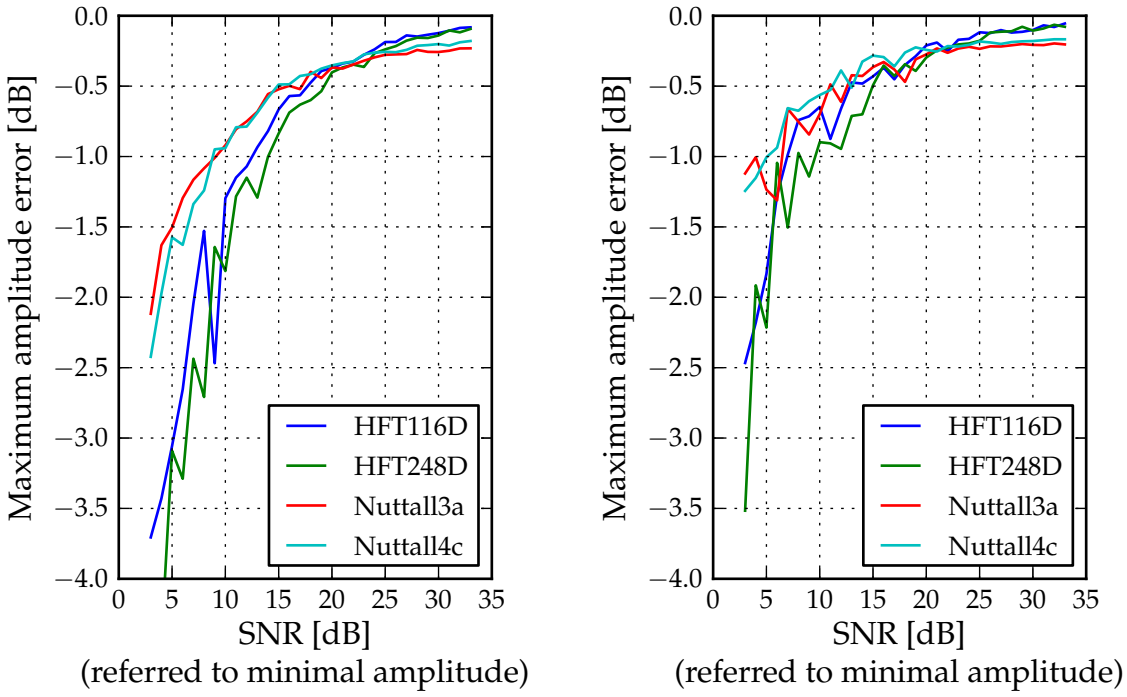

(a) Worst case

(b) Average case

Figure 2.21: Maximum amplitude error over varying SNR of the input signal with 4 window types

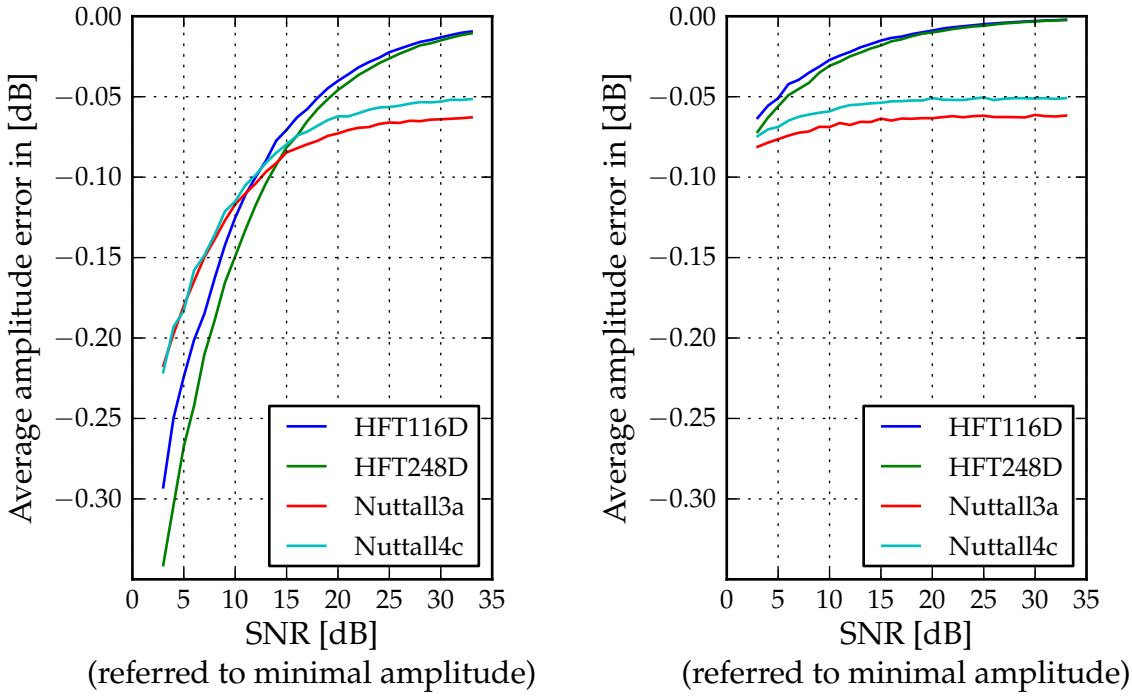

(a) Worst case

(b) Average case

Figure 2.22: Average amplitude error over varying SNR of the input signal with 4 window types

2.4.4 Averaging vs longer DFT

For obtaining better results, more sample points can be taken. In general, two methods are known to take an advantage of these additional samples. Either the FFT length can be made longer or several short FFT calculations can be averaged. Looking at the computational effort, the longer FFT increases by $n\log(n)$, while the averaging method has a linear increase in complexity.

The averaging method can be enhanced by overlapping several FFTs as otherwise the information in the first and last samples would be lost as the window functions are normally zero or close to zero. [65] gives the optimal overlapping factors for each window. This factor has to be added to the computational effort. The simulations results with longer FFT lengths can be seen in Figure 2.23a, and the averaging results with optimal overlap for each window in Figure 2.23b. Both methods can reduce the error but especially for low SNR the average method is performing better and is additionally cheaper in terms of computation. The average error is not plotted, but behaves in a similar way.

2.4.5 Window conclusion

The simulation results show that Nutall windows only show a better performance than the HFT windows, if no averaging is used and the signal has a low SNR of $< 15\,\mathrm{dB}$. In all other cases, the HFT windows HFT116D and HFT248D show better performance, especially, if a signal has a high SNR. Independently of the window used, averaging over several calculations lowers the estimated amplitude error significantly. Summarizing the numerical results, it can be concluded that for a high precision detection of amplitudes, the HFT248D window with a averaging over several FFTs has the best performance.

2.4.6 Further considerations

The results shown here cover only a part of the possible parameter space for dimensioning the signal processing for the detection of pilot tone amplitudes. All considerations were done with the sample frequency of 4096 kHz. There is a lower bound for the sample frequency of 2200 kHz given by the Nyquist criterion. The upper bound for the sample frequency is 40 960 kHz due to the necessary frequency resolution of 1 FFT bin to be maximal 10 kHz. Within this interval, the simulations show that, given a fixed FFT length, a lower sample frequency and so a less accurate frequency resolution leads to better results. This effect is mainly seen in the average error. It is caused by the fact that less noise is going to be seen by the actual bin. Every window shown here, actually every

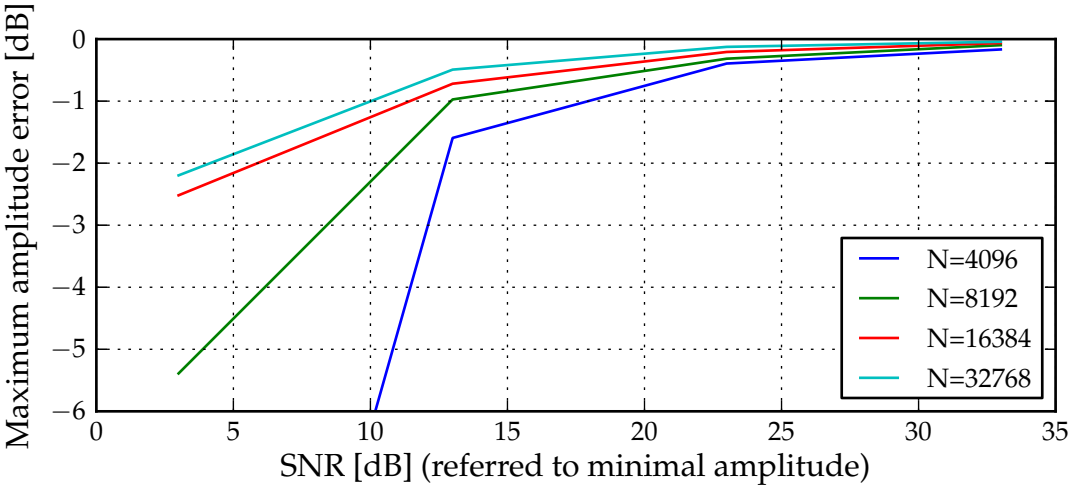

(a) Results of 1 large FFT with length N of a input signal with L=N samples

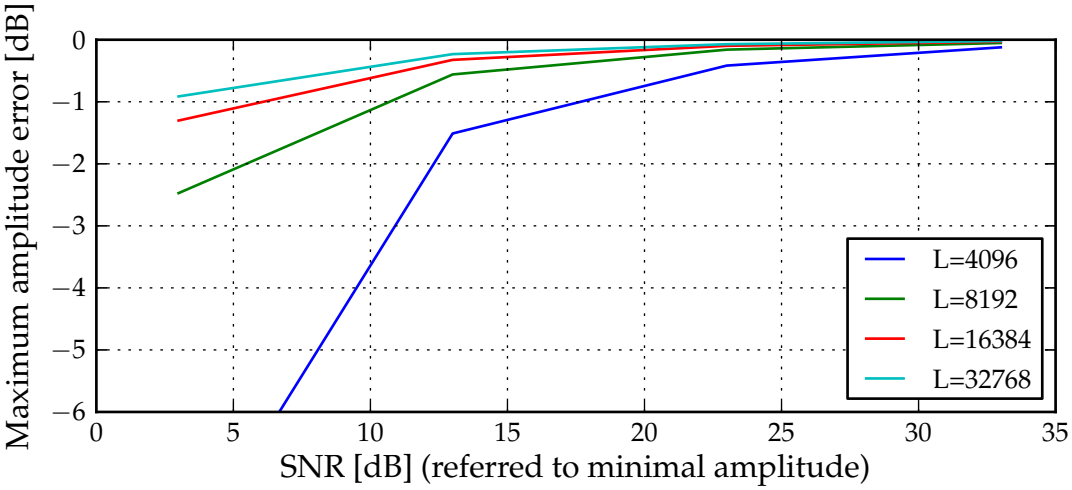

(b) Averaging the results of input signal with L samples over the several overlapping FFTs of length 4096

Figure 2.23: Improving the results with the usage of more samples with the HFT248D window

window except the rectangular, has a normalized equivalent noise bandwidth (NENBW) higher than one. So for inaccurate resolutions there is a scalloping effect of the main peak.

2.5 Chapter conclusion

In this chapter, existing pilot tone generation methods were compared to a new method which uses a modified 8B/10B encoder to generate a pilot tone. A real implementation in an FPGA of the new method was used to compare its performance with the existing one. As the results reveal, the new method shows the same performance as a signal without pilot tone and can be used with standard optical transceivers. Table 2.4 summarizes the findings and can be used as a decision finder. Secondly, a method which estimates the power levels of a wavelength-multiplexed signal with unique pilot tones was presented. Therefore, it is necessary to calculate the pilot tone amplitude spectrum of the low-pass filtered signal. Numerical simulations were done to determine the accuracy of different signal processing methods with regard to different SNR levels. With the usage of a window function and an FFT, all pilot tone amplitudes and thus the optical power levels of the multiplexed signal can be determined in one step. With the HFT windows, an average amplitude error of < 0.1 dB can be achieved. This accurate pilot tone amplitude detection enables to accurately estimate the optical power level of the optical signal. This enables the usage for different monitoring applications, such as wavelength control.

The findings of this chapter will be used in the following chapters, where pilot tones and their amplitudes are used to remotely control the lasing frequency of a tunable transceiver.

3 Wavelength control in WR-WDM-PONs

3.1 Chapter preface

In this chapter, a standard tunable transceiver used in today's WDM systems will be described. The hardware design, including the components, of such a transceiver is not suitable for the cost sensitive mass market of residential access. Therefore, it is necessary to understand what the main cost drivers are and how their cost can be lowered or completely avoided by changing the system design. Different methods of lowering the costs are described in this chapter. Finally, implementations of these methods will be reported and their experimental results will be discussed.

3.2 Full band tunable transceivers

In older core WDM networks, only fixed wavelength, so-called coloured, transceivers have been used due to the lack of tunable lasers. With the availability of tunable laser sources, operators have begun to replace the fixed wavelength modules by variants with tunable lasers. The replacement with tunable wavelength modules is mainly driven by the savings in the operational complexity. It is easier to handle one item in purchase, replacement and installation than a multitude of similar items only differing in wavelength. While fixed wavelength modules may be controllable for backhaul systems, in mass-deployments, like WDM-PONs, the operators strictly forbid the usage of fixed wavelength interfaces. Therefore, it is important to understand the functionality of current tunable transceiver.

An optical transceiver normally contains the following parts:

- Receive direction
  - Photo diode: avalanche photo diode (APD) or positive intrinsic negative diode (PIN)
  - TIA to convert current to voltage and increase the impedance
  - Limiting amplifier (LA) to normalize the voltage to predefined '0' and '1' voltage levels

  - Clock and data recovery (CDR) (only XFP) to minimize jitter

- Transmit direction
  - CDR (only XFP) to minimize jitter
  - Laser driver to convert the voltages into injection currents and to adapt the impedance
  - Laser diode with monitor PD to control the output power

- General
  - Micro controller (μC) for monitor and control functionality
  - Etalon filter for wavelength control (in a tunable transceiver only)
  - Thermoelectric cooler (TEC) to regulate the operating temperature of the laser chip
  - Receiver (RX) and transmitter (TX) optical little connectors (LCs)

These parts can be either integrated into a pluggable module (SFP [66] / XFP [67]) or be mounted on a line card. Figure 3.1 shows a functional block diagram of the components.

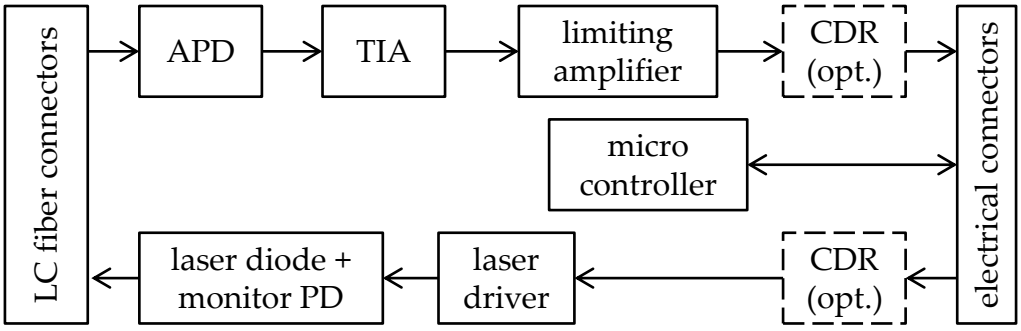

Figure 3.1: Optical transceiver block diagram

3.3 Local wavelength control

In a tunable transceiver, the lasing wavelength has to be monitored to ensure correct operation. The calibration of the laser currents is done so that the laser can be turned on within ± 15 GHz of the target grid frequency. Ageing and external effects can however effect the laser frequency. Therefore, it is necessary to have a frequency reference which allows to operate the laser within a smaller area around the target grid frequency, e.g. ± 2.5 GHz. This frequency reference is realised by coupling out a part from the transmitted laser light and filtering it using an etalon filter.

3.3.1 Etalon filter

The etalon filter or Fabry–Pérot interferometer is an optical periodic filter in which the light is reflected several times between two surfaces, see Figure 3.2. The phase difference

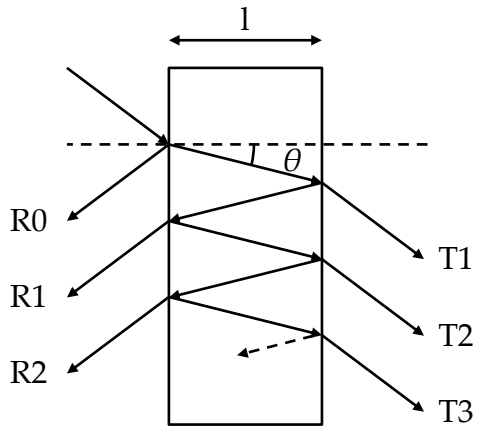

Figure 3.2: Etalon cross section

δ on each round trip, e.g. between T1 and T2, is given by:

$$\delta = \frac{4\pi n l \cos\theta}{\lambda} \tag{3.1}$$

where n is the index of refraction within the etalon, l is thickness of the etalon, θ is the angle of incidence and λ is wavelength of the light, see also [68, pp. 160–164]. Assuming the same reflectance R for both surfaces and F as coefficient for the finesse the transfer function can be calculated by:

$$T(\delta) = \frac{(1-R)^2}{1+R^2-2R\cos\delta} = \frac{1}{1+F\sin^2(\delta/2)} \tag{3.2}$$

$$F(R) = \frac{4R}{(1-R)^2} \tag{3.3}$$

The spacing of two periodic maxima is called free spectral range (FSR) and is normally chosen to be same as the WDM channel spacing, e.g. 50 GHz or 100 GHz. In order to locate the maxima δ_m, the derivative with respect to λ of the transfer function must be set to 0:

$$T'(\delta) = \frac{-F\sin(\delta/2)\cos(\delta/2)}{\left(1+F\sin^2(\delta/2)\right)^2} \stackrel{!}{=} 0 \tag{3.4}$$

$$\sin(\delta/2)\cos(\delta/2) = 0 \tag{3.5}$$

$$\delta_m = 2m\pi,\ m \in \mathbb{N}\ or\ \delta_n = (2n-1)\frac{\pi}{2},\ n \in \mathbb{N} \tag{3.6}$$

The FSR can thus be calculated with the usage of Equation (3.1) (analogue for δ_n):

$$\lambda_m = \frac{2nlcos\theta}{m} \tag{3.7}$$

$$v_m = \frac{c}{2nlcos\theta}m \tag{3.8}$$

$$FSR = v_{m+1} - v_m = \frac{c}{2nlcos\theta} \tag{3.9}$$

Finally, the transfer function as a function of f and FSR can be noted as:

$$T(f) = \frac{1}{1 + F\sin^2(\frac{\pi}{FSR}f)} \tag{3.10}$$

Figure 3.3 shows the etalon transfer functions for different finesses and an FSR of 100 GHz.

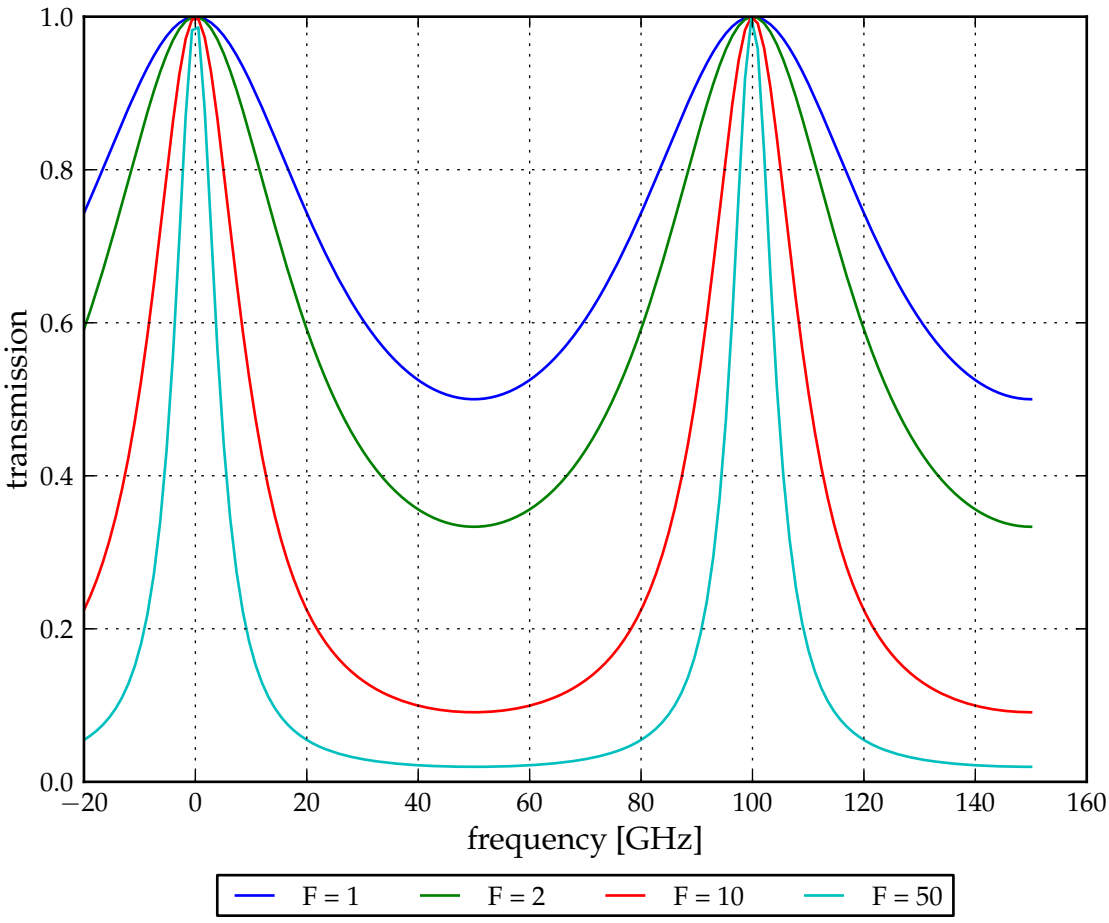

Figure 3.3: Etalon transmission transfer function for etalon with an FSR of 100 GHz and different values of finesse F

3.3.2 Control loop

The etalon and its transfer function are now used within a control loop. Within the transceiver a small part, e.g. 1 % to 5 % of the transmitted light is coupled out via a beam splitter and the transmitted and reflected light of the etalon are detected by two slow running photo diodes. Figure 3.4 shows a variant where the light is coupled out between the laser chip and the output fibre, and Figure 3.5 shows a variant with an external component. This external component including the photo diode is called wavelength locker or wavelocker. The following calculations, however, are the same for both component types as the reference PD signal can be calculated by the following equation

$$PD_{\text{reference}} = PD_{\text{transmission}} + PD_{\text{reflection}}. \tag{3.11}$$

After the signal reception, the mean power of both PDs is taken and the ratio r_{abs} is calculated:

$$r_{abs} = \frac{PD_{\text{transmission}}}{PD_{\text{reflection}}} \tag{3.12}$$

Using this ratio, it can be detected whether the current frequency is too low or too high. With this information the lasing frequency can then be changed accordingly to approach the target grid frequency. As this ratio is ambiguous the etalon needs to have an FSR at least the size of the WDM channel spacing, and the laser has to be pre-calibrated so that it will start lasing within the lock-in range (Δv_{lr}) of the desired channel.

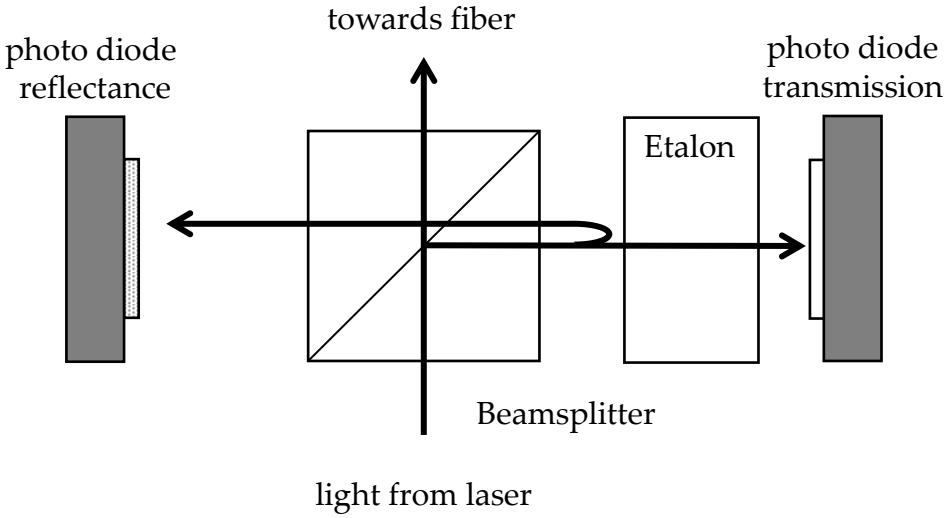

Figure 3.4: Local control detection. The reflected light into the laser is not drawn, as the laser is normally protected by an optical isolator.

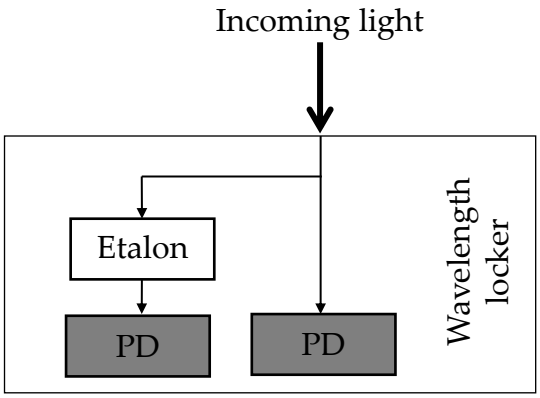

Figure 3.5: Wavelength locker device with etalon

Lock-in range

The lock-in range Δv_{lr} is defined as the frequency range where a frequency error can be calculated correctly in order to reach the target frequency f_t. The frequency range is then given by

$$\Delta v_{lr} = f_a - f_b. \tag{3.13}$$

Figure 3.6 shows a graphical representation of the lock-in range. If the frequency is

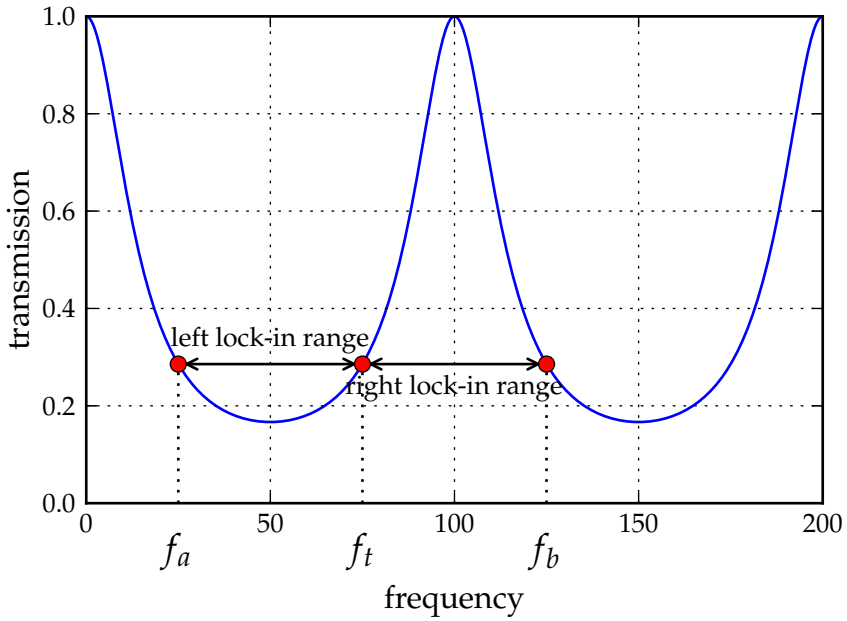

Figure 3.6: Etalon lock-in range with $F = 5$

outside the lock-in range it will be detected as belonging to the next lock-in range and the correction information will be calculated towards another locking point $f_{lock} = f_t + nFSR$, $n \in \mathbb{Z}$. Therefore the left $(f_t - f_a)$ and right $(f_b - f_t)$ side lock-in ranges should be as large and as symmetric as possible. This symmetric lock-in range $(\Delta v_{lr,sym})$ can be

defined as:

$$\Delta v_{lr,sym} = min\left\{f_a - f_t, f_t - f_b\right\} \tag{3.14}$$

and is expressed by:

$$f_{mod} = f \bmod \frac{FSR}{2} \tag{3.15}$$

$$\Delta v_{lr,sym}(f_{mod}) = \begin{cases} \frac{FSR}{2} - 2f_{mod} & \text{if } f_{mod} \leq \frac{FSR}{4} \\ 2f_{mod} & \text{if } \frac{FSR}{4} < f_{mod} \leq \frac{FSR}{2} \end{cases} \tag{3.16}$$

As it can be calculated from Equation (3.16) and also be seen from Figure 3.7 the largest value for $\Delta v_{lr,sym}$ is reached at $f = \frac{FSR}{4}$ and $f = \frac{3FSR}{4}$. One point lies on the rising and the other on the falling edge of the etalon transfer function. At these points, the left and the right hand lock-in range are equal. The maximal symmetrical lock-in range for a given FSR is

$$\Delta v_{lr,sym,max} = \frac{FSR}{2}. \tag{3.17}$$

The frequency offset of the etalon transfer function should thus be chosen that this maximal symmetrical lock-in range is reached at the target frequency. In the case where the FSR is equal to the channel spacing this will then automatically fit for all the other channels.

Finesse

Additionally to a high symmetrical lock-in range, it is desirable to have a high slope at this locking point, as a higher slope results in a higher sensitivity. The finesse with the maximum slope at the point with the maximum lock-in range ($f = \frac{FSR}{4}$) can be determined by calculating the maxima of the slope function $T'(F)$.

$$T''(F, f = \frac{FSR}{4}) \stackrel{!}{=} 0 \tag{3.18}$$

$$\frac{\pi F}{FSR\left(\frac{1}{2}F + 1\right)^3} - \frac{\pi}{FSR\left(\frac{1}{2}F + 1\right)^2} = 0 \tag{3.19}$$

$$F = 2 \tag{3.20}$$

As seen from the equation, a finesse of 2 has the highest slope at the point with maximum lock-in range. Most etalons designed for wavelength locking have low finesse (< 5).

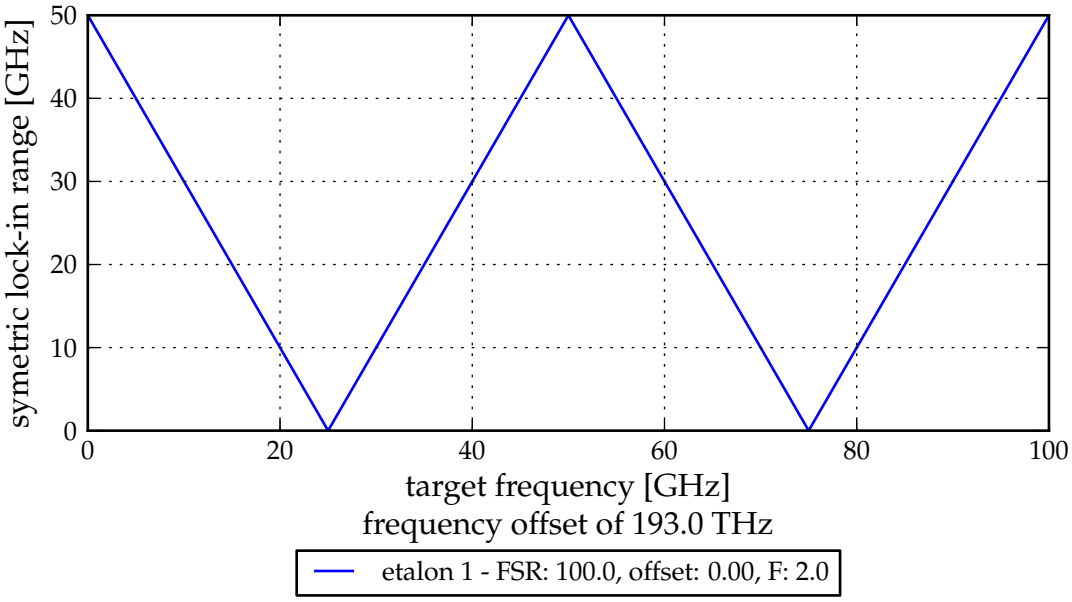

Figure 3.7: Single lock-in range, FSR = 100 GHz, the grid frequency is at f = 0

However, not obligatory a finesse of 2 as the finesse is dependent on the reflectance, see Equation (3.3), and the reflectance may not always be chosen freely as also other design criteria have to be met.

Applications

For most wavelength locking applications the rising edge is used as here a smaller ratio is equivalent to a lower (smaller) frequency. Alternatively, another application is the use of both the falling and the rising edge. Then the FSR is twice the WDM channel spacing. This reduces the maximal lock-in range by a factor of 2. Mostly, this principle is used when the system capacity is doubled from an existing WDM channel spacing, i.e. 40x 100 GHz channels to 80x 50 GHz channels). Then the already installed etalons do not need to be changed.

It can be summarized that the etalons used in the tunable transceivers and external wavelength lockers have to be designed with the following properties: The absolute frequency offset has to be set so that the point with maximum lock-in range is on the grid frequency. The FSR needs to be equal to the channel spacing as then all lock-in points are on the target grid. Finally, the finesse of $F = 2$ has the highest slope and thus the highest sensitivity at the lock-in point.

3.4 Lowering cost of a tunable laser assembly

As mentioned before, tunable transceiver products cannot be used in PON applications mainly due to their high price, but also due to their high energy consumption. The total cost of any optical component consists of material and manufacturing costs. The manufacturing costs are the major contributor for tunable laser assemblies to the overall cost and can be separated into two steps: assembly with packaging and calibration with function testing. For one full C-band tunable laser the calibration with function testing can take up to 2 hours.

One part of the material costs is the etalon filter which provides a wavelength reference for wavelength control. See Section 3.3.1 for a detailed explanation on the usage of the etalon filter as a wavelength reference. However, it is possible that the local wavelength control in the ONU can be omitted and be replaced by a centralised one. By leaving out the etalon not only the component costs can be reduced but also lower manufacturing costs are achieved as less components need to be assembled. In Section 3.5 this possibility will be explained in detail and also be validated experimentally.

The next component that adds major costs to the transceiver is the tunable laser chip. The main problem is not the laser chip itself which can be produced cheaply on a wafer scale. However, each laser chip needs a full calibration of the injection currents due to imperfectness during the production process of the wafer. This calibration is done during manufacturing and is needed to ensure a stable and fast operation of the wavelength tuning. A possible approach for lowering the manufacturing costs is to drastically reduce or omit the calibration process. Instead, the laser is tuned by general equations of the injection currents which are device independent. It is clear that these equations cannot offer such a high-end performance as calibrated lasers, but it can be shown that their performance is still enough for PON applications.

To furthermore reduce the cost, but mainly for reducing the energy consumption, an option is to remove the temperature controller, i.e. TEC, from the module. The laser then has to operate in an environment with changing temperature which affects its lasing frequency. This can also be compensated by generic temperature dependent equations.

The calibration-free and also TEC-less operation of the ONU laser are both optional and can be implemented independently from a network wavelength control. Therefore, these two approaches are discussed separately in the next chapter, in particular see Section 4.3.1 for detailed explanations on calibration-free and TEC-less operation of tunable lasers.

3.5 Network wavelength control for WR-WDM-PON

As discussed before, one way of lowering the cost of the tunable ONU transceiver in a WR-WDM-PON system is to centralize the wavelength control. This centralised approach enables the sharing of component costs. Figure 3.8 shows a complete WR-WDM-PON system including the centralised network control. The figure shows that the C-band is used for upstream and the L-band for downstream communication. In the OLT two arrays for the multiplexing and demultiplexing of the optical channels are used. Upstream and downstream directions are coupled to the feeder fibre with a C/L band splitter (combiner). The splitter has a low insertion loss ($< 2\,\mathrm{dB}$) at the operating wavelength range, and the gap between the bands is wide. At the RN the channels are separated and transmitted via the drop fibers to the ONUs. The same C/L band splitter as in the OLT is also used in the ONUs. In transmit direction the C-band port of the band splitter is connected to the tunable laser and the receive direction (L-band) to a PD.

For centralising the wavelength control in a WR-WDM-PON, any transmission parameter which is dependent on the frequency offset to the target frequency can be used. For ease of the usage it should be possible to measure this frequency offset without special, meaning expensive, equipment. For example [69] showed a system using the back reflected signal from the remote node's AWG. For detailed overview of more variants, see the author's paper [70].

All wavelength control loops can be differentiated into open and closed loop schemes. In an open loop system, the ONU tries to set the parameters without any feedback from the OLT. The disadvantage of this scheme is clear: In case of any unpredictable error the ONU is wrongly tuned without knowing it and the service may not work. A better performance is therefore achieved by using a closed loop. Here, a tuning information is sent back to the ONU, so that it can continuously optimize its tuning parameters. This back signalling is done from the OLT to each ONU separately via a dedicated embedded communication channel (ECC). The ECC from the OLT to the ONU is indicated in Figure 3.8 by the red dashed lines. This ECC can either be embedded within the data stream or encoded in a low bit rate pilot tone communication channel, e.g. with the parameters described in Section 2.3.

3.5.1 Optical power based method

An advantage of a WR-WDM-PON is the easy detection of the power per channel at the OLT. After the demux AWG the power can be either measured by a low-speed photo diode or by using the RSSI output port of the TIA or LA, see the array of channels at point

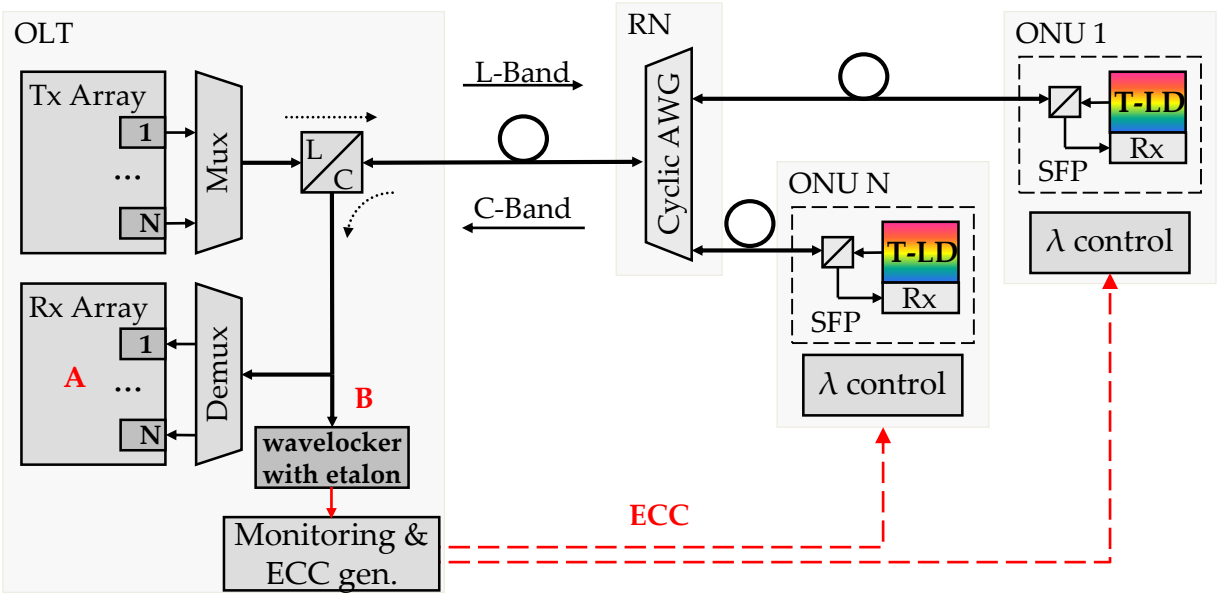

Figure 3.8: Centralised network wavelength control in a WR-WDM-PON using a shared wavelength locker in OLT and showing the dedicated ECCs

A in Figure 3.8. In the simplest feedback loop, the OLT measures the received upstream optical power in the channel under consideration. The OLT then signals the tuning information back to the ONU via the ECC. The ONU is hence tuned by maximizing the received power at the OLT whose value is received via the ECC. This scheme preferably uses AWGs (in the RN and OLT) with Gaussian passband characteristics since then a hill-climbing algorithm can be used to find the passband optimum. This scheme will result in rather low tuning accuracy when used with a flat-top shaped AWG passband as here the maximisation of the power is not evident. Figure 3.9 shows both passband shapes: Gaussian and flat-top, demonstrating the clear transfer maximum for Gaussian form, while the flat-top has a flat range, for which no clear maximum can be determined, such that the exact grid wavelength cannot be determined. In general, the optical power based tuning is easy to realise and a good performance can be achieved, see [71]. However, certain applications may contradict the usage of Gaussian-shaped AWGs and also their availability may not be given. Especially, if a large operation temperature range has to be met the AWGs are mostly flat-top so that a temperature introduced shift of the passband does not change the insertion loss.

3.5.2 Pilot-tone based method

More sophisticated, yet low-cost capable tuning methods make use of individual per-wavelength pilot tones. These tones are used to identify the correct wavelength under

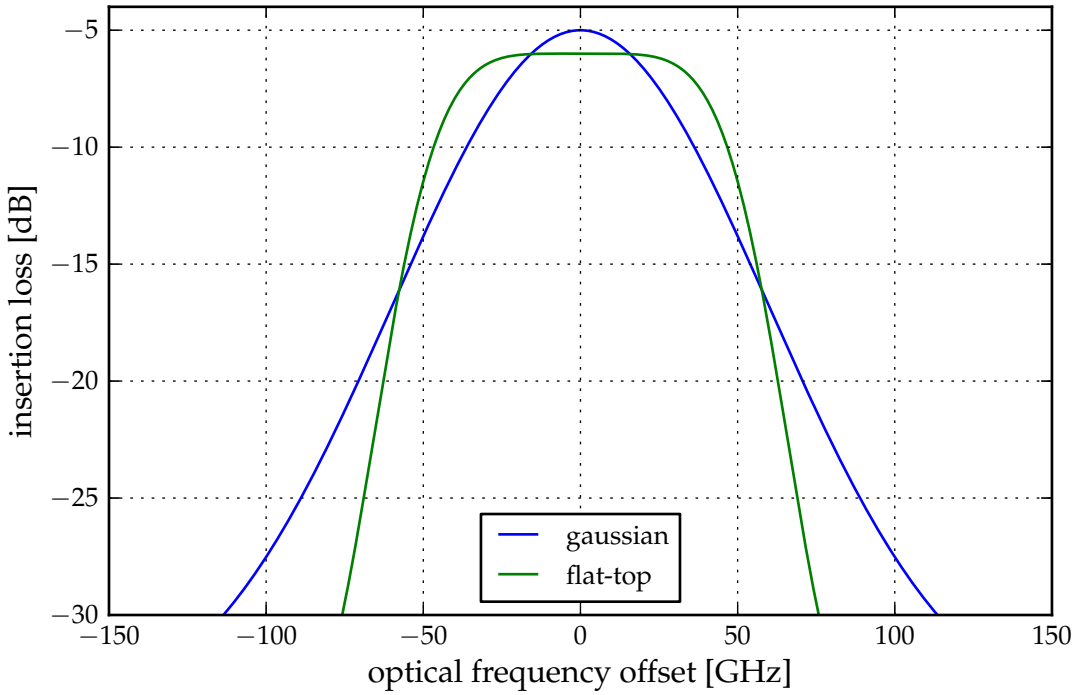

Figure 3.9: Passband shapes of AWGs

consideration and provide the information which is required for correct tuning. In an optical multiplexed signal also the pilot tone frequencies are added up spectrally. If the ONUs now use unique pilot tones, it is still possible to determine the optical channel under consideration by its pilot tone frequency.

Power estimation using pilot tones

One application of these pilot tones is the measurement of optical powers via the pilot tone amplitudes in the optical multiplexed signal. Therefore a small part is coupled out from the multiplexed signal and detected by a low bandwidth PD. This is equal to the reference PD at point B in Figure 3.8.

For every channel the optical power can be estimated by detecting its pilot tone amplitude and dividing it by its optical modulation index. Figure 3.10 shows a measurement where the optical input power to the wavelength locker was varied and the pilot tone amplitude was calculated. The measurement for each optical input level was repeated 20 times, and also the error bars are given. The measurement shows the linear dependency, and it is possible to use this principle down to $\sim -40\,\mathrm{dBm}$ until the error caused by the noise gets too high, see Figure 3.11.

The advantage of the calculation of the received optical power at the reference PD is that the optical power can be calculated in parallel for all optical channels, and it is not

necessary to get the values from N different electrical lines.

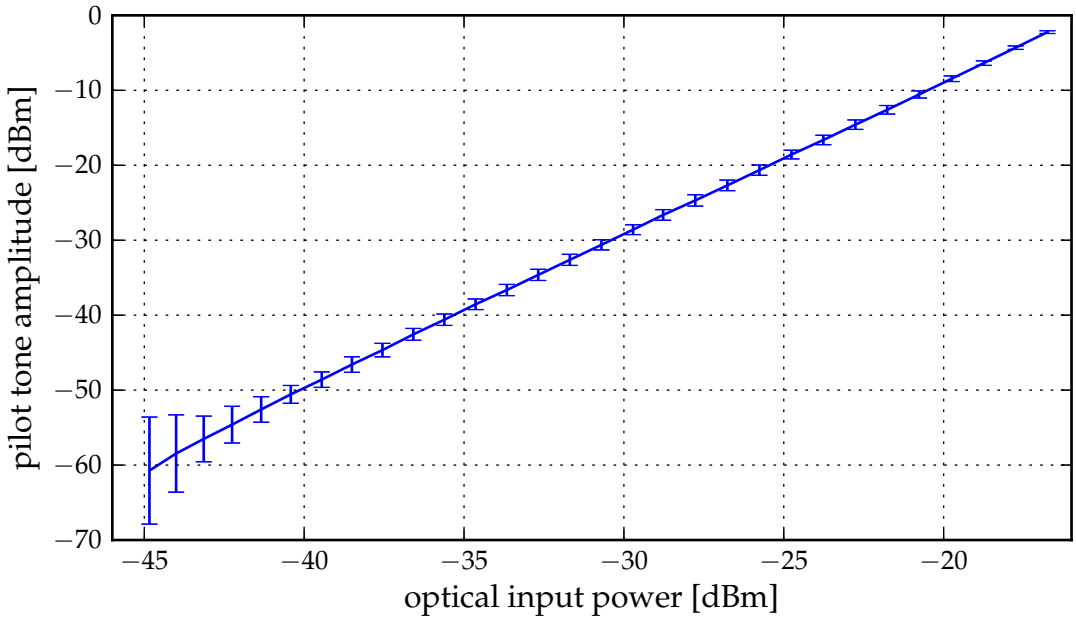

Figure 3.10: Mean pilot tone amplitude vs. optical input power; including error bars of 20 measurement repetitions

Wavelength locker ratio

As the optical wavelength can be identified by their pilot tones it is also possible to place a shared centralized etalon filter in the OLT - instead of individual wavelength lockers in each ONU. The centralized locker is located after a tap-coupler and is shown in Figure 3.8 at point B. The component was already shown in Figure 3.5.

The reference and the etalon PD can be slow running as they only need to detect the AM tones applied by the ONUs. The tuning information is then calculated on the same principle as with the local etalon as described in Section 3.3.2. The principle is changed so that instead of the average signal ratio, the pilot amplitude ratio is calculated. The ONU then tries to change its lasing frequency until a target ratio is found.

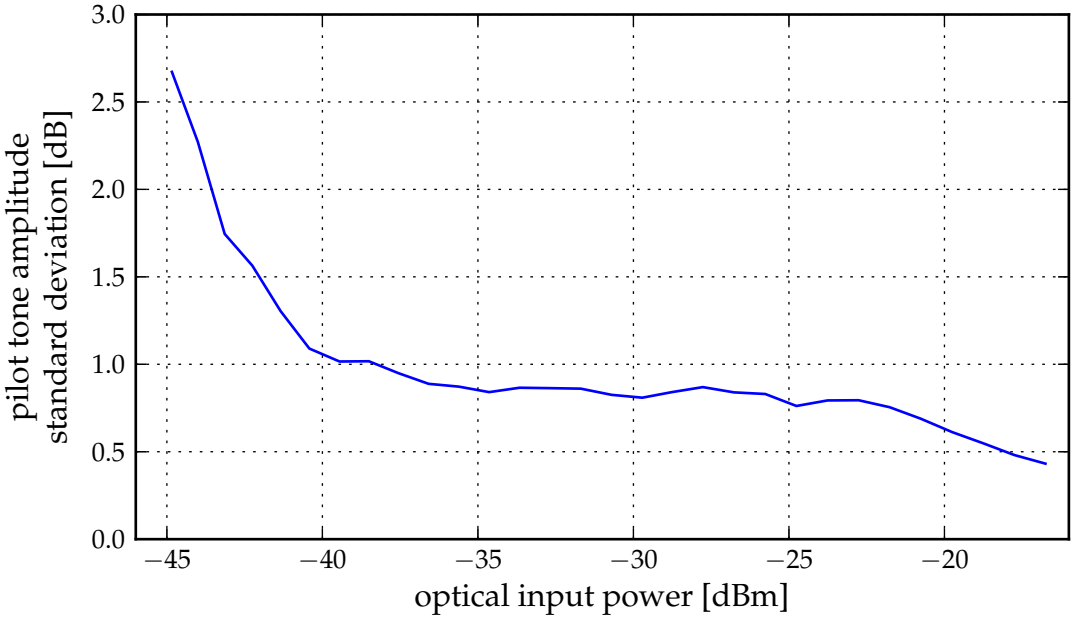

Figure 3.11: Pilot tone amplitude mean standard deviation vs. optical input power; 20 measurement repetitions

3.5.3 Proposed & implemented combined tuning method

By using individual pilot tones for each ONU and the application of the power estimation and wavelength locker calculation method, a fast and precise network wavelength control scheme can be realised. The proposed solution is also cost-effective as the centralised wavelength locker is shared between all ONUs. The OLT measures and continuously sends back the optical power and the etalon ratio offset for each optical channel. This can be done in parallel for each ONU on their downstream wavelength using an ECC. The ECC is divided into frames each containing the wavelength tuning information from the last measurement.

Normalised wavelength locker ratio λ_{err}

To make the ratio etalon independent, it is preferable to first normalize the obtained ratio and then send back its value to the ONU. Instead of the actual calculated ratio, a wavelength error λ_{err} is calculated. Using Equation (3.12), the wavelength error $\lambda_{err,i}$ for the optical channel i can be calculated to

$$\lambda_{err,i} = c_{\text{edge}}(r_{abs} - r_{\text{target},i}) \tag{3.21}$$

with $r_{\text{target},i}$ being the target ratio for the selected channel on the specific etalon transfer function. c_{edge} is either 1 or -1 depending on whether the operation point is on the raising or falling edge of the etalon transmission curve.

λ_{err} is a parameter which is 0 when the laser frequency is exactly on the target frequency and negative (positive) if the frequency is too low (too high). Figure 3.12 shows a measurement of λ_{err} as a function of the lasing frequency using a pilot tone with 200 kHz. The figure shows three 100 GHz channels with their lock-in points and lock-in ranges (double arrow). The λ_{err} in the figure is symmetric as the finesse of the used etalon was $\sim$1.2.

Note that the wavelength error λ_{err} still has ambiguity of the channel and only provides a valid information, if the current frequency lies within the lock-in range.

OLT ECC frame generation

With the usage of wavelength error the following information can now be sent to each ONU after each measurement. One ECC frame consists of: target optical channel (λ-ID), target pilot tone frequency (PT-ID), received optical power (OP-RX) and wavelength error (λ-error). Table 3.1 summarizes the parameters and explains how the values can be

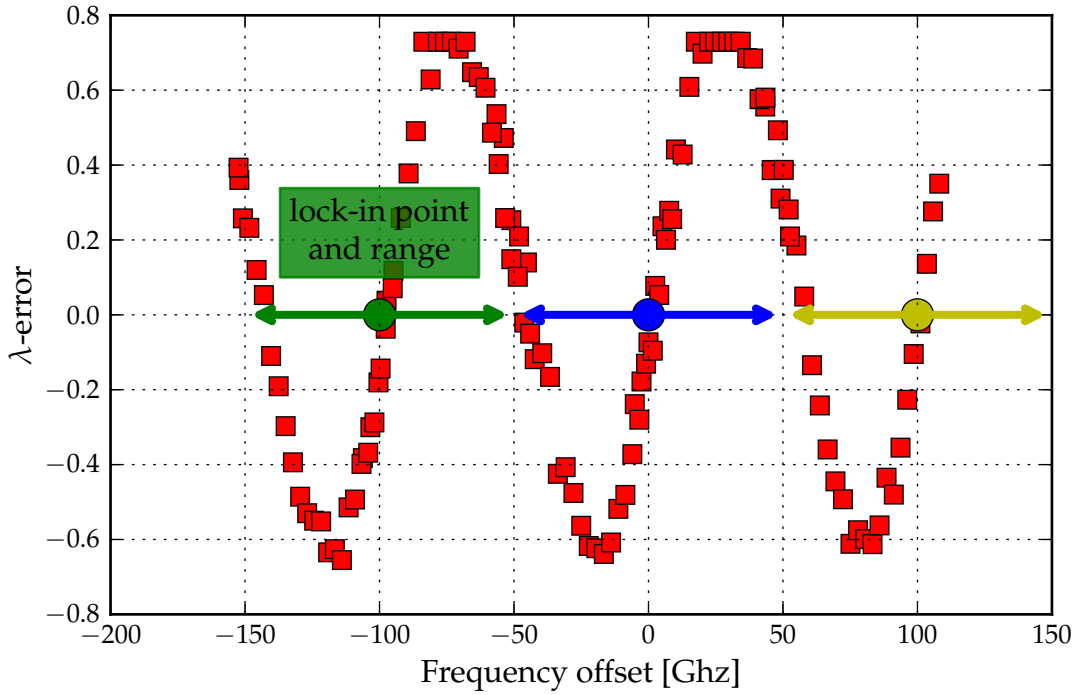

Figure 3.12: Lambda error measurement for a 100 GHz etalon including the lock-in point and range of different optical channels

calculated. Either λ-ID or PT-ID could be omitted, if a fixed allocation between the pilot tone frequency and the optical wavelength is used.

name	abbreviation	note / calculation method
optical channel number	λ-ID	unique value for each channel
upstream pilot tone frequency	PT-ID	unique value for each channel
received optical power	OP-RX	calculation via the pilot amplitude of the reference PD
normalized pilot tone ratio	λ-error	calculation via the pilot tone ratio between etalon and reference PD

Table 3.1: ECC frame content from OLT to ONU

Figure 3.13 shows the flow chart of the described process at the OLT. First, the signal from the reference and etalon PD is captured. Then, both pilot tone amplitude spectra are calculated. See Section 2.4 for amplitude spectrum computation methods. With the pilot tone amplitude spectra, the optical power and the wavelength error are estimated. Finally, the ECC frames for all ONUs are assembled and sent out to the respective ones.

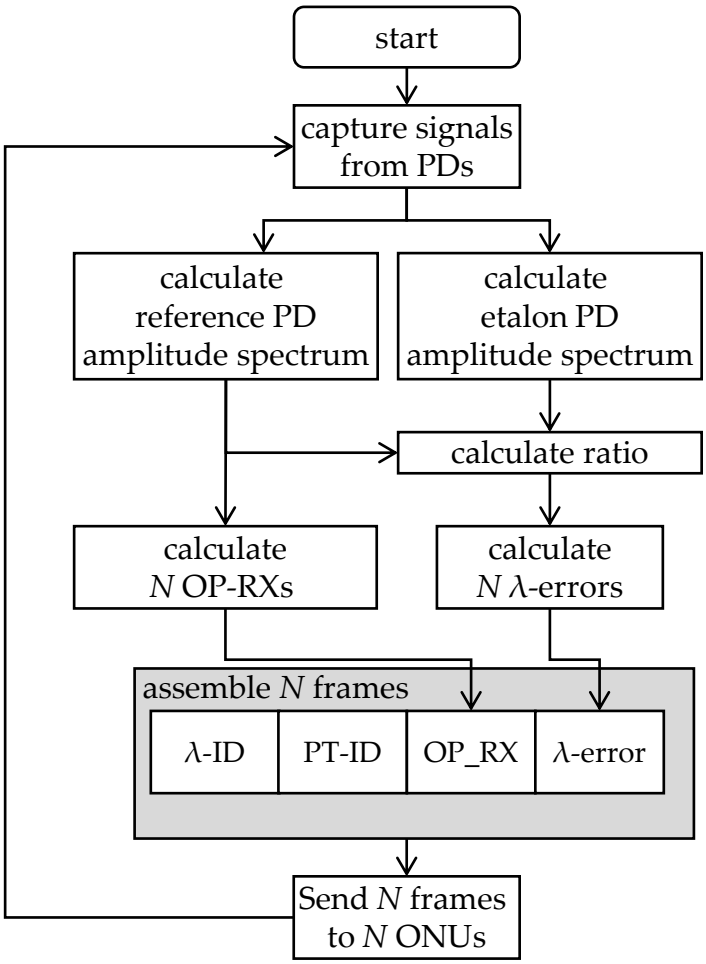

Figure 3.13: Simplified OLT flow chart for a network wavelength control

ONU initialisation phase

After connecting or powering on, the ONU starts with the initialisation phase. After the first reception of an ECC frame, the ONU knows which optical target frequency it needs to reach and which pilot tone to use. The ONU now tries to maximise the optical power seen at the OLT and communicated via the ECC frame. Depending on the implementation and the knowledge of the tunable laser module the ONU can either directly select the injection currents for the target channel or do a blind search. The blind search can be either in the full C-band, e.g. by stepping from the lowest to highest optical frequency. This for example could be done without calibration data. Alternately, in the case that a partial calibration was done, the search can also be done within a sub-band. In any case, the new ONU doesn't disturb the other already existing channels even when setting a wrong frequency because the AWG in the remote node suppresses the cross talk from adjacent channels by at least 35 dB.

After the received optical power is higher than a predefined threshold value the initialisation phase is finished. The threshold depends on the system design and should be set $\sim$10 dB higher than the noise level observed when the laser is tuned outside of the passband of the AWG. After the threshold is reached, the optical frequency lies within the passband of the target channel. Then phase two for continuous tuning can start.

ONU operation phase

Additional to the received power, the ECC frame also contains the normalised λ-error. As already mentioned, this information is only valid, if the frequency lies within the symmetrical lock-in range $\Delta\upsilon_{lr,sym}$ of the etalon, see Section 3.3.2. In a WDM-PON with channel spacing of 100 GHz the lock-in range is $\pm$50 GHz from the target channel which is larger than the typical AWG passband width of $< \pm$20 GHz to 35 GHz, see Figure 3.9. Therefore, it is now safe to use the pilot λ-error information as the frequency lies within the lock-in range. The λ-error is then evaluated, and the laser is continuously fine-tuned with small tuning steps.

Figure 3.14 shows the flow chart of the described ONU process including the two phases. For a better overview, abort conditions are not included in the figure. E.g., if the optical power drops for several received frames under a loss of signal (LOS) level, a restart of the channel search needs to be triggered.

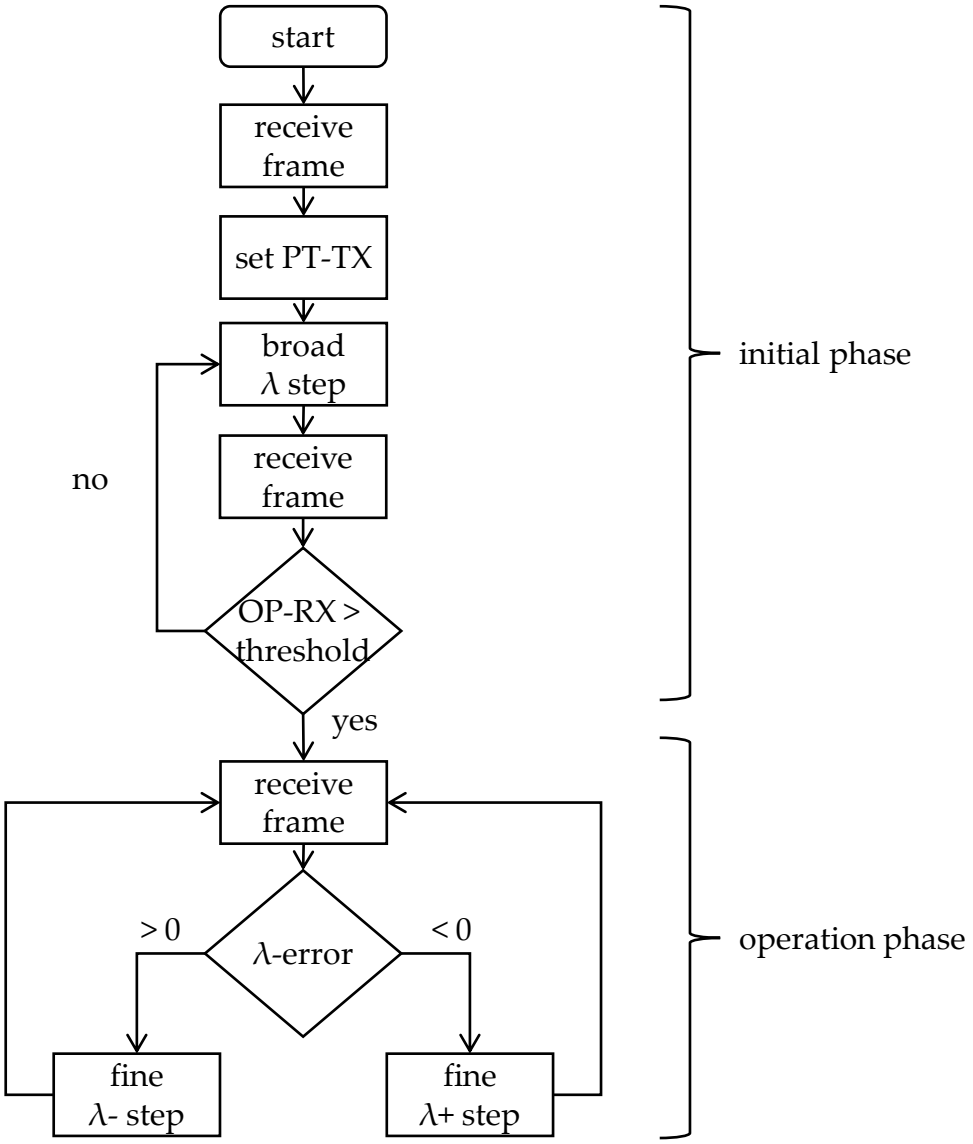

Figure 3.14: Simplified ONU flow chart for a network wavelength control

3.6 Experimental validation over a single fibre

The described combined network control was demonstrated in a full set-up, see Figure 3.15 and [72]. In the shown configuration the C-band was used for upstream and the L-band for downstream communication. The validation included initial tuning of a laser, as well as laser wavelength control in operation with stable ONU temperatures. Experiments within changing temperatures have also been deducted and will be presented in Section 4.2.2. In all configurations, the same control loops on OLT and ONU were used. Between OLT and ONU a 50 km standard single-mode optical fibre (SSMF) was installed to emulate realistic transmission distances. The generation of the pilot tone was done using an external function generator. In the experiment, the setting of the pilot tone frequency was done manually by setting the received pilot tone. However, in a fully integrated system this step can be done automatically, e.g. using a direct digital synthesis (DDS) chip.

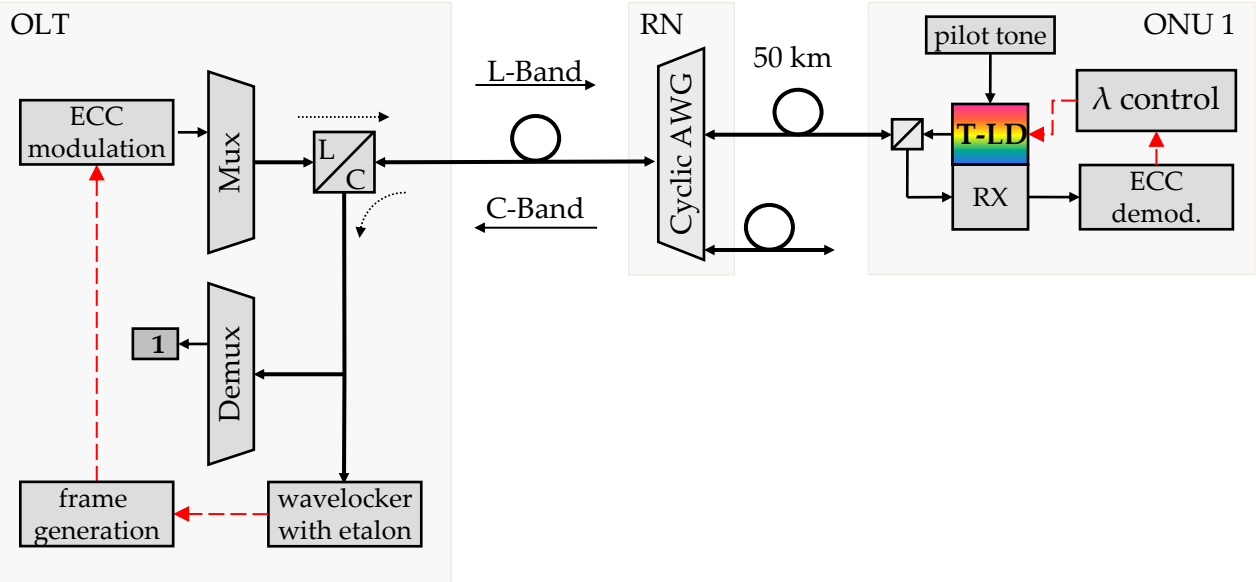

Figure 3.15: Network control experimental set-up

The ECC was transmitted back to the ONU on the fibre in the L-band. The optical downstream carrier was modulated with an 8B/10B encoded 1-Gb/s pseudo-random bit stream (PRBS) data stream and in addition with a 100 kHz tone, carrying the wavelength control information via 1-kb/s BPSK modulation. The parameters of Table 2.3 were used, and the modulation index was set to 10 %. In the experiment, the tone was modulated via a modification of the 8B/10B encoding, as described in Section 2.3.3. Including header and CRC data a frame rate of maximal 12.5 frames/s can theoretically be achieved. This rate was not reached in the experiment as the processing on the OLT side was done

on a standard personal computer (PC), on which the processing is slow with the used implementation. An effective frame rate containing tuning information of $\sim$1 frames/s was reached, while the remaining frames contained idle signals.

For each information field of the ECC frame, as described in Table 3.1, 1 byte was used. This resulted in only 4 bytes for the complete wavelength tuning information. Table 3.2 shows the data format of the 4 fields. Due to the limitation of 8 bit per information field the real transmitted values were rounded, clipped and truncated. Both the ONU and OLT were programmed to have the behaviour as shown in Figure 3.14 for the ONU and Figure 3.13 for the OLT. This resulted in frequency stepping as shown in Figure 3.16.

In this experiment, a sampled grating Y-branch (SG-Y) laser was used whose injection current curves were generalized in order to facilitate the operation and to reduce the number of calibration points needed for characterization. Section 4.7.5 will explain the tuning principle of the laser in detail. For the result discussed here, the laser can be assumed to be continuously tunable in wavelength without any mode jumps.

byte	name	abbreviation	note
0	target optical channel	λ-ID	192 THz + 100 GHz $\cdot$ λ-ID
1	target pilot tone frequency	PT-ID	100 kHz $\cdot$ PT-ID
2	received optical power	OP-RX	signed value in dBm
3	normalised pilot tone ratio	λ-error	signed value with 0 meaning grid frequency

Table 3.2: Downstream pilot tone ECC data

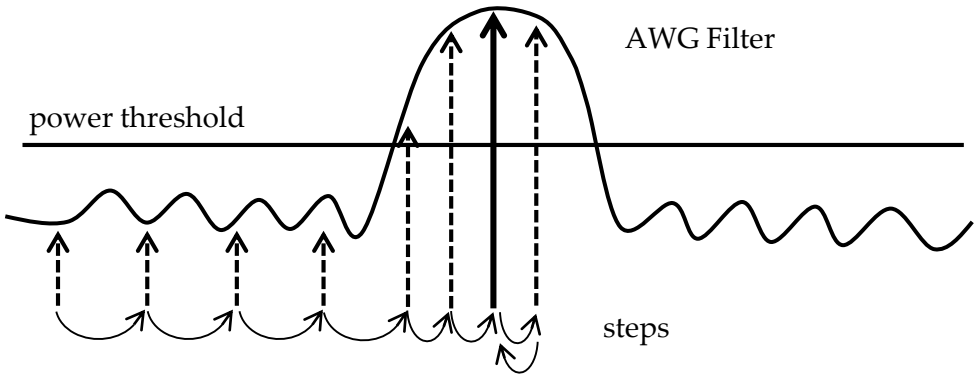

Figure 3.16: Frequency sweep on power-up

Initial phase

After the reception of the first ECC-frame the target optical channel is known to the ONU. Then the injection currents for a frequency, which is $\sim$400 GHz lower than the target

channel, were selected. From this point onward, the injection currents were changed stepwise. The frequency was increased with a step-size of ∼25 GHz until the received optical power at the OLT was higher than a pre-set threshold level, here −25 dBm. Figure 3.17a shows the measured lasing frequency during the turn-up and Figure 3.17b the optical received power. The optical power before the channel fell into the AWG target passband slot was actually lower than −40 dBm, however, the feedback value was truncated within the range from −40 to 0. As seen from Figure 3.17a, the target frequency is reached within ∼18 s. This tuning time was achieved regardless of the target channel and is due to fact that a pre-calibrated data of the ONU laser was used and the initial offset was always set to ∼ 400 GHz.

Operation phase

After the initial phase the operation phase was started and the fine tuning of the laser was done. Figure 3.18 shows the achieved wavelength accuracy of a long-term measurement over 15 hours. As the figure shows, the wavelength was kept within a ±3 GHz range during the whole time. The wavelength locker used in the experiment had a small polarisation dependence in one branch, resulting in a change of the measured ratio with polarisation, which was in turn compensated for by a wavelength change. It is expected that the PD effects can be reduced by using a different or optimized wavelength locker.

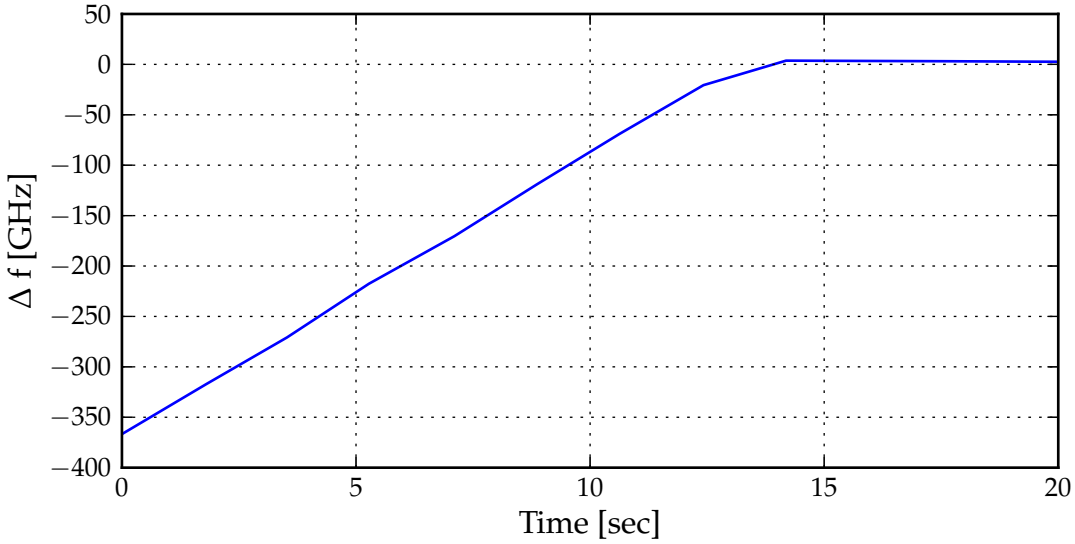

(a) Lasing frequency

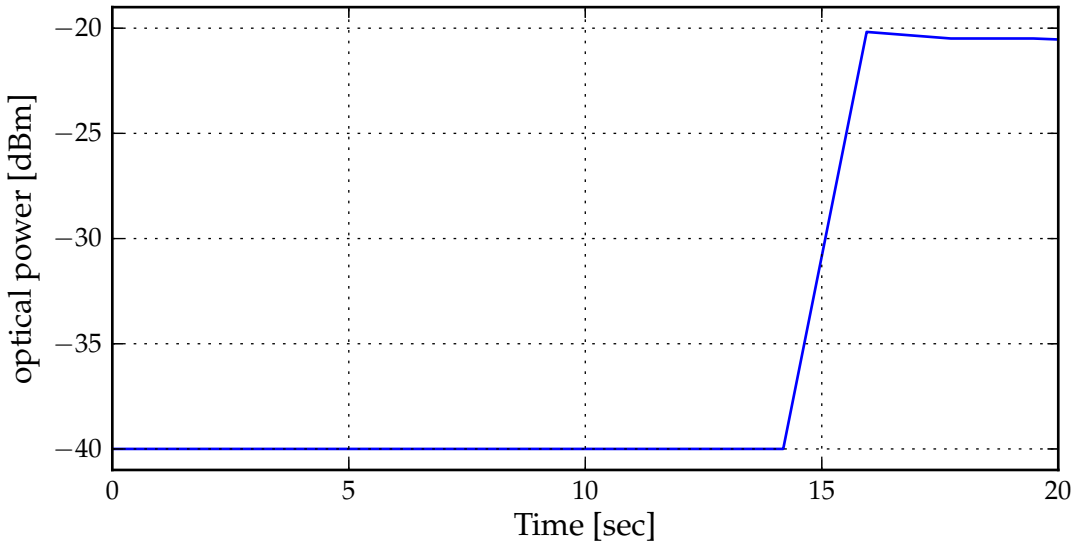

(b) Optical power

Figure 3.17: Measurement results during turn on process

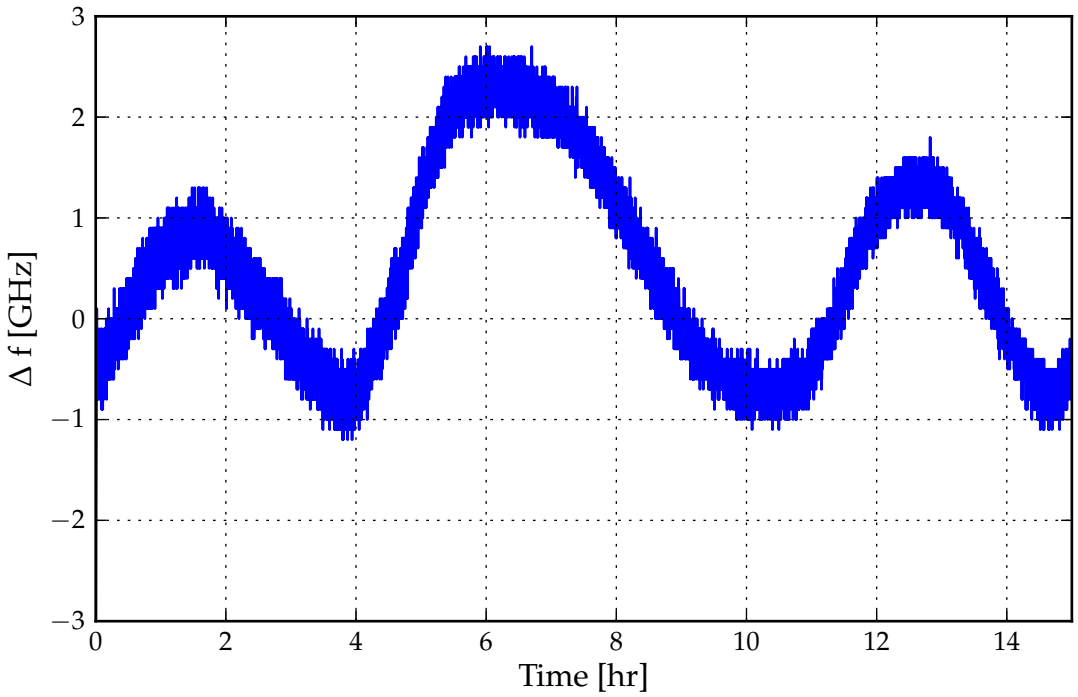

Figure 3.18: Long term frequency evolution at fixed laser temperature during the operation phase

3.7 Network wavelength control summary

In this chapter, first a standard tunable laser and its local wavelength control were described. Then, a network wavelength control was described which uses a centralised wavelength locker and individual pilot tones. This approach is very cost-effective as instead of N etalons for N ONUs, only 1 etalon at the OLT is needed. The OLT is estimating the optical power and pilot tone for each optical channel individually by measuring its pilot tone amplitude. This information is then transmitted to the ONUs via an ECC and evaluated at the ONUs within two phases: Initial phase and operation phase. During the initial phase, only the estimated optical power is considered until the level is high enough and thus the upstream channel is found. In the second phase, the operation phase, the ONU tries to minimize the wavelength error λ_{err}, which gives an information on the tuning direction.

The tuning principle was introduced in detail and also implemented. The experimental set-up was chosen to demonstrate the tuning of a full-band C-band tunable over a single fibre working set-up with 50 km SSMF. The experimental results showed that the target optical channel was found within $\sim$18 s independent of its position in the C-band. Additionally, a long-term experiment showed that by evaluation of the wavelength error λ_{err} a frequency stability of $\pm$3 GHz over several hours was achieved.

In the next chapter, optional approaches to lower the cost further are discussed: uncooled or partly uncooled tunable lasers with reduced or none calibration. This approach complements the centralized network control and allows the highest cost savings.

4 Tunable laser technologies

4.1 Chapter preface

Currently, several tunable laser technologies are commercially available and being used in tunable transceivers. For a complete overview on tunable laser technologies see [7], [73]. Common to all, here mentioned, tunable lasers is their tuning range over the entire C-band. Among these laser technologies, the following laser types could suit the requirements for PON usage:

- micro-electromechanical systems (MEMS)-tunable vertical-cavity surface-emitting laser (VCSEL) [74]
- multi-section distributed Bragg reflector (DBR) laser
  - digital supermode - distributed Bragg reflector (DS-DBR) laser [75]
  - sampled grating - distributed Bragg reflector (SG-DBR) laser [76]
- lasers with an external Bragg-Grating [77]
- sampled grating Y-branch (SG-Y) laser [78] .

In this chapter, the tuning principles of the DS-DBR and the SG-Y laser will be explained in detail. In the following, both concepts for lowering the cost will be evaluated experimentally for both laser types: reduction or omission of laser chip calibration and the operation without a TEC.

4.2 Operation principle

4.2.1 DS-DBR

The DS-DBR laser, commercially available from Oclaro Inc., is a fully monolithic integrated 5 section laser. The 5 sections are rear multi-peak reflector, phase section, multi-quantum well (MQW) gain, several Bragg front reflectors and a SOA. At both ends the

laser is anti-reflection coated. Figure 4.1a shows a schematic cross section of the laser, and Figure 4.1b shows a picture from the top of the laser chip itself. The wide tuning range

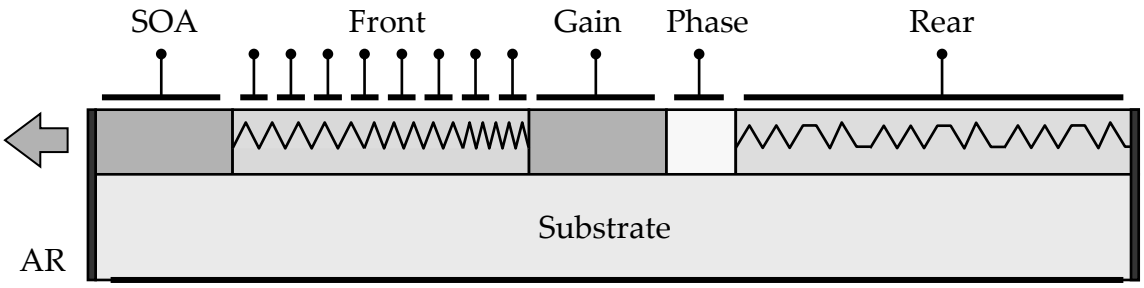

(a) Cross section - schematic view, based on [79]

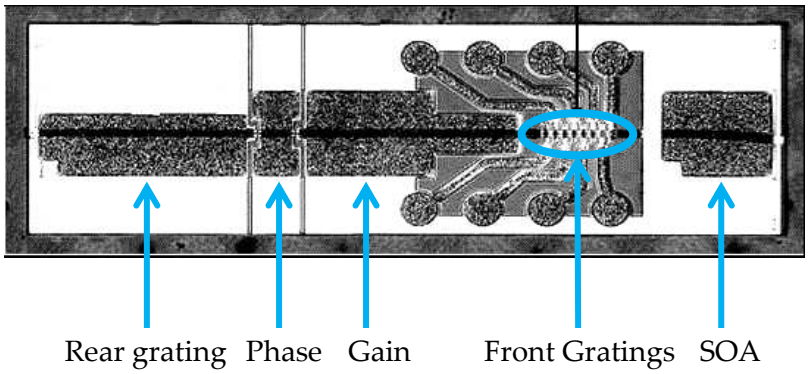

(b) Laser chip - top view, based on [80]

Figure 4.1: DS-DBR laser

of 1548 nm to 1563 nm, see [75], is achieved by a combination between the rear section and the selection of one front section. The rear section has a comb-shaped reflectivity spectrum with 7 main peaks. The injection current in one pair of 8 adjacent front grating contacts selects one of the 7 main peaks and suppresses all other peaks. Now the lasing frequency is within the selected sub-band of the front grating pair. Tuning within a sub-band can be achieved by aligning the rear grating and front grating.

Figure 4.2 shows the steps for selecting a lasing wavelength of ∼1 548 nm (∼ 193.664 THz). Starting point is the untuned state as shown in Figure 4.2a. In this state no front section pair is selected and the rear section is unaligned to the target lasing frequency. For selecting a lasing frequency, first, the matching front section for the target lasing frequency is selected by injecting a current into the corresponding front section pair, see Figure 4.2b. At this point the laser is lasing within the sub-band of the front section. The lasing frequency is marked by a triangle, and the sub-band is marked with a rectangle in the spectrum in Figure 4.2b. Finally, the injection current into the rear section is changed so that it also aligns with the front reflector at the target frequency, see Figure 4.2c

Additional to front and rear section, the phase and gain currents can be used to fine

tune the laser frequency within a small range. These two currents are mainly used to achieve high side-mode suppression ratio (SMSR) and to avoid mode jumps around operation points. Finally, the output power is equalized in the SOA section. For lower data rates, i.e. $< 10\,\text{Gbit/s}$, this section can be modulated directly, otherwise an external modulator, i.e. a MZM, has to be used.

4.2.2 SG-Y branch

Another tunable laser is the sampled grating Y-branch (SG-Y) laser. The SG-Y laser is also called modulated grating Y-branch (MG-Y) laser, see [81], [82]. The laser was originally developed by Syntune AB and is today commercially available from Finisar Corporation. The laser consists of the following sections: 2 reflector sections (branches) with different periods, multi-mode interferometer (MMI), phase section, gain section. Figure 4.3 shows the cross section of the laser.

The wide tuning range of the SG-Y laser is based on the Vernier effect between the two rear grating reflectors which each have a comb-shaped reflectivity spectrum. For selecting a specific lasing frequency both reflectors have to be tuned via their injection currents to align one of their peaks at the target frequency. As the rear reflectors have both a slightly different peak spacing, only the aligned combination of the peaks stimulates a mode and the other far-modes are suppressed. Figure 4.4 shows the schematic output spectrum of the tuning principle. The target frequency is marked with dotted circles. Figure 4.4a shows the alignment of one peak of reflector 1 with the target frequency. Reflector 2 is not aligned to the target frequency. Figure 4.4b then shows both reflectors aligned at the target frequency. This alignment produces a high power output and suppresses the other reflectors. Finally, the gain and phase section can be used to fine-tune the lasing frequency.

4.3 Laser calibration

As mentioned in section 3.4, the main cost driver for the tunable laser is not the laser chip itself, but rather the calibration step which takes a lot of time. The calibration step is very time consuming because all injection currents need to be calibrated for each optical channel at the operating temperature. The criteria for the calibration are, apart from the obvious lasing frequency, constant high output power, mode jump free tuning and high SMSR. For applications in the long haul area, a typical value for SMSR is $> 35\,\text{dB}$.

The result of the calibration step is the calibration table. The calibration table is sorted by optical channel and contains the values of all the injection currents. This laser chip

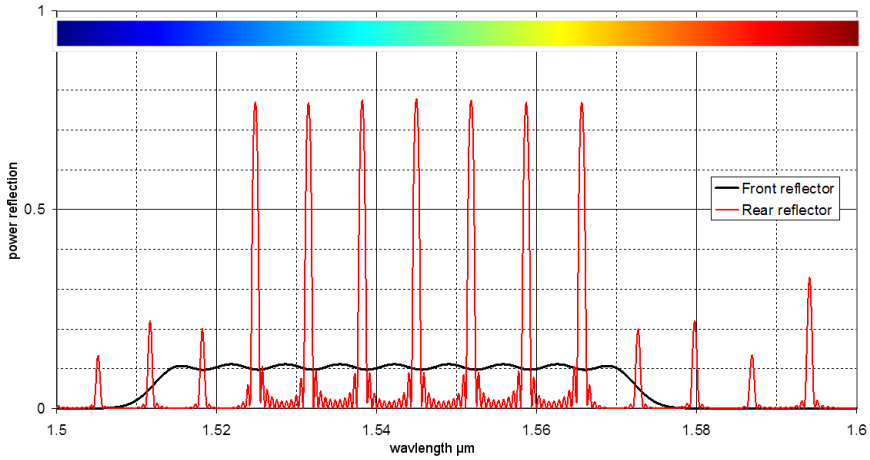

(a) No front pair selected - rear section unaligned

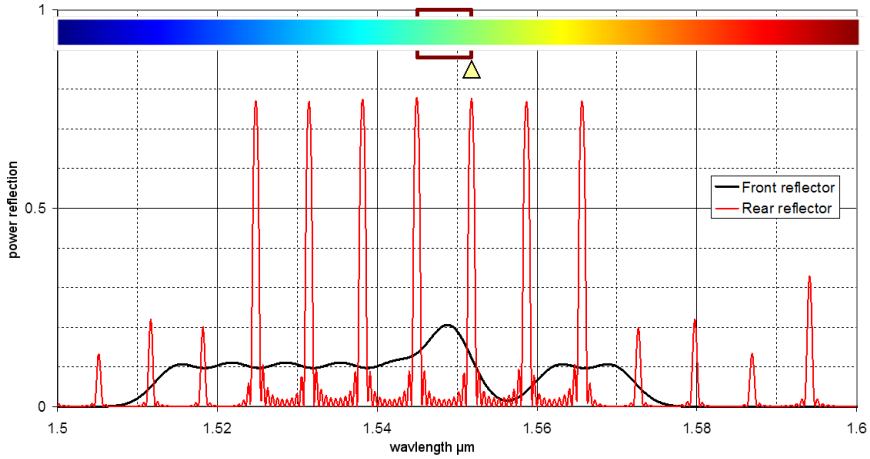

(b) Front pair selected and aligned - rear section unaligned

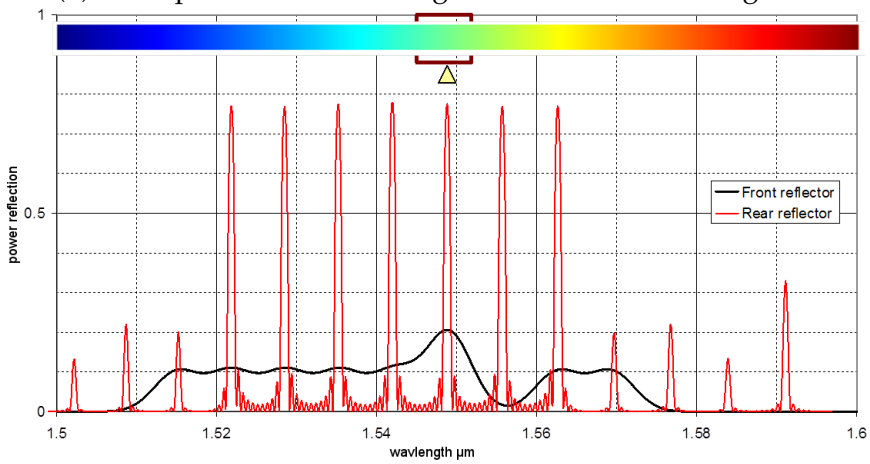

(c) Front pair selected and aligned - rear section aligned

Figure 4.2: Schematic tuning principle of the DS-DBR laser, taken from [79]

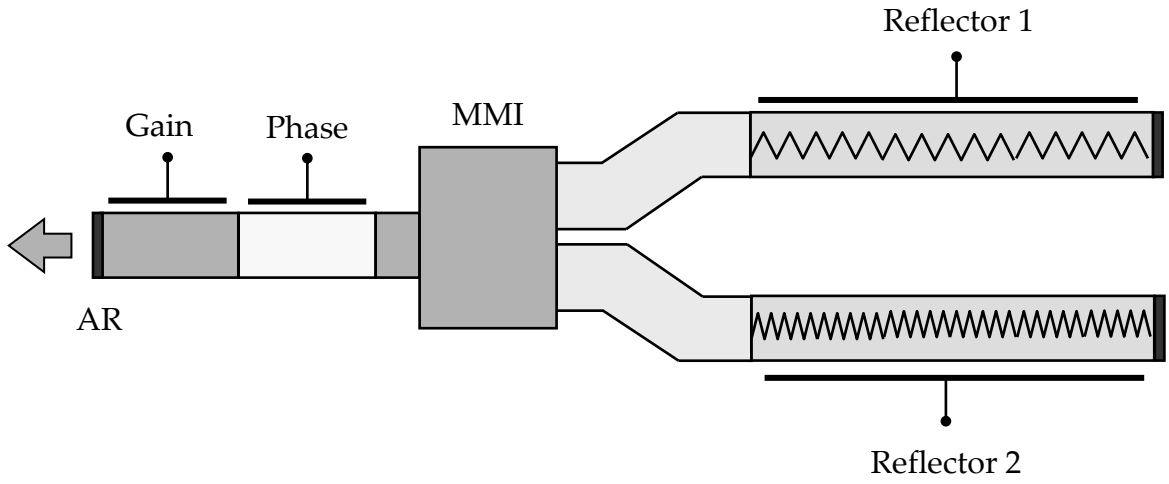

Figure 4.3: SG Y-branch cross section, based on [78]

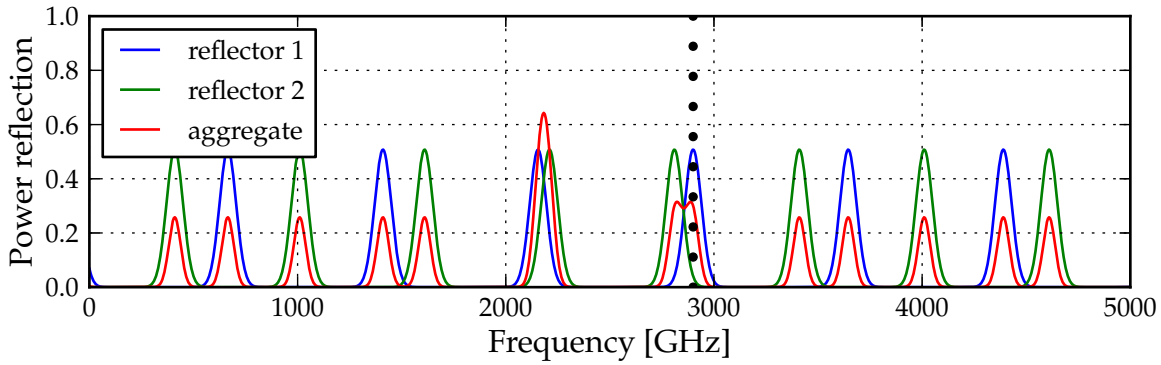

(a) Grating 1 tuned to target frequency & grating 2 untuned

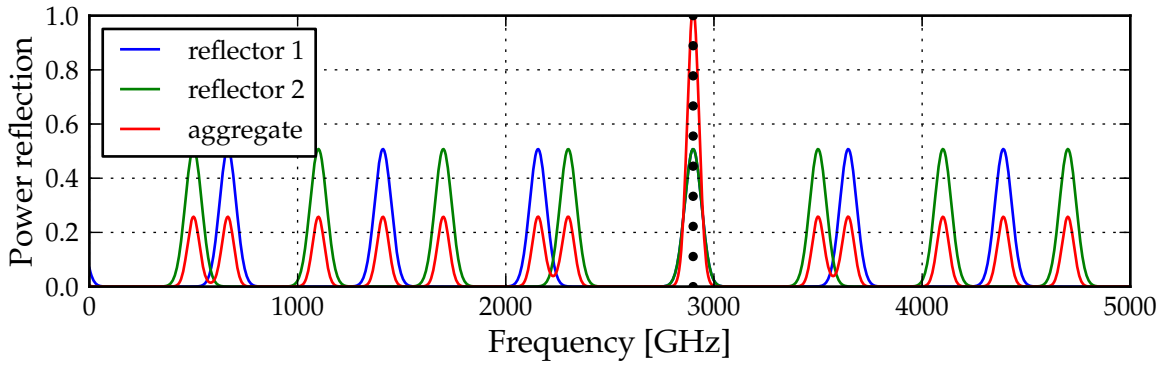

(b) Grating 1 & 2 tuned to target frequency

Figure 4.4: Tuning principle of SG-Y laser

specific calibration table is then saved in the microprocessor controlling the injection currents.

Apart from the long time to measure all optical channels also the calibration equipment is very expensive, e.g. optical spectrum analyser (OSA) and thus the process cannot be parallelised at low cost. In general, there are two possibilities to lower the effort: reducing or omitting the laser calibration.

4.3.1 Reducing calibration

In the reduced calibration approach, the calibration time is reduced by only measuring some key points in the laser tuning map instead of all optical channels. Then, the rest of the tuning map is interpolated. For this method, the reduction of the effort is dependent on the number of key points needed for a good interpolation. Section 4.7.5 describes one possible implementation for the SG-Y laser.

4.3.2 Omitting calibration

One step further is to omit the calibration step during manufacturing and therefore apply generic tuning functions. The application of generic tuning functions can lead to unsatisfactory performance as all laser chips differ somehow due to variations in production. This loss of performance can be (partly) compensated by a centralised wavelength control which provides a feedback signal for each ONU. The feedback signal can then be used to adjust the generic equations to yield better optical performance and also to improve the accuracy of the wavelength. This approach offers the highest saving potential but also the highest technical challenge to work properly. This approach will be discussed in Section 4.6.3 for the DS-DBR laser and in Section 4.7.4 for the SG-Y laser.

4.4 Athermal operation

Complimentary to the calibration free operation is the TEC-free operation to save power. Depending on the targeted environment, the temperature specification can be very challenging, e.g. $-40\,^{\circ}\mathrm{C}$ to $80\,^{\circ}\mathrm{C}$ for industrial range. Operating a laser without a thermoelectric cooler directly affects the lasing frequency of the laser. The external temperature change leads to a temperature change of the laser chip. This temperature change leads to a change of the refractive index of the material. The change of refractive index subsequently changes the lasing frequency of the laser. A typical value for this frequency drift is $\sim 12\,\mathrm{GHz}/^{\circ}\mathrm{C}$.

As the laser temperature increases, its threshold current increases and its slope efficiency decreases. Both effects decrease the laser output power. For lower temperature this can be compensated by increasing the injection currents. However, for higher temperatures ($> \sim$60 °C) the output power of the laser drops under a usable level. The problem of the power drop, however, can then only be solved with the usage of different materials, e.g. aluminium quaternary (AlQ), which have lower temperature dependent coefficient. The usage of a different material means a complete redesign of the laser. This is outside of the scope of this work and also results in high upfront cost for the new wafer masks.

It is thinkable to calibrate the laser at different temperatures to enable an athermal behaviour. The athermal calibration, however, increases the calibration time and thus the component cost. Instead of a temperature calibration step, the temperature introduced wavelength changes can also be compensated by using generic equations. The thermal generic equations are the same as the calibration-less generic equations. A temperature shift is translated to a wavelength shift and then the currents are changed accordingly. Section 4.6.3 discusses the thermal behaviour of the DS-DBR laser and Section 4.7.2 for the SG-Y laser.

4.5 General remarks on tunable lasers

4.5.1 Characterisation

The calibration effort can be omitted by using generic injection current equations instead. These generic equations can be extracted from a fully detailed characterisation and can be applied to different laser chips. Laser chips have small differences from chip to chip due to imperfect manufacturing techniques. Even though these differences exist the generic equations are still very similar and can be compensated via a network control loop. For the generation of the generic equation of the sub-band tuning a complete laser characterisation with all injection current combinations was done. Therefore all injection currents were swept in small steps and the output optical frequency and output power were monitored using a mlti-wavelength meter. The set-up is shown in Figure 4.5.

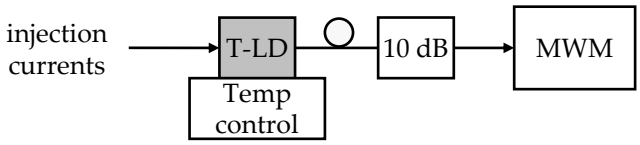

Figure 4.5: Experimental set-up for a tunable laser characterisation

4.5.2 Mode jumps

Thermal changes cause that different sections of the laser become mismatched and thus mode jumps will occur. A mode jump causes a short burst of error in the data transmission. In the residential access context, these error bursts can be regarded acceptable as the duration of the error burst is less than one Ethernet frame and will be auto corrected by the used higher layer (e.g. Layer-4 (TCP/IP) corrective actions). Additionally, it would be possible to stop the data transmission before a mode jump, which was triggered by a generic equation. While the mode jump occurs the data is cached in a memory and no data error is produced. After the mode jump, the data from the memory is transmitted as before the mode jump.

4.6 Digital Supermode-distributed Bragg reflector

4.6.1 Characterisation

The results of the characterisation for varying front and rear section currents are shown in Figure 4.6 and are called tuning-map. The figure shows the 7 front section settings, which are used to select one of the rear peaks. A particular combination is called a super-mode. The solid arrows mark the evolution of front and rear currents for a continuously increasing lasing frequency and was approximated by a generic equation. If the rear injection current reaches its maximum of $\sim$88 mA another super-mode has to be used to further increase the lasing frequency. This super-mode jump is marked in the figure by a dashed line. See Appendix B for a details on the generic equations of the DS-DBR.

4.6.2 Thermal behaviour

The same method of extracting equations from a full characterisation can also be used to get temperature-dependent equations. Contrary to the former general tuning map, the objective is not to use the equations for a continuously increasing the lasing frequency but for keeping the lasing frequency stable at different temperatures. Figure 4.7 shows the temperature tuning map for the phase section. This tuning map was generated with the set-up from Figure 4.5 and using the internal TEC to change the laser temperature. During the measurement, only the phase injection current was changed, all other injection currents where kept stable. The solid line in Figure 4.7 marks a constant lasing frequency for different temperatures. The approximation is the following two-degree polynomial for all three modes

$$I_{\text{phase}} = 0.179\vartheta^2 - 5.709\vartheta + 46.62 \tag{4.1}$$

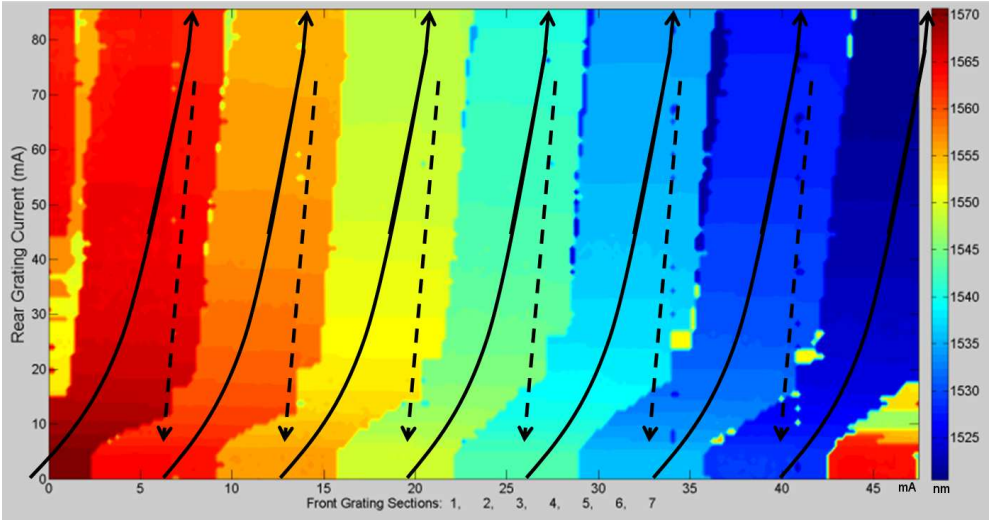

Figure 4.6: Output wavelengths at different front and rear currents at 25 °C; the x-axis is injection current [mA] into the front section selecting front pair 1 to 7

with I_{phase} being the phase injection current in mA and ϑ the temperature in °C. As seen within the range from 15 °C to 42 °C three cavity longitudinal mode jumps (dashed lines) occur. A mode jump is unwanted as it produces a burst of bit errors. The mode jump temperature range can be extended by parallel tuning of other sections. [83] demonstrated that, by parallel tuning of the gain section, the number of mode jumps within a temperature range from 15 °C to 70 °C can be reduced to two mode jumps for most channels.

Characterisation of the DS-DBR laser for different temperatures and also the extraction of mode-jump optimised injection current equations have been published in the author's paper [84] and in much more detail in [71], [80], [83]. It can be shown that by only using the generic equations the laser can be operated in an open loop control with acceptable results. [83] showed that a frequency stability of ±15 GHz can be achieved over a large temperature range.

4.6.3 Generic equations - experimental results

The experimental validation of the tuning algorithms was done with the former described centralised network control for WR-WDM-PON using a shared wavelength locker, as shown in Figure 3.8 and explained in Section 3.5.3. The ECC from the OLT to the ONU was not implemented as an optical in-data channel but rather an electrical Ethernet connection which is comparable to the final usage but easier to implement as it requires less hardware. The ECC only contained the four bytes for wavelength tuning as listed in Table 3.2. Further on, the pilot tone frequency and 1.25 GBit/s Ethernet data were

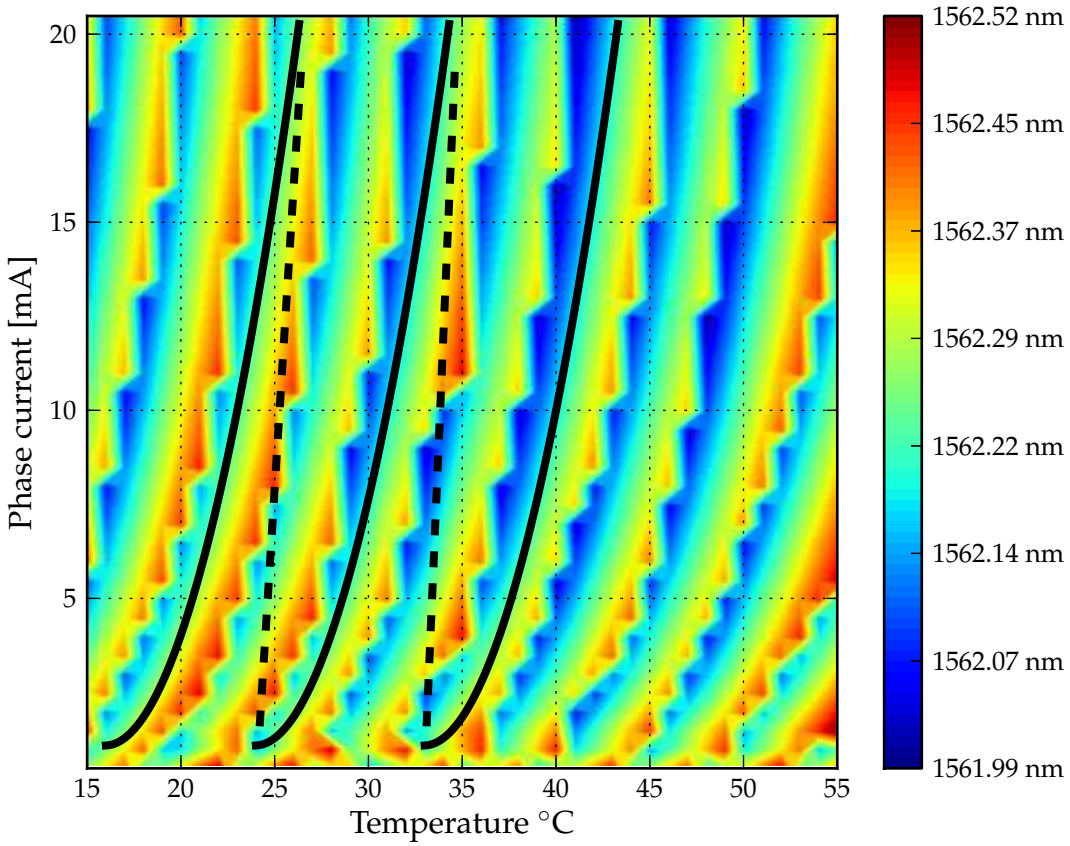

Figure 4.7: Temperature tuning map of the phase section

both applied to a MZM within the ONU. Figure 4.8 shows the complete experimental set-up for the ONU. For a realistic set-up a 40 km SSMF was installed between OLT and ONU. Note that in this experiment no TEC was used and the laser chip temperature was following the temperature in the laboratory.

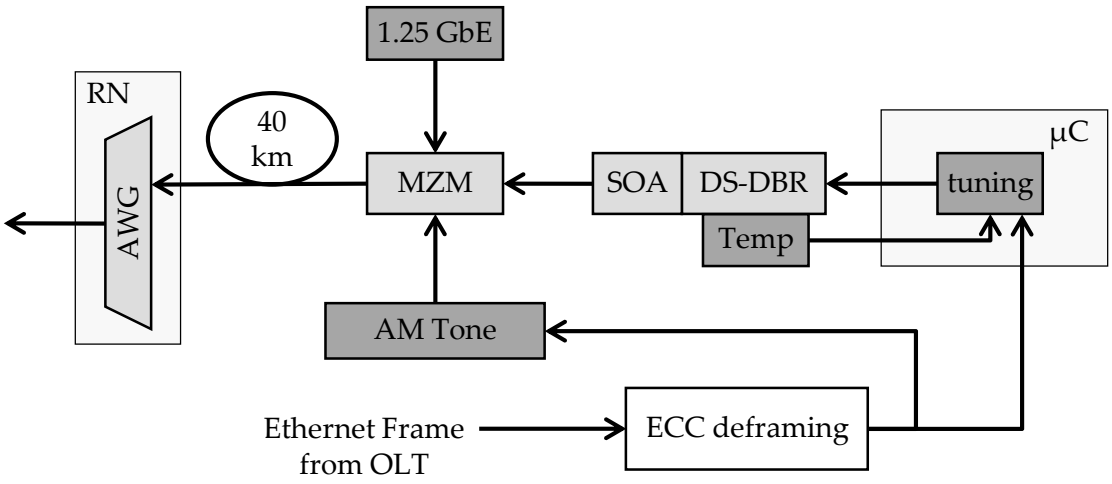

Figure 4.8: ONU sub-system diagram and control flow

Initial phase

After the turn-on of the laser and reception of the first ECC-frame the laser was tuned to the lowest optical channel. Then from the lowest channel the laser's frequency was increased step by step. The frequency increase was achieved by tuning the rear and the front sections in parallel. The values of the injection currents were calculated by using the extracted equations from Figure 4.6 and temperature-shifted ones. For covering the whole C-band the algorithm also needs to take care of super mode jumps. If the end of one super mode is reached, the injection currents for the next super-mode have to be set. It is however not possible, when using generic equations, to make a super mode jump maintaining the exact lasing frequency, if both super modes are not exactly calibrated and coordinated to interwork. A higher frequency in the next mode however contradicts the requirement to increase the frequency steadily. Therefore, a defined decrease in frequency for all the super mode jumps was implemented. This frequency overlap is also useful to provide some hysteresis for avoiding unnecessary mode jumps with changing temperatures.

During the initial tuning phase the gain current is fixed at 150 mA and the phase current was fixed at 0 mA. The step width of the lasing frequency has to be chosen so that it is ensured that the pass-band of the target WDM channel will always be found. In the experiment a step width $\sim$0.3 nm was used, which is about the accuracy of the tuning

map over a temperature range of 15 °C to 60 °C. This enables the laser to continuously increase the frequency even when the temperature changes and ensures that the lasers steps through the whole C-band and subsequently finds its target channel.

Figure 4.9 shows the measured results of the lasing frequency offset to the target frequency and the received optical power, both measured at the OLT. The tune-up time is dominated by the delay in the control loop. After each setting of new injection currents the ONU has to wait until it receives a new ECC-frame from the OLT. As seen from Figure 4.9, the initial tuning speed is roughly 2 THz/min and the selected target channel is found within 1 min. The entire C-band, which is used for upstream transmission, has a width of approximately 4 THz. Therefore, the initial tuning for all channels can be finished in less than 2 min. The main time factor in set-up was the processing of the pilot tones and the generation of the ECC-frames on the OLT side where a standard PC was used. It is expected that a speed-up of >10 can be achieved when using an FPGA.

After the target channel was found the optical power was maximised, and then the continuous phase was started.

Operation phase

In this phase, only the λ-error calculated from the etalon ratio was used to tune the laser, compare Table 3.1. In order to achieve a fine adjustment of the lasing frequency all sections where tuned using generic equations. With these equations and with the active feedback control a long term measurement was done. Figure 4.10 shows the measured result for the frequency offset and the λ-error. During all the time a frequency accuracy of $< \pm 4$ GHz is observed. During this test the laser chip temperature was left uncontrolled and changed arbitrarily between 28.5 °C and 33.2 °C. A bit error measurement with a standard Ethernet signal of 1.25 Gbit/s was done. The BER measured was $< 1 \times 10^{-9}$.

Finally, some error detection functions have also been implemented, e.g. monitoring the local output power to ensure that the injection currents are set properly. Another error detection function is to monitor the received optical power during this tuning phase. If the optical power is several ECC frames below a threshold, it can be assumed that for whatever reason (wrong injection currents, fast temperature change) the lasing frequency is no longer within the AWG passband. If this error is detected, a re-sweep within the neighbouring channels is done in order to find the correct optical channel again. In case that the optical power stays low and thus the AWG passband is not found, a complete restart of the tuning process with the initial phase is done.

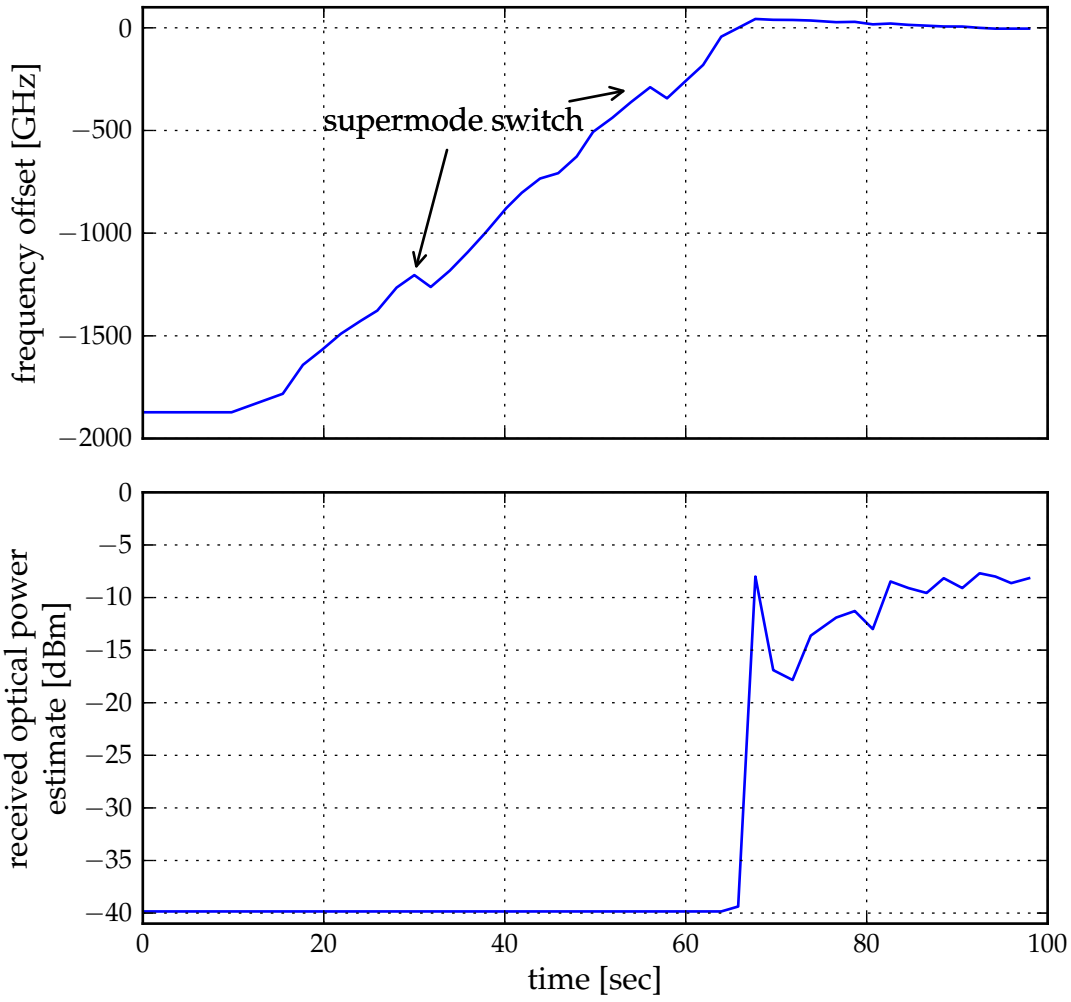

Figure 4.9: Initial wavelength search after power-up of the ONU

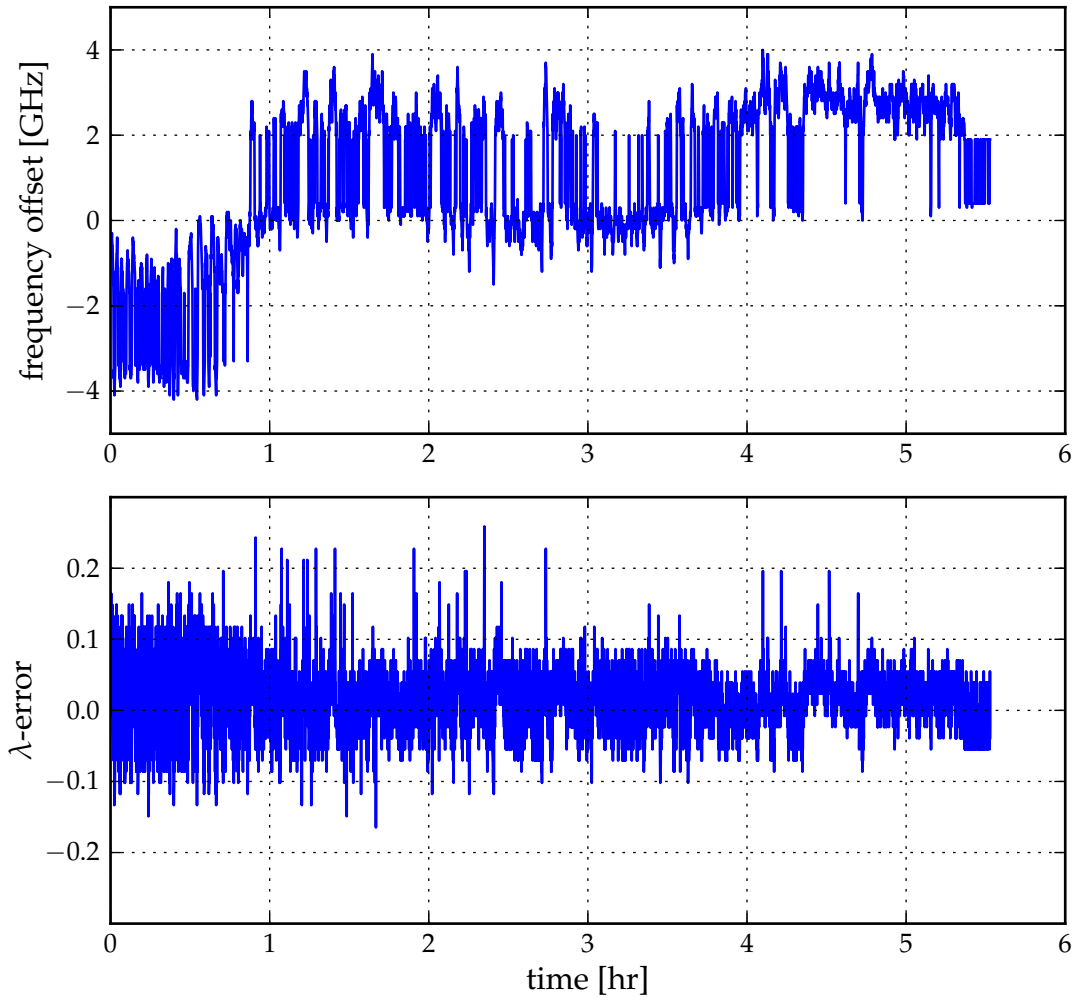

Figure 4.10: Long-term frequency stability

4.7 Sampled grating Y-branch laser

4.7.1 Characterisation

Similar to the DS-DBR laser, the SG-Y laser can be characterised by a tuning map. At a fixed temperature, both the injection currents to the reflectors were independently increased from 0 mA to their maximal allowed value. The maximal value of $\sim$20 mA was set so that the gratings are not damaged. The set-up used to generate the tuning map was the same as shown in Figure 4.5. Figure 4.11 shows the generated tuning map of the SG Y-branch laser. The regions of the same colour represent one super-mode. A super-mode can be defined as the frequency range where the same combination of rear reflector peaks is used. In the total spectrum, from blue to red, 8 super-modes are seen. The lower right and upper left areas are repetitions and don't allow stable operation. The white spots in Figure 4.11 are combinations of injections currents where the measured output power was $>$ 10 dB lower than the normally observed 13 dBm, which normally appear at the transition between two super modes. At the transition between two super modes, the available power is shared between the modes as the laser shows a multi mode behaviour. Furthermore, it can be seen that the SG Y-branch laser covers the entire C-band.

4.7.2 Thermal behaviour

As mentioned before, the lasing wavelength changes with the environment temperature. In order to quantize the wavelength shift, the wavelength was measured, again using the same set-up as shown in Figure 4.5. The injection currents to all sections were kept constant and only the TEC set point of the laser was changed. Figure 4.12 shows the measured lasing frequency shift of a SG Y-branch laser with static injection currents over changing temperature. As seen from the figure at $\sim$33.6 °C a mode jump to the next longitudinal mode occurs. Additionally, the temperature coefficient mentioned in Section 4.4 of $\sim$12 GHz/°C can be observed.

4.7.3 Athermal operation with generic equations

Again, the basic idea of the athermal operation is to counteract any wavelength shift introduced by a temperature change by adapting the injection currents, see the author's publication [85]. Therefore, the frequency change of the rear combs as a function of the injection currents was measured. The red curve in Figure 4.13 shows the lasing frequency as a function of the injection current into one rear reflector. As a generic equation, the measurement curve was approximated by a square root function (blue curve) with the

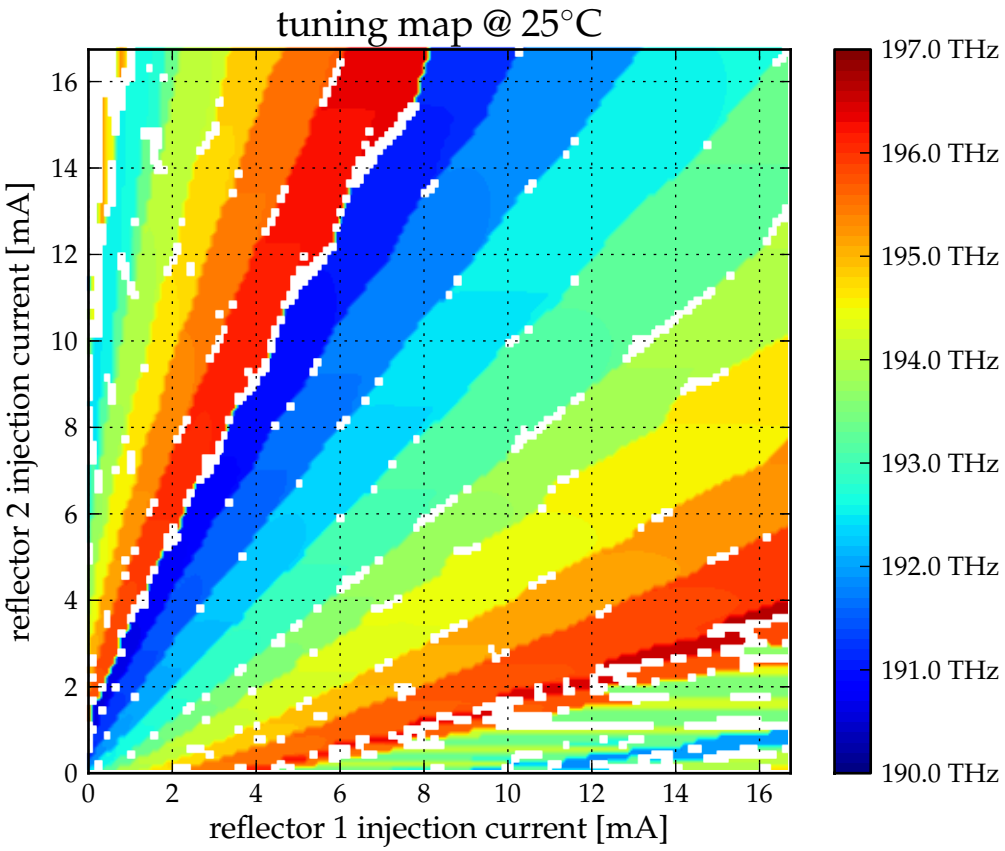

Figure 4.11: Tuning Map of a SG Y-branch laser, white spots are combinations with low output power

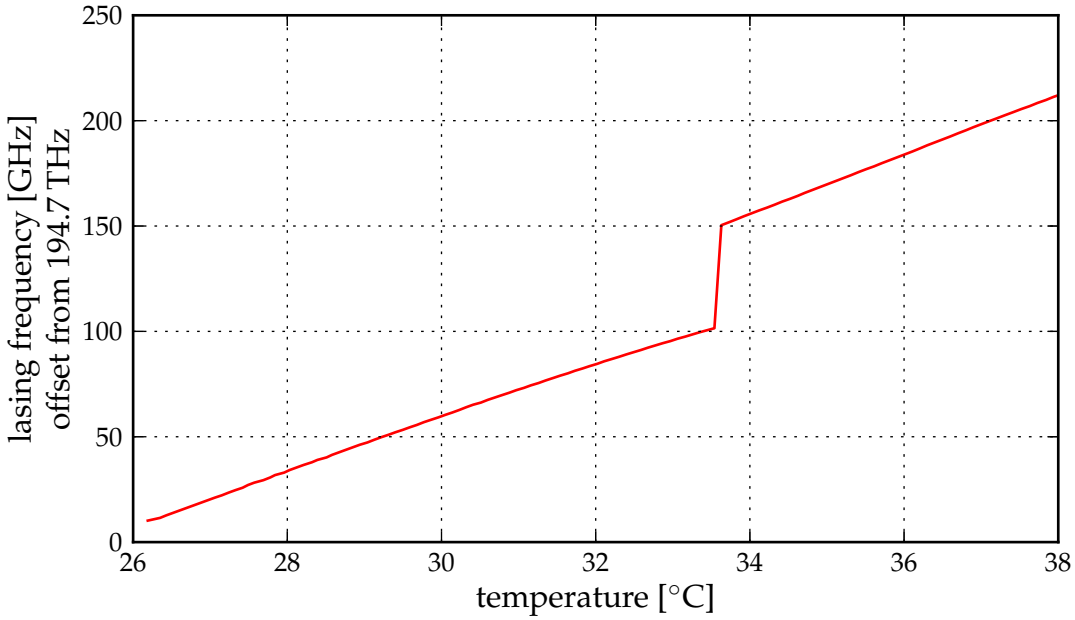

Figure 4.12: Temperature drift with fixed injection currents, at a temperature of ∼33.6 °C a mode jump to the next cavity longitudinal mode occurs

following parameters:

$$\Delta f = \sqrt{46519.21}\sqrt{I_{\text{rear}}}. \tag{4.2}$$

When operating within one super-mode (combination of the same two reflectance peaks of the rear grating), the frequency can be tuned continuously by tuning the two reflectors simultaneously from a given lasing position until a longitudinal mode jump occurs. The mode jump is a phase mismatch which occurs between the sections. Therefore, it is possible to simultaneously tune the phase section so that ideally the effect of the wavelength jumps is fully compensated. However, perfect compensation cannot be achieved for all longitudinal mode jumps. Figure 4.14 shows an exemplary measurement of the longitudinal mode jump compensation using a linear decreasing phase injection current. The upper subfigure of Figure 4.14 shows the resulting lasing frequency with two mode jumps. The first jump has a phase mismatch of ∼6 GHz and the second ∼9 GHz, which leads to acceptable jumps compared to the 50 GHz as seen in Figure 4.12.

This parallel shifting method can be used until one injection current needs to be set to a value outside of the boundaries of the approximation (0 mA to 18 mA). If this occurs, a new super mode has to be found and used. A possible solution is to use generic equations based on the full-band tuning map. However, by using the discussed method a temperature change > 10 °C can be compensated.

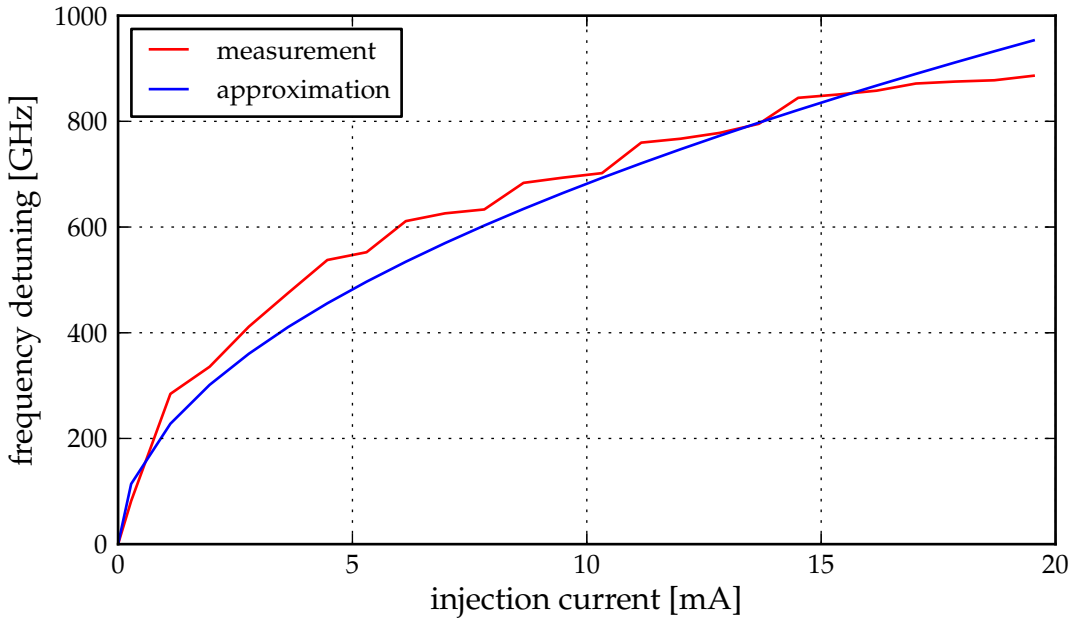

Figure 4.13: Wavelength shift over injection current; the approximation with a square root function

4.7.4 Generic equations - experimental results

Again, for experimental demonstration of the tuning concept the same setup as shown in Figure 3.8 was used, which represents the basic WDM-PON set-up. For reducing the hardware effort, the loop-back from the OLT to the ONU was omitted and done locally by the control PC. However, exactly the same could be done via a real loop-back as described in Section 3.5. Again, both the received optical power (OP-RX) and wavelength error (λ-error) were used to control the ONU wavelengths. The experiment is again split up into the two phases.

Initial phase

First, after the turn-on of the laser, a sweep over the entire C-band is started. This sweep was achieved by doing a blind search in all possible combinations of the two reflector sections. Basically, Figure 4.11 is searched for the current combination for the target wavelength, determined by a transparent path between ONU and OLT. This blind search could be accelerated, if the knowledge of the target channel wavelength was taken into account. This however was not implemented. The blind search is done until the received optical power at the OLT raises, which signifies that the target channel is reached. The whole tuning process for the initial phase takes $\sim$55 s, which is however only limited

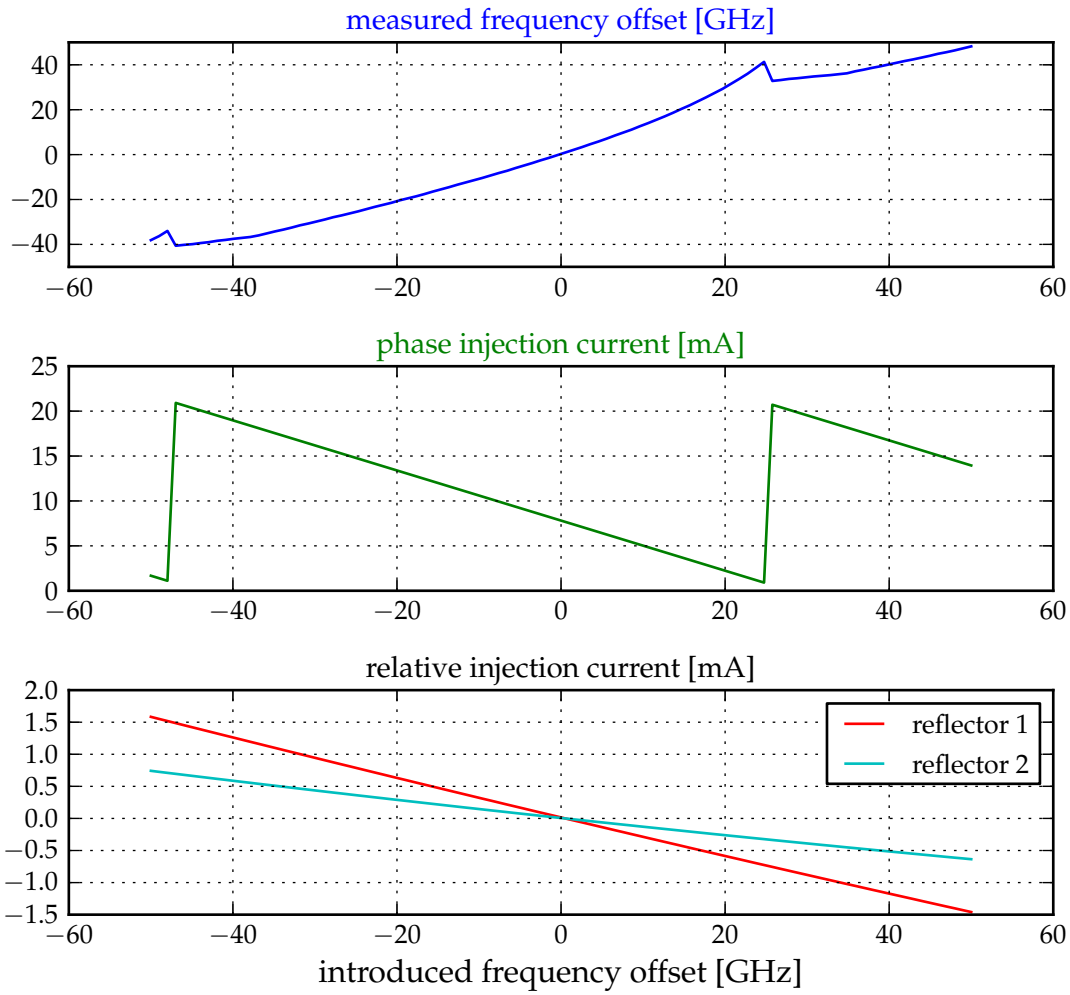

Figure 4.14: Longitudinal mode jump compensation by parallel tuning of the phase section and both reflectors

by the speed that the control board is capable of changing the injection currents. With a specially designed control board a factor 10 in speed-up can be expected.

Continuous phase

In the second phase, after the initial tuning the temperature of the laser chip was changed slowly. This was done by changing the TEC set-point of the module and has the same effect as a changing environmental temperature. The temperature was changed from 26 °C to 38 °C within 15 minutes. This corresponds to a temperature change rate of $\sim$0.8 °C/min. Even higher temperatures can only be achieved by disabling the TEC and applying external temperature control to the module (i.e. temperature chamber). The temperature change rate was limited by two factors: As mentioned before the speed of driver electronics and also the monitoring of the result parameter. Especially the multi-wavelength meter, which is measuring the frequency offset from the channel nominal value, takes $\sim$2 s to complete one measurement.

Results

Figure 4.15a shows that after the first $\sim$10 s of initial tuning using the feedback loop the wavelength can always be kept within $\pm$5 GHz of the target wavelength. Additionally, Figure 4.15b shows the received optical power and the ratio of the pilot tone at the wavelength locker. This value is normalized, meaning that a ratio of 1.0 represents the target wavelength. As it can be seen from Figure 4.15b two drops of the power are observed (at 180 s and 560 s). These two drops are the former mentioned longitudinal mode jumps. In the first event (180 s), the mode jump could be compensated directly after it occurred and thus the slower wavelength measurement did not capture the event. In the second event (560 s), the correction takes longer and is accordingly captured by the wavelength measurement. The experiment has been repeated with similar results for different channels over the C-band, and the jump offset was normally $< \pm$10 GHz and the target wavelength re-locked within $<$ 5 s after the mode jump.

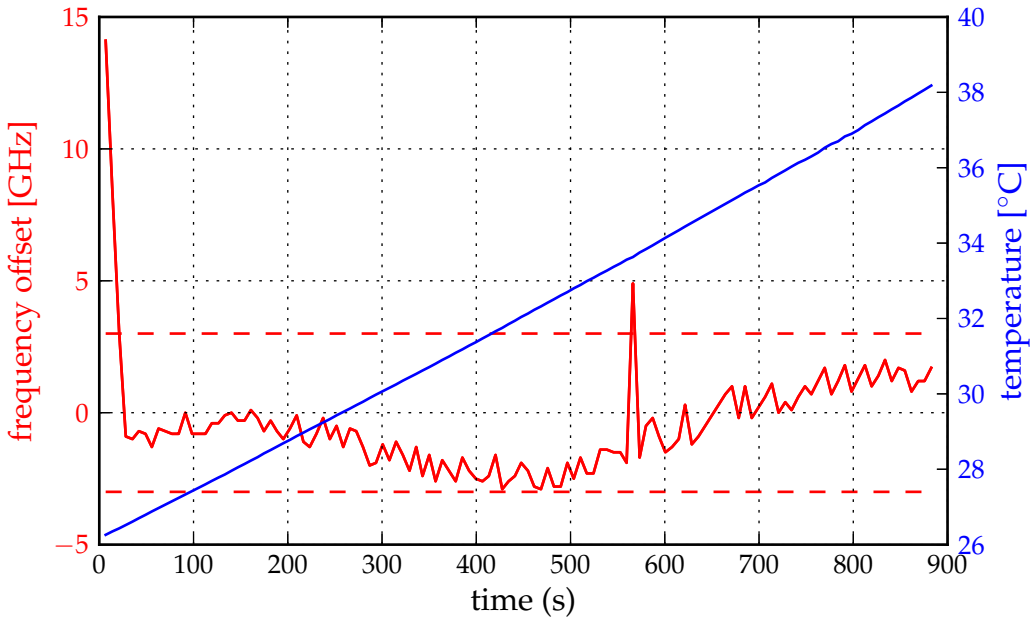

(a) Frequency and temperature

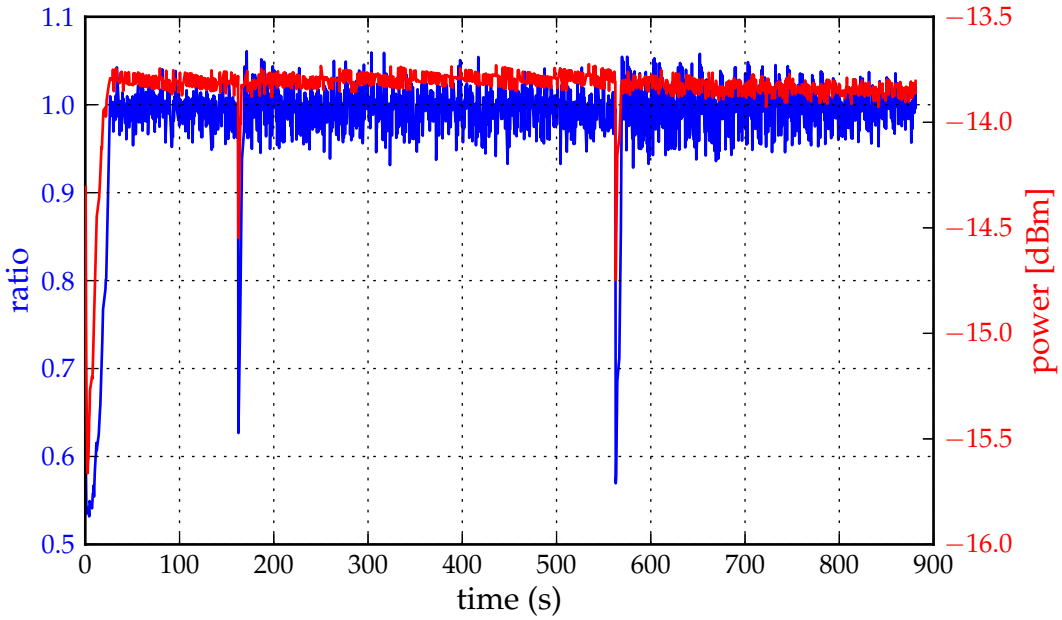

(b) Optical power at the OLT RX and ratio at the wavelength locker; a ratio of 1.0 is the target ratio

Figure 4.15: Result of the tuning using generic equations

4.7.5 Athermal operation with interpolated calibration data

In order to achieve single-mode behaviour and a high SMSR, the commercially available laser is characterized around each alignment of two reflectivity peaks which are approximately 50 GHz apart. This characterization is done using three values: two rear reflector currents and a phase injection current under a stable temperature of 25.0 °C. High SMSR is normally achieved around ±20 GHz of a peak combination.

Differently to the former explained variant of generic injection current equations, it is possible to interpolate this calibration data and to use it to counteract thermal changes. This approach was applied to rear and phase sections. To facilitate the operation of the laser and to reduce the number of calibration points needed for characterization, the curves were approximated. For the rear reflectors linear equations $\Delta f = a_r I_{\text{rear}} + b_r$ and for the phase section a quadratic equation $\Delta f = a_p I_{\text{rear}}^2 + b_p I_{\text{rear}} + c_p$ was used. The parameters were different for each alignment. In order to achieve continuous frequency tuning, the approximations have been extended so that overlapping frequency sections exist between two adjacent alignments. Figure 4.16 shows the resulting wavelength tuning versus the frequency set-point for different temperatures. It demonstrates that the lasing frequency can be kept constant by modifying the set-point, when the temperature evolves.

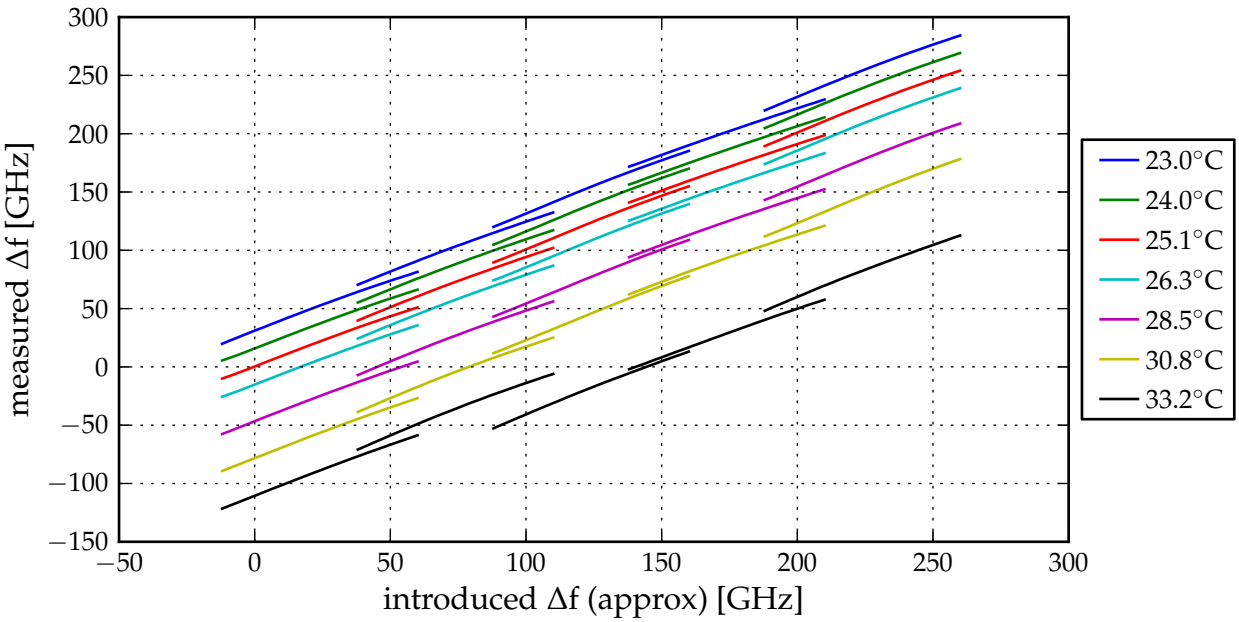

Figure 4.16: Lasing frequency of the laser for different temperatures using the interpolated equations. Each continuous line is a single alignment (mode)

The approximation was then used to operate the laser within changing environment

temperatures. A temperature change results in the change of the refractive index of the waveguide, which is proportional to the change in emission frequency. With increasing temperature, the laser frequency is shifted towards lower frequencies, which are compensated by lower injection currents within the limits of a single alignment. Upon further temperature increase, another alignment has to be used and therefore a mode-jump will occur. An advantage of this method is that the required time to reach the target channel is reduced as its injection current values can be calculated using the interpolation curves.

4.7.6 Interpolated calibration data - Experimental results

Again, the experiments were performed within a WR-WDM-PON with a network wavelength control including the initial and the operation phase. In all configurations, the same control loops on ONU and OLT were used. Between OLT and ONU a 50 km SSMF was installed to emulate realistic transmission distances. Figure 4.17 shows the complete optical set-up. On the OLT-side a standard PC was used to calculate the ECC data, and then an FPGA was used to generate the ECC frames. On the ONU-side, the ECC was received with an FPGA board and transmitted to a PC, which controlled the integrated tunable laser assembly (iTLA) including the laser and the TEC.

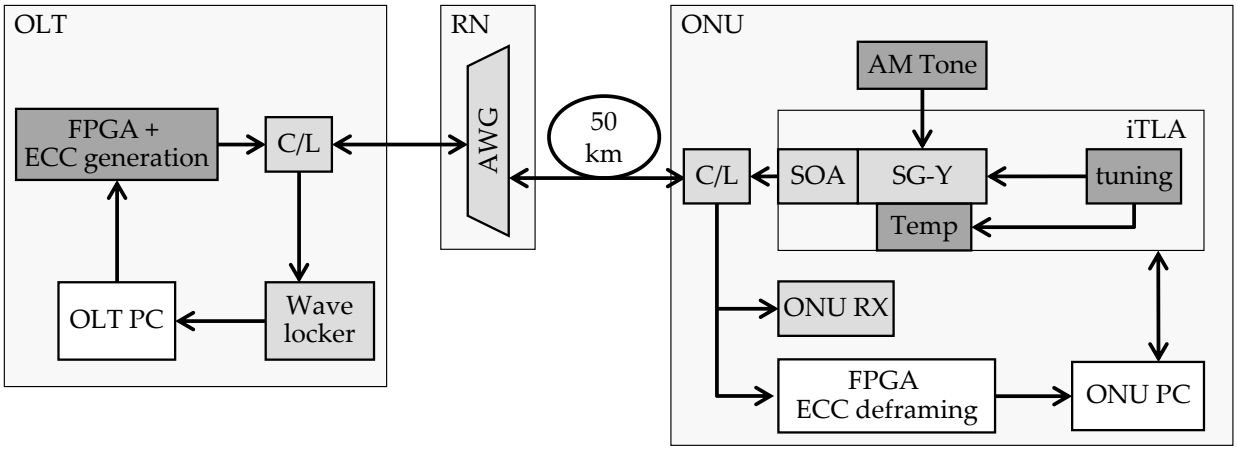

Figure 4.17: Test set-up for the SG-Y laser testing

Initial phase

After turn-on, the ONU waits for the first reception of the downstream ECC-frame. As the frame contains the target optical channel and the upstream pilot tone frequency, it is possible for the ONU to initialize its settings accordingly, compare also Section 3.5.3. The generation of the pilot tone was done with an external function generator and was adjusted manually, however in a fully integrated system this step will be done

automatically. Then the injection currents for a mode, which is $\sim 400\,\mathrm{GHz}$ lower than the target channel, were selected. From this point onward, the injection currents were changed so that the frequency was increased until the received optical power at the head end was higher than a pre-set level. At this point, the lasing frequency lies within the pass-band of the RN's AWG, which has a 3-dB bandwidth of $\sim 60\,\mathrm{GHz}$. The turn-up process is the same measurement as already described in Section 3.6. Figure 3.17 shows the transmit wavelength evolution during this tuning phase. As the lasing frequency now lies within the lock-in range of the wavelength locker, it is possible for the ONU to evaluate the values of the frequency up-or-down information received in the ECC-frame. During the continuous tuning process, only this information is used to tune the laser until the received optical power drops under a pre-set value and the start-up cycle is repeated.

Operation phase

For the operation phase two measurements were done: With stable and changing temperature. The results with stable temperature were already described in Section 3.6. It was shown that the wavelength was kept within a range of $\pm 3\,\mathrm{GHz}$.

In a second experiment, the laser temperature was randomly varied between 20.0 °C and 30.0 °C, see Figure 4.18, upper part. Here, the lasing frequency is kept within $\pm 5\,\mathrm{GHz}$ of the target. The peaks in Figure 4.18, lower part, are due to mode jumps, which occur when a new pair of injection currents is chosen. Directly after any mode jump, the $\pm 3\,\mathrm{GHz}$ range was reached and kept until the next mode jump became necessary.

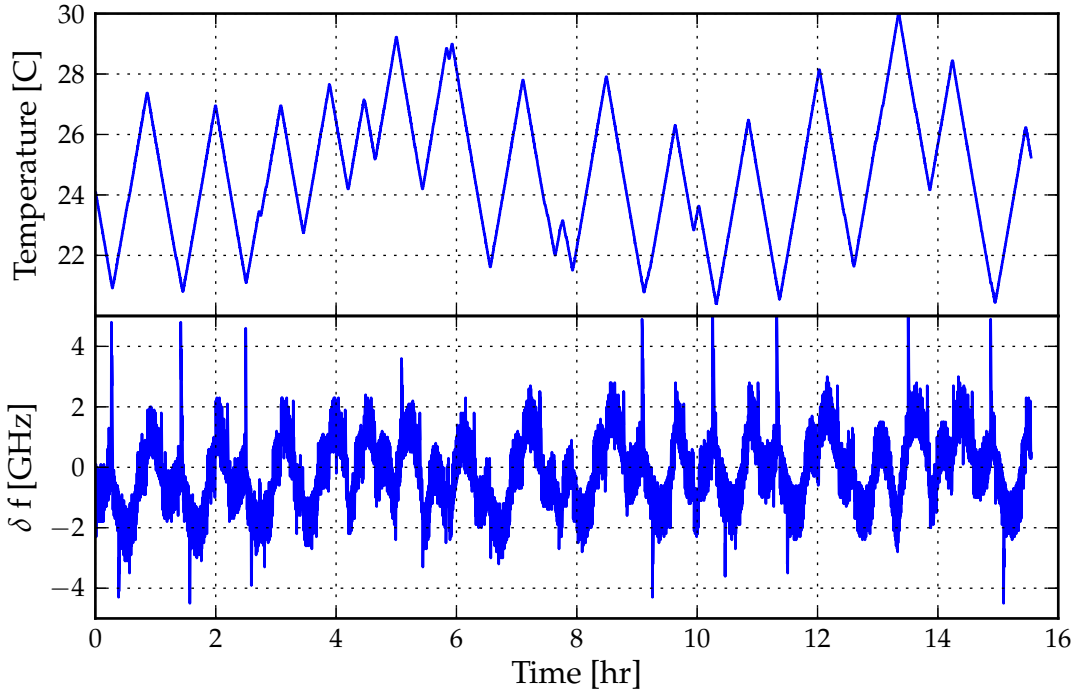

Figure 4.18: Long term frequency evolution with varying temperature

4.8 Low cost tunable lasers - summary

In this chapter it was was reported, how uncooled (or at least partly uncooled) DS-DBR and SG-Y lasers in ONUs can be wavelength-stabilized in a WR-WDM-PON system context against ambient temperature drift. This is achieved by a combination of measuring the laser chip temperature and using the wavelength tuning information provided by the OLT. With these two process variables the injection currents can be changed in order to maintain the wavelength. Two approaches for the setting of the injection currents were presented: using generic equations and the interpolation of calibration data. Both concepts have been demonstrated successfully in conjunction with the network wavelength control, which was presented in Chapter 3.

Whilst the usage of generic equations does not require any per device calibration, its performance is not as good as the interpolation concept. Both variants are aware of mode jumps, and it has also been shown how mode jumps can be controlled and resulting effects be minimised.

As proven, the combination of the network wavelength control together with the tuning concepts for TEC-less and calibration-free laser modules allows to build low-cost ONU transceivers.

5 Grid-less wavelength locking

5.1 Motivation

In a WR-WDM-PON a RN is used to separate upstream and downstream wavelengths in different bands. As seen from Table 1.2, only the channel spacing in C-band is equal to a ITU standard 100 GHz grid. Other bands have a slightly higher or lower channel spacing. If an etalon for the usage in another band is needed, it becomes necessary to design an etalon with a FSR matching this channel spacing. An etalon to lock the channels L-band, for an AWG as measured in Table 1.2, would then need to have an FSR of 97.3 GHz.

Other applications, like flexible grids (FlexGrid), no longer use fixed channel spacings or use very small spacings. This is done for better bandwidth utilisation of the optical spectrum. [86] defines channels with either 12.5 GHz, 25 GHz, 50 GHz, or 100 GHz optical width. For a gapless operation the channel center frequencies then need to have a granularity of 6.25 GHz.

An etalon, designed for such a FlexGrid transceiver, would need to have an FSR of 6.25 GHz. This FSR leads to a symmetrical lock-in range of only 3.125 GHz. Such a small lock-in range is practically unusable with inaccurately characterized lasers, if not unusable at all.

In the following, a method incorporating a second etalon will be presented. The new method is capable of locking a laser to an arbitrary frequency while maintaining the symmetrical lock-in range of $\frac{1}{2}FSR$ of the etalons.

5.2 Simple combination of two etalons

As described in Section 3.3.2, every etalon has a certain symmetric lock-in range which is depending on the FSR. As seen from Equation (3.16) and Figure 3.7, the lock-in range is only maximal at 2 points, which are at $\frac{1}{4}FSR$ and $\frac{3}{4}FSR$. Their absolute positions dependent on the absolute frequency offset.

The basic idea, see also [87], is to add a second etalon with another offset, which is used when the first etalon has a small lock-in range. For the ease of use the second

etalon has the same parameters as the first one. Only its frequency is shifted by $\frac{1}{4}FSR$ or $\frac{3}{4}FSR$ so that it has its maximal symmetrical lock-in range where the first etalon has its minimum. Figure 5.1 shows the lock-in ranges for 2 etalons on a 100 GHz channel grid and a frequency offset of 25 GHz between the etalons. Now, at the frequency of 25 GHz only the ratio from etalon 1 is evaluated and at 50 GHz only the ratio from etalon 2. This simple method results in a minimal overall symmetrical lock-in range of $\frac{1}{4}FSR$, here 25 GHz.

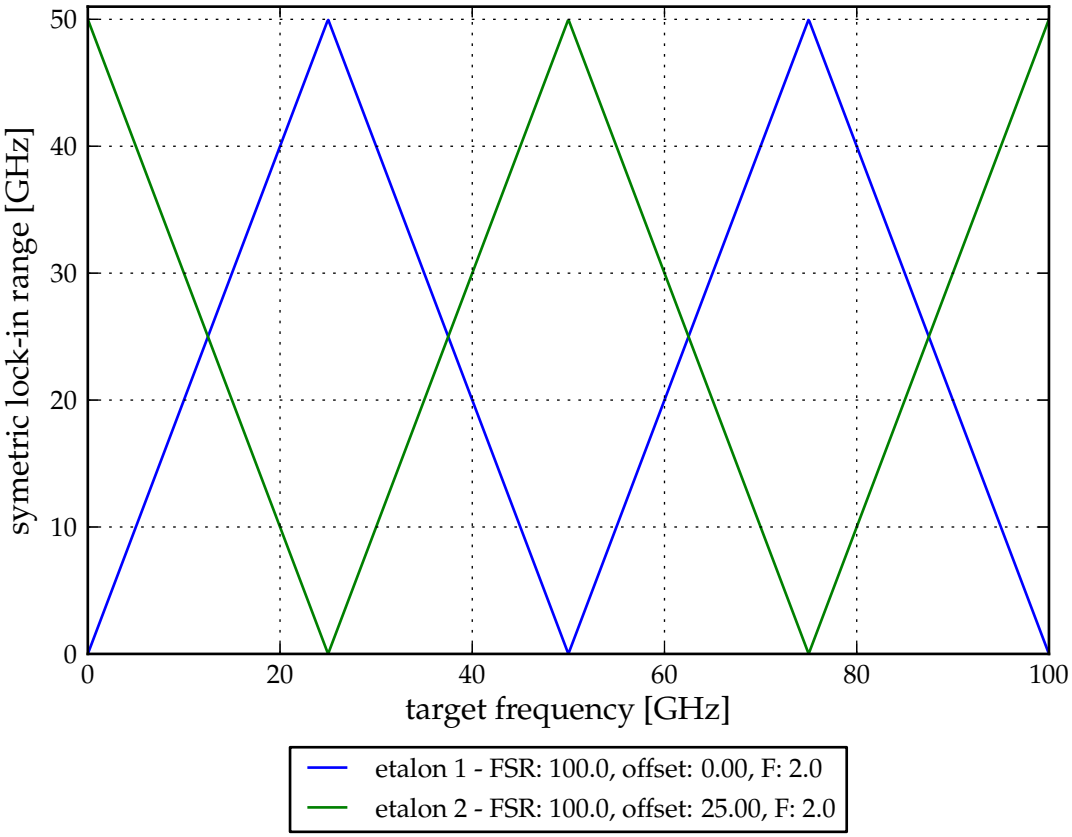

Figure 5.1: Lock-in range of two etalons

5.3 Weighting of two etalons

5.3.1 Theory

Additional lock-in range can be gained by applying a weighting function to both etalon transfer functions. The etalon transfer function was already defined in Equation (3.10).

Here, a slightly modified definition will be used

$$T_{i,\Delta}(f) = \frac{1}{1 + F \sin^2\left(\frac{\pi}{FSR}(f - \Delta)\right)}. \tag{5.1}$$

where i is the number of the etalon and Δ the frequency offset. E.g., $T_{1,FSR/2}$ is the transfer function of etalon 1 shifted by $\frac{1}{2}FSR$. Using this definition a combined transfer function $T_c(f)$ can be calculated

$$T_c(f) = a_1(f)T_{1,\Delta 1}(f) + a_2(f)T_{2,\Delta 2}(f) \tag{5.2}$$

with $\Delta 1$ and $\Delta 2$ being the frequency offsets of the two etalons. The values of the weighting factors $a_1(f)$ and $a_2(f)$ are calculated, so that $T_c(f)$ will get periodic with $\frac{FSR}{2}$ and thus have a maximal symmetrical lock-in range of $\frac{FSR}{2}$ over all target frequencies.

$$T_c(f) \stackrel{!}{=} T_c\left(f + \frac{1}{2}FSR\right) \tag{5.3}$$

With the assumption that both etalons have the same FSR, $T_c(f)$ of Equation (5.3) can be simplified to

$$a_1(f)T_{1,0}(f) + a_2(f)T_{2,0}(f) = a_1(f)T_{1,FSR/2}(f) + a_2(f)T_{2,FSR/2}(f). \tag{5.4}$$

Solving the equation for $a_1(f)$ leads to

$$a_1(f) = a_2(f) \underbrace{\frac{T_{2,FSR/2}(f) - T_{2,0}(f)}{T_{1,0}(f) - T_{1,FSR/2}(f)}}_{Z(f)} \tag{5.5}$$

$$a_1(f) = a_2(f)Z(f). \tag{5.6}$$

where $Z(f)$ is an auxiliary variable. Note that $Z(f)$ only depends on the following design parameters of the etalons: finesse F, FSR and the frequency offset between the etalons $\Delta_{1,2}$.

Assuming that the etalons have the same FSR, at the lock-in point with the maximal lock-in range of etalon 1, etalon 2 can be weighted with 0 as it cannot enlarge the overall lock-in range. At this point the etalon 1 can be weighted with 1. The same condition is also true for the maximal lock-in range point of etalon 2. This can be generalised to yield a condition for all frequencies:

$$a_1(f) + a_2(f) = 1. \tag{5.7}$$

Applying this condition, the weighting factors can be calculated to

$$a_1(f) = \frac{Z(f)}{1+Z(f)} \quad \text{and} \quad a_2(f) = \frac{1}{1+Z(f)} \tag{5.8}$$

and thus the combined transfer function $T_c(f)$ results in

$$T_c(f) = \frac{1}{1+Z(f)} \left(Z(f)T_1(f) + T_2(f)\right). \tag{5.9}$$

Given that the two etalon transfer functions don't have their maxima at the same point, and that both etalons have the same FSR, $Z(f)$ and thus also $T_c(f)$ are periodic with FSR. This means that for any frequency difference, $T_c(f)$ has a symmetrical lock-in range of $\frac{1}{2}FSR$ for all target frequencies.

5.3.2 Numerical evaluation

In order to compare the weighting method to the simple combination, the same frequency offset of $\frac{1}{4}FSR$ was assumed. Given the same finesse F, $Z(f)$ can then be reduced to

$$Z(f) = \frac{F^2 \cos\left(\frac{6\pi f}{FSR}\right) + \left(3F^2 + 16F + 16\right) \cos\left(\frac{2\pi f}{FSR}\right)}{F^2 \sin\left(\frac{6\pi f}{FSR}\right) + \left(-3F^2 - 16F - 16\right) \sin\left(\frac{2\pi f}{FSR}\right)}. \tag{5.10}$$

Using Equation (5.6), the weighting factors $a_1(f)$ and $a_2(f)$ are calculated. Figure 5.2a shows the plot for the calculated parameters $a_1(f)$ and $a_2(f)$. As seen from the figure the value approach infinity for certain frequencies, e.g.

$$\lim_{f \to \frac{1}{8}FSR} a_1(f) = \infty. \tag{5.11}$$

An infinitely big factor is unwanted for a practical implementation. To avoid this, the factors can be scaled and piecewisely defined so that their values are always between -1 and 1. These scaled factors $a_{s1}(f)$ and $a_{s2}(f)$ are defined as:

$$a_{s1}(f) = \begin{cases} \frac{a_1}{a_2} = -Z(f), & \text{if } a_2 > a_1 \\ 1 & else \end{cases} \tag{5.12}$$

$$a_{s2}(f) = \begin{cases} \frac{a_2}{a_1} = \frac{-1}{Z(f)}, & \text{if } a_1 > a_2 \\ 1 & else \end{cases} \tag{5.13}$$

The graphical representation of the piecewisely defined scaled factors $a_{s1}(f)$ and $a_{s2}(f)$ can be seen in Figure 5.2b.

Figure 5.3 shows the result of the numeric simulation of the symmetric lock-in range of two etalons with a frequency offset of $\frac{1}{4}FSR$, here 25 GHz. The figure confirms the theory that the maximum symmetrical lock-in range of $\frac{1}{2}FSR$, here 50 GHz, is reached for all target frequencies.

5.4 Experimental validation

5.4.1 Setup

For experimental demonstration of the symmetrical lock-in range of $\frac{1}{2}FSR$ two etalons and a tunable laser were used. Figure 5.4 shows the optical set-up with the two wavelength lockers used in parallel. The etalons are two devices from the same series. It is possible to shift their transfer function in frequency by changing their operation temperature using the integrated TEC. The frequency offset between the two etalons and also their individual offset were chosen randomly by setting the TEC set points randomly within the allowed temperature range. Table 5.1 summarizes the parameters and Figure 5.5 shows the two measured transfer functions. Complementary, also a curve fit was performed which is also plotted.

In the following, first, the weighting factor method will be applied to a sample target frequency, and the calculations will be described in detail. Then, the same method will be applied to a fine target frequency grid to demonstrate the lock-in range for all frequencies within on period.

Device	FSR [GHz]	Finesse	peak offset [GHz]	relative offset [GHz]
A	100	~ 1.18	58.31	28.69
B	100	~ 1.10	29.65	

Table 5.1: Parameters of the etalons (Santec OWL-30) used in the experiment

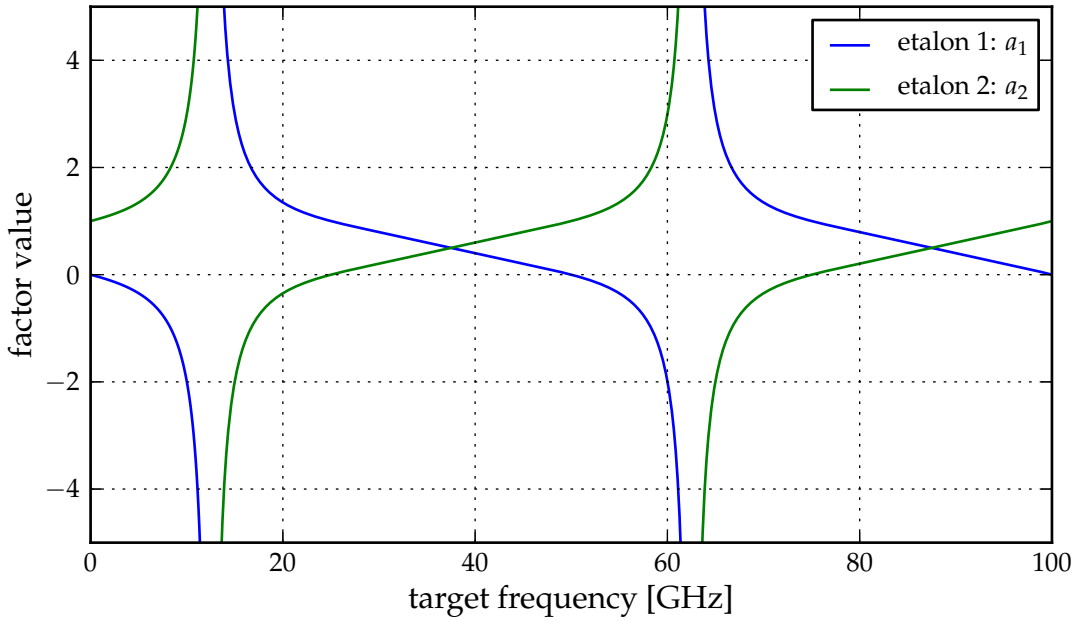

(a) two etalons weighting factors

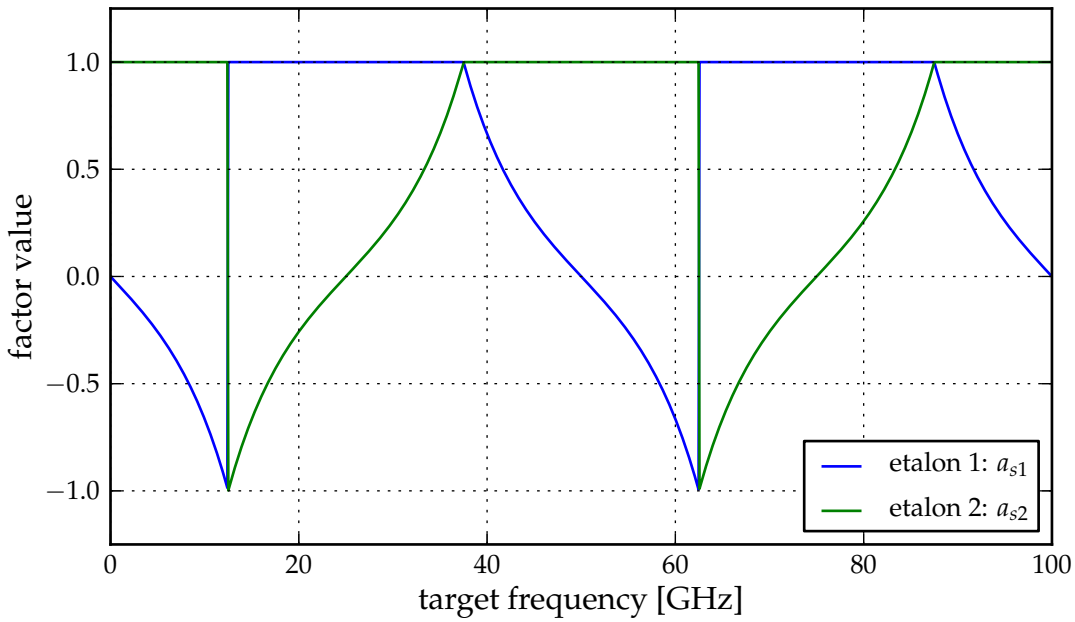

(b) two etalons scaled weighting factors

Figure 5.2: Etalon factor - scaled and unscaled

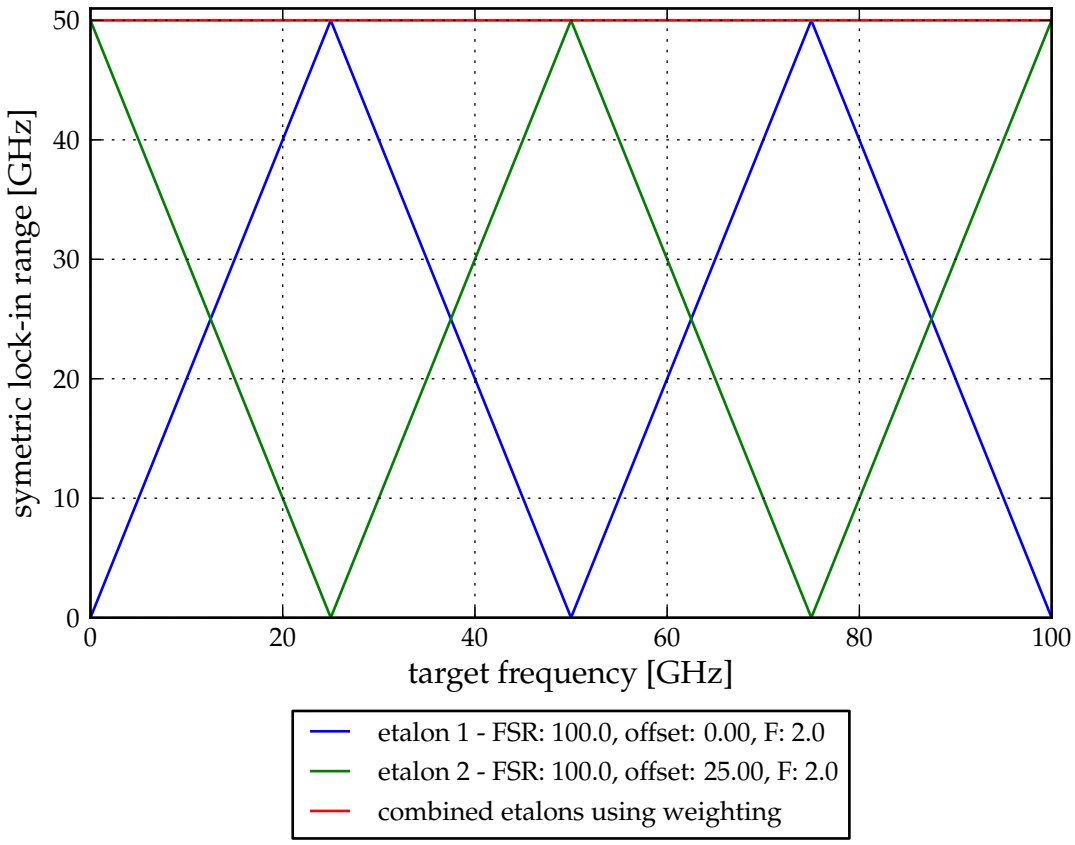

Figure 5.3: Two etalons including weighting method

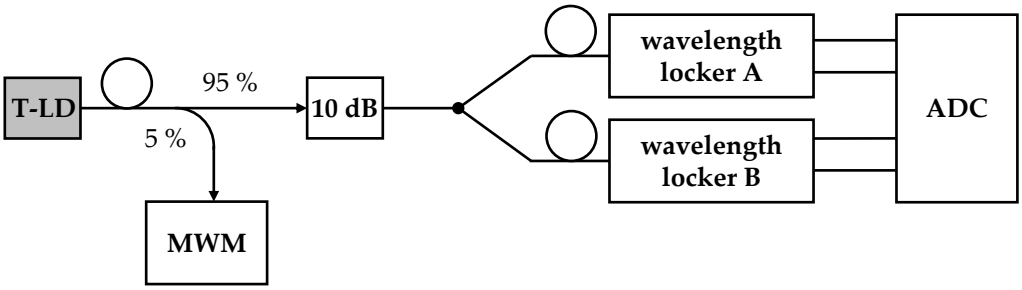

Figure 5.4: Experimental set-up for flex grid locking

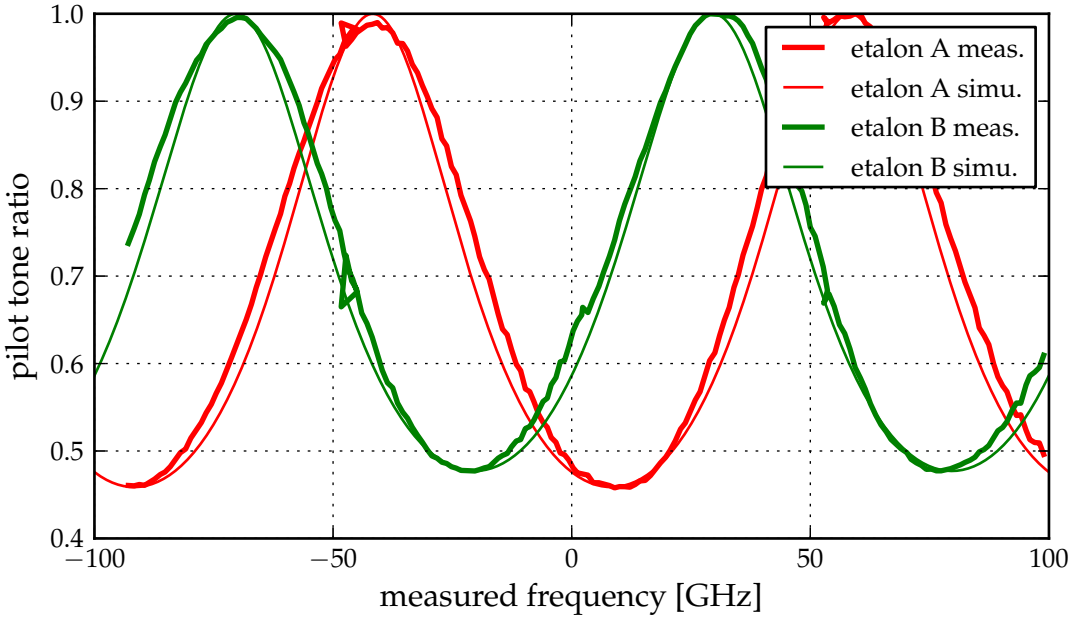

Figure 5.5: Transfer functions

5.4.2 Sample target frequency

The first step is to calculate the combined transfer function $T_c(f)$. Therefore the weighting factors $a_1(f)$ and $a_2(f)$, as defined in Equations (5.12) and (5.13), are calculated. For a sample target frequency of $f_t = 12.5\,\text{GHz}$ the combined transfer function $T_c(f)$, results in

$$T_c(f) = 0.486T_1(f) + 1.0T_2(f). \tag{5.14}$$

Figure 5.6 shows the measured and simulated combined transfer function. The figure shows the periodicity of $T_c(f)$ which is equal to the FSR, here 100 GHz. The vertical line at 12.5 GHz marks the target frequency, and the vertical lines at -37.5 GHz and 62.5 GHz mark the lock-in range boundaries. It can be seen from the figure that the following equation, which is necessary for providing information, is valid:

$$T_c(f) < T_c(f_t) \text{ if } f_t - \frac{1}{2}FSR < f < f_t \tag{5.15}$$

$$T_c(f) > T_c(f_t) \text{ if } f_t < f < f_t + \frac{1}{2}FSR. \tag{5.16}$$

For providing the tuning information (λ-error), it is useful to normalize the combined transfer function. This can be done in the same way, as it was done for a single etalon, see Equation (3.21).

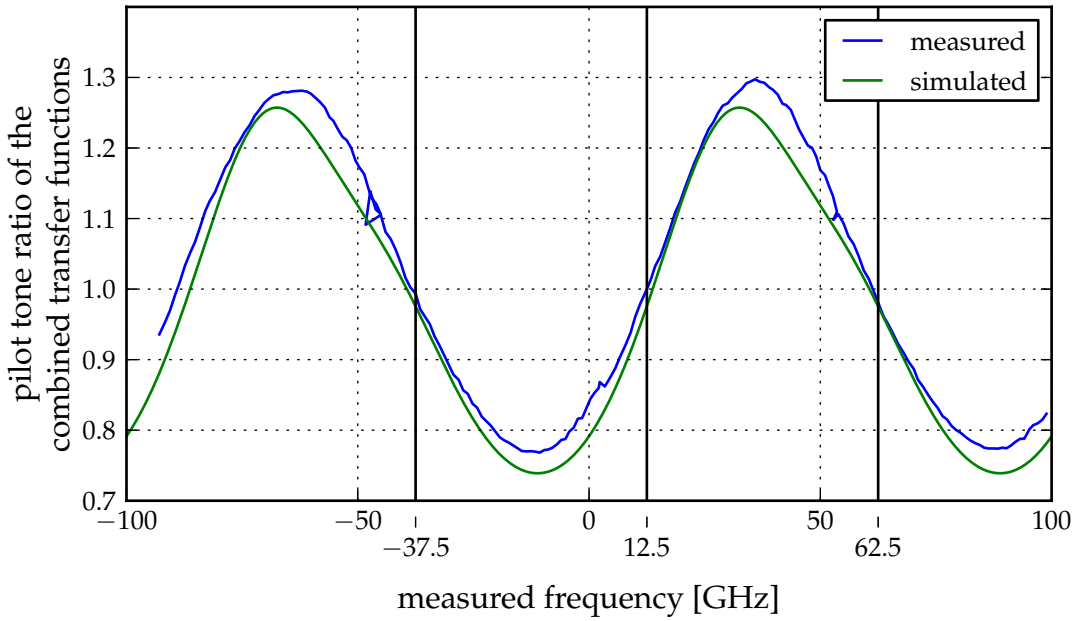

Figure 5.6: Combined ratio including the lock-in frequency and the left and right limits for a target channel of 12.5 GHz

Experimental validation of the tuning

To demonstrate the lock-in range, the laser tuning process was done twice. Once the laser started with a frequency close to the lower boundary of lock-in range ($f_t - \frac{1}{2}FSR$) and once close to the upper boundary ($f_t + \frac{1}{2}FSR$). In both cases the λ-error was continuously evaluated to change the laser frequency. Figure 5.7 shows the tuning process over time for both tests. The dotted lines mark the lock-in range boundaries. The blue curve marks the case where the start was near the lower boundary (−37.5 GHz) and the green curve the start near upper boundary (62.5 GHz). It can been seen that from both starting points the target frequency of 12.5 GHz is reached. The discontinuities at time steps 4 and 9 are longitudinal mode jumps, which were not compensated gaplessly, see Section 4.7.4 for an explanation of mode jumps.

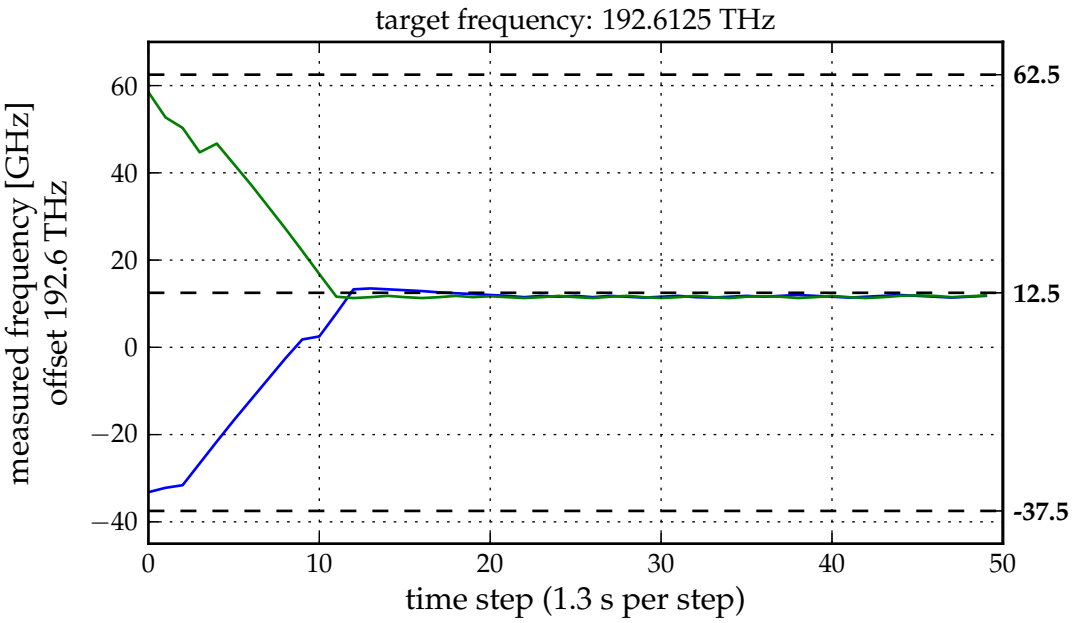

Figure 5.7: Tuning result of two runs for a target frequency of 192.6125 THz, discontinuities at time steps 5 and 9 are longitudinal mode jumps

5.4.3 Multiple channels

The same experiment, as for the sample channel, was repeated with several target frequencies each 1 GHz apart. Figure 5.8 shows the measured frequency offset to each target channel over time. The colour for each target channel is different and its value can be determined from the colour bar at the bottom of the figure. The figure shows that for every target channel a large lockin-range is achieved. For most target frequencies a lock-in

range from −45 GHz to 45 GHz, which is close to the theoretical possible −50 GHz to 50 GHz, was achieved. The tuning accuracy, for all channels measured after 25 time steps was −3 GHz to 2 GHz, which is in the same range as the single channel variant, demonstrated in Section 3.6.

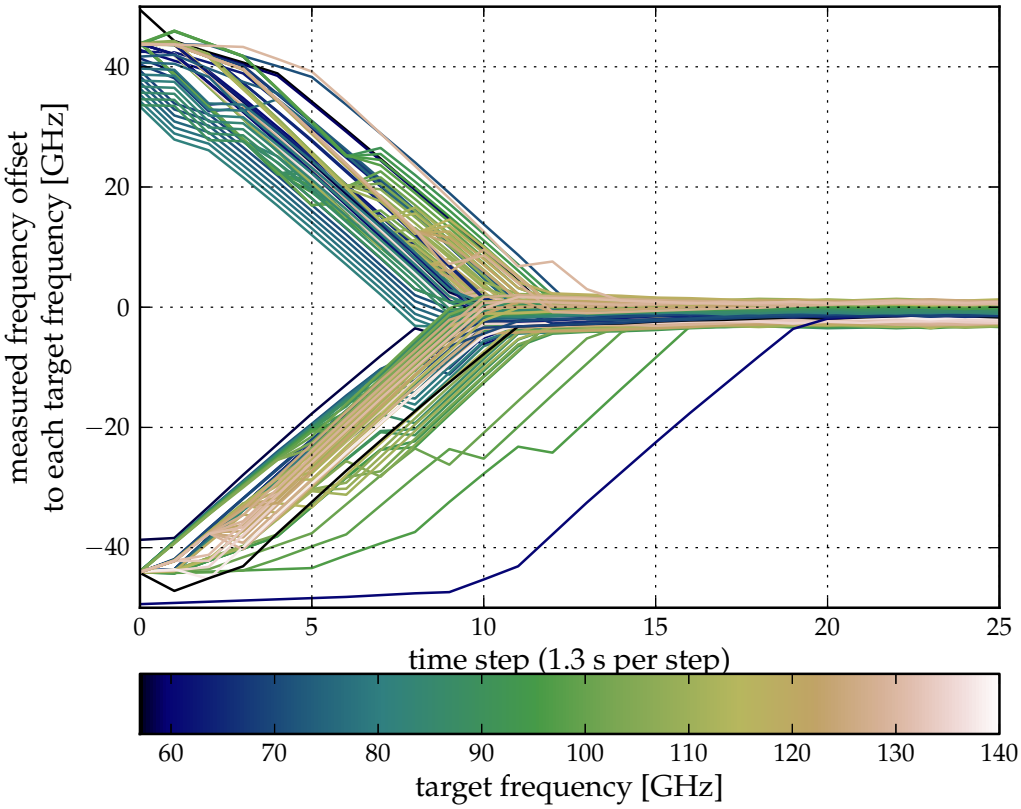

Figure 5.8: Flexgrid measurement for several channels, each 1 GHz apart

5.4.4 Conclusion

In this chapter, a new method for providing a large lock-in range of an arbitrary target channel frequency was introduced. It was theoretically shown that by using a second etalon with the same FSR, a combined transfer function for all target frequencies can be calculated which has a lock-in range of $\frac{1}{2}FSR$. The new proposed method was successfully demonstrated and can be used in several applications like Flexgrid.

6 General discussion, conclusion and outlook

6.1 Discussion and conclusion

First, Chapter 1 gives a broad introduction and history on PON systems. Then, a literature overview of commonly used monitoring and control functionality for WDM-PON was given.

In Chapter 2, a new pilot tone generation method based on a modified 8B/10B encoder has been introduced. The new modulation scheme was explained in theory and was also experimentally demonstrated in an FPGA. This new modulation method was then compared to the most commonly used existing ones. The results showed, that the new method has a better performance than the existing ones and shows the same performance as a signal without pilot tone. Additionally, it can be used with standard optical transceivers as no change in the optical components is needed.

With the usage of a pilot tone, it is possible to estimate the (average) optical power of the high speed data signal. Therefore it is necessary to estimate the pilot tone amplitude. With the usage of an HFT window function and an FFT, it is possible to estimate the amplitude and thus the optical power with an error of < 0.1 dB. Such an accurate estimation enables the usage of pilot tones for wavelength control.

Chapter 3 then showed how a centralised network wavelength control uses pilot tones to lower the overall cost of a WR-WDM-PON. The cost reduction is achieved by removing the local etalon filter for wavelength control from each ONU. Instead of a local etalon, only one etalon is installed at the OLT and each ONU applies a unique pilot tone. The OLT then estimates the optical power and the wavelength error (λ-error) for each ONU. This tuning information is then sent back to the ONU via an ECC and allows the ONU to tune itself to its target channel in two tuning phases: Initial phase and operation phase. First, during the initial phase only the optical power is optimized until the target channel is found. Then in second phase, the operation phase, only the wavelength error is evaluated. Despite being a very low cost approach, the two tuning phases allow the ONU to tune fast and very accurately. The complete system for demonstration of the

tuning of a full-band C-band tunable transceiver within a WR-WDM-PON concept was experimentally validated. The set-up over a single fibre with 50 km SSMF proofed that the target optical channel was found within ∼18 s. Also the long-term stability was tested, and it could be shown that the lasing frequency could be held within ±3 GHz of the target frequency over several hours.

Chapter 4 then showed how the cost of tunable transceivers can be further reduced by omitting the temperature controller and reducing the calibration effort. A laser without a TEC then has to operate within varying temperatures. The lasing frequency of the laser can be kept stable by measuring the laser chip temperature and using the wavelength tuning information provided by the OLT. Upon these two indications the laser injection currents can be changed according to generic equations or by interpolation of the calibration data. Both approaches can be applied to different laser types and have been successfully demonstrated for 2 laser types: the DS-DBR and SG-Y laser. The usage of generic equations also enables to completely omit the step of calibration during manufacturing but also has the lowest optical performance. The interpolation of calibration data requires some degree of calibration but provides a better overall performance.

In the last chapter, Chapter 5, a method for extending the lock-in range has been presented. The method incorporates a second etalon, and it was shown that by choosing the same FSR and an arbitrary frequency offset, a tuning information can be calculated to lock the frequency to any frequency within one period. The advantage of this method is that all frequencies have the the lock-in range of $\frac{1}{2}FSR$. Two main applications for this new method are seen. First, when a system has unequally spaced channels, e.g. 97.15 GHz as defined in ITU-T G.698.3, and only etalons of 100 GHz are available. Second, when flexible grid transceivers with a very small channel spacing of e.g. 6.25 GHz are used, the lock-in range becomes unusably small (3.125 GHz). In both cases the new, described and also experimentally demonstrated, method overcomes the shortcomings and is a reliable solution.

6.1.1 Limitations

The research shown here is a step towards a low-cost WR-WDM-PON. There are several more steps needed to have a commercial low-cost tunable laser product. One point of further research is the super-mode jump behaviour of different laser types. Further work is needed to reliably predict super mode jump without detailed calibration. Also the optical and electrical integration of OLT components has to be studied further and was not discussed in this work.

6.2 Outlook

Many approaches here use the commercially available laser types. However, when new laser types, like MEMS-VCSEL or the same laser types with other material, become commercially available the requirements for a low-cost tunable receiver may be met without the need for temperature compensation methods. Additionally, the findings of this work can also be used to lower the cost of tunable transceivers in other areas. One area of particular interest are the mobile backhaul/fronthaul passive systems. Here, the data from several antenna sites is processed at a central point. The used architecture is very similar to the WR-WDM-PON architecture, however, in the mobile backhaul market the price pressure is not as high as in access networks. Therefore, the backhaul market could be the first market for low-cost tunable transceivers and network-based wavelength control.

A List of publications

Most results and ideas presented in this thesis have been published by the author in the following journal papers, conferences papers, and patents:

Articles

K. Grobe, M. Roppelt, A. Autenrieth, J.-P. Elbers and M. Eiselt, 'Cost and energy consumption analysis of advanced WDM-PONs', *IEEE Communications Magazine*, vol. 49, no. 2, s25–s32, Feb. 2011, ISSN: 0163-6804. DOI: 10.1109/MCOM.2011.5706310.

Conferences

S. Pachnicke, M. Roppelt, A. Wonfor, J. Zhu, R. Penty, M. Eiselt and J.-P. Elbers, 'Centralized, Pilot-Tone-Based Wavelength-Locking for WDMPON with 1 GbE Data Rate', in *Photonic Networks, 14. 2013 ITG Symposium. Proceedings*, May 2013, pp. 1–4.

K. Grobe, M. Roppelt, M. Eiselt and J.-P. Elbers, 'Combined Reach, Client-Count, Power-Consumption, and Cost Analysis of WDM-based Next-Generation PON', in *37th European Conference and Exposition on Optical Communications*, Optical Society of America, 2011, We.10.P1.113. [Online]. Available: http://www.opticsinfobase.org/abstract.cfm?URI=ECOC-2011-We.10.P1.113.

M. Roppelt, K. Grobe, M. Eiselt and J.-P. Elbers, 'Efficient Broad-and Unicast in WDM-PON', VDE VERLAG GmbH, Mar. 2011. [Online]. Available: http://www.vde-verlag.de/proceedings-de/453339008.html.

M. Roppelt, M. H. Eiselt and M. Lawin, 'Experimental Demonstration of a New Pilot Tone Generation Method', in *Optical Fiber Communication Conference/National Fiber Optic Engineers Conference 2013*, Optical Society of America, Mar. 2013, JW2A.72. DOI: 10.1364/NFOEC.2013.JW2A.72. [Online]. Available: http://www.opticsinfobase.org/abstract.cfm?URI=NFOEC-2013-JW2A.72.

S. Pachnicke, A. Dochhan, M. Roppelt, M. H. Eiselt and J.-P. Elbers, 'Experimental Demonstration of Low-Cost S- / C-Band Broadcast-Overlay in WDM-PON', in *Asia Communications and Photonics Conference 2013*, Optical Society of America, 2013, AF4D.4. DOI: 10.1364/ACP.2013.AF4D.4. [Online]. Available: http://www.opticsinfobase.org/abstract.cfm?URI=ACP-2013-AF4D.4.

S. Pachnicke, M. Roppelt, M. Eiselt, A. Magee, P. Turnbull and J.-P. Elbers, 'Investigation of Wavelength Control Methods for Next Generation Passive Optical Access Networks', in *European Conference and Exhibition on Optical Communication*, Optical Society of America, 2012, P6.02. [Online]. Available: http://www.opticsinfobase.org/abstract.cfm?URI=ECEOC-2012-P6.02.

M. Roppelt, K. Grobe, M. Eiselt and J.-P. Elbers, 'Investigation of Wavelength Control Schemes in WDM-PONs', VDE VERLAG GmbH, May 2011. [Online]. Available: http://www.vde-verlag.de/proceedings-de/453346029.html.

D. Breuer, C. Lange, E. Weis, M. Eiselt, M. Roppelt, K. Grobe, J.-P. Elbers, S. Dahlfort, F. Cavaliere and D. Hood, 'Requirements and Solutions for Next-Generation Access', VDE VERLAG GmbH, May 2011. [Online]. Available: http://www.vde-verlag.de/proceedings-de/453346012.html.

M. Eiselt, M. Roppelt and M. Lawin, 'Single-Fibre Operation of a Metro Access System with Network Based Wavelength Control', in *39th European Conference and Exposition on Optical Communications*, Sep. 2013.

M. Roppelt, F. Pohl, K. Grobe, M. H. Eiselt and J.-P. Elbers, 'Tuning Methods for Uncooled Low-Cost Tunable Lasers in WDM-PON', in *National Fiber Optic Engineers Conference*, Optical Society of America, 2011, NTuB1. [Online]. Available: http://www.opticsinfobase.org/abstract.cfm?URI=NFOEC-2011-NTuB1.

M. Roppelt, M. H. Eiselt, K. Grobe and J.-P. Elbers, 'Tuning of an SG-Y Branch Laser for WDM-PON', in *Optical Fiber Communication Conference*, Optical Society of America, 2012, OW1B.4. [Online]. Available: http://www.opticsinfobase.org/abstract.cfm?URI=OFC-2012-OW1B.4.

K. Grobe, S. Pachnicke, M. Roppelt, J.-P. Elbers, M. Fellhofer, P. Neuber and M. Dietrich, 'WDM-PON Field Trial at Energie AG', VDE VERLAG GmbH, May 2013.

Patents

M. Eiselt and M. Roppelt, 'An optical frequency locking method and device for optical data transmission', EU Patent EP2573961 A1, 27th Mar. 2013.

J. Elbers, M. Eiselt, M. Roppelt and K. Grobe, 'An optical wavelength division multiplex (WDM) transmission system, especially a WDM passive optical network', EU Patent EP2525517 A1, 21st Nov. 2012.

K. Grobe and M. Roppelt, 'Method of operating an optical network element and optical network element', EU Patent EP2506476 A1, 3rd Oct. 2012.

S. Pachnicke, M. Eiselt, M. Roppelt, M. Lawin, K. Grobe and J. Elbers, 'A method and system for operating an optical transmission system', EU Patent EP2642676 A1, 25th Sep. 2013.

K. Grobe and M. Roppelt, 'Method of operating a primary optical node and a secondary optical node', EU Patent EP2675089 A1, 18th Dec. 2013.

B Generic equations of the DS-DBR laser

In the following the generic equations used in Section 4.6 will be described.

B.1 Front section

Figure B.1 shows the measurement result for all 7 front section pairs. As seen from the figure, the front section pairs have very similar behaviour for the relative wavelength shift. In order to show this in detail, the same measurement result is plotted in Figure B.2, however, relative to the wavelength at injection current of 0 mA.

For the usage in generic equations, it is better to have the relative wavelength change as an input variable. Figure B.2 shows the same data as Figure B.2 with changed x- and y-axis. Additionally, an approximation of third degree is plotted. The resulting equation is

$$\Delta\lambda = -0.182 I_{\text{front}}^3 + -0.990 I_{\text{front}}^2 + -4.822 I_{\text{front}} + 1.814 \tag{B.1}$$

with I_{front} being the injection current into the front section pair and $\Delta\lambda$ the relative wavelength change in nm.

B.2 Rear section

The same measurement, as for the front section, is done for rear section. Figure B.4 shows relative wavelength change versus the injection current into the rear section. The approximation for the rear current injection is then:

$$\Delta\lambda = 0.194 I_{\text{rear}}^3 + -1.053 I_{\text{rear}}^2 + 4.385 I_{\text{rear}} + -0.675 \tag{B.2}$$

with I_{rear} being the injection current into the rear section pair and $\Delta\lambda$ the relative wavelength change in nm.

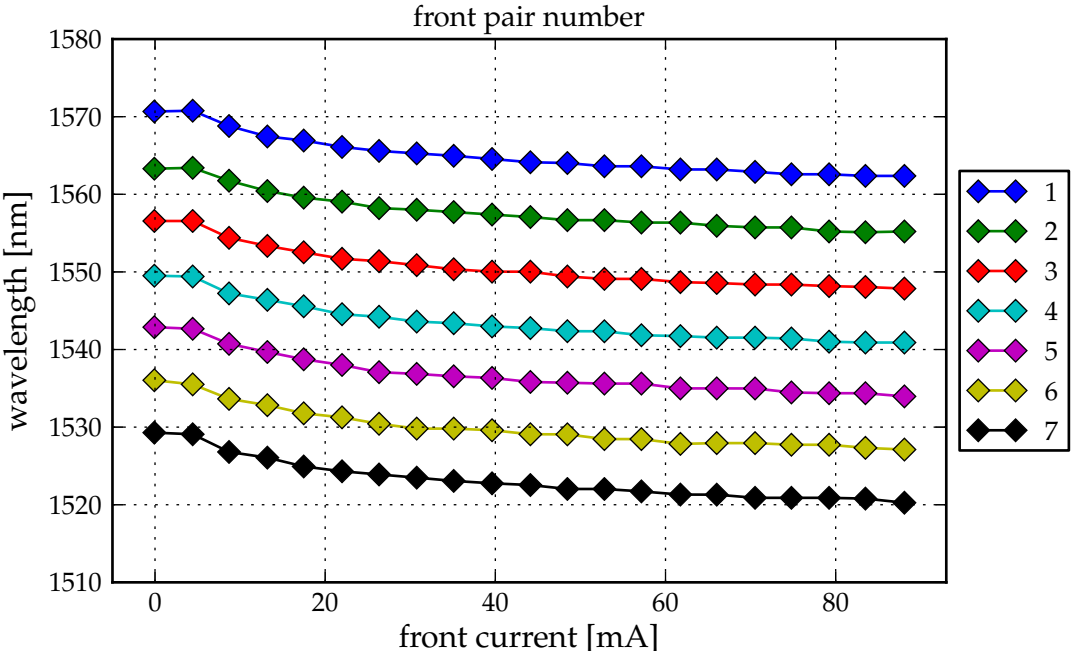

Figure B.1: Front grating behaviour showing the complete tuning range

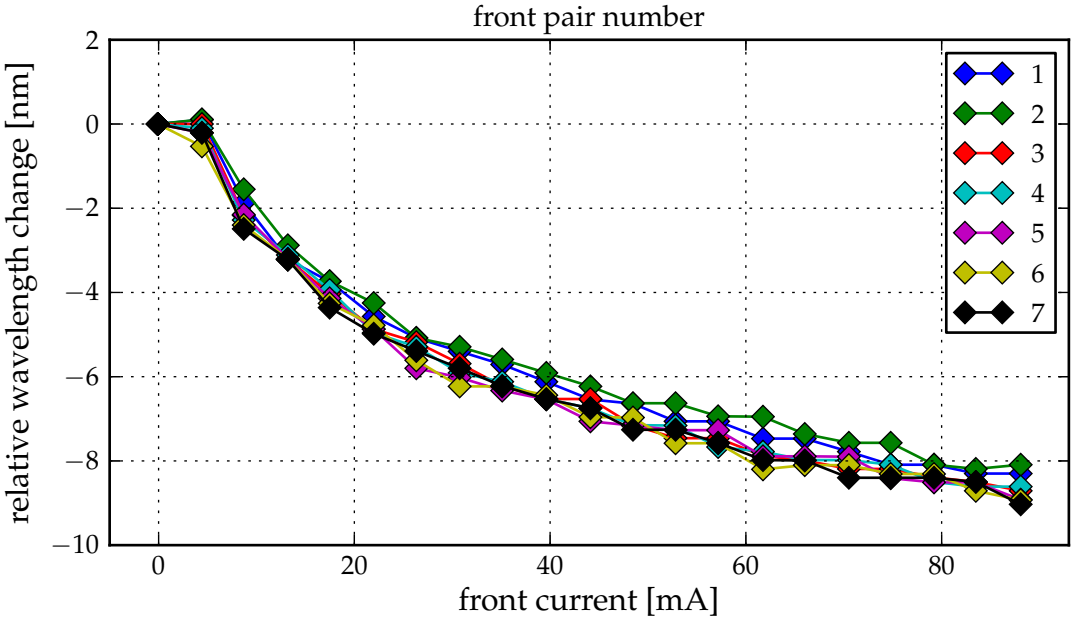

Figure B.2: Front grating relative behaviour

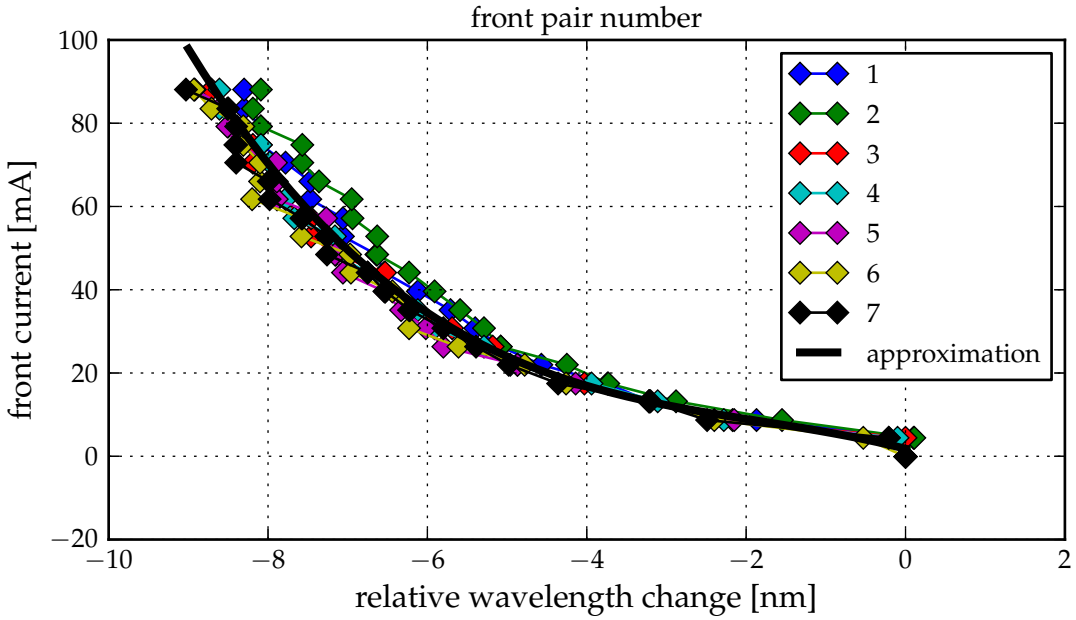

Figure B.3: Front grating relative behaviour (with changed axis and with approximation)

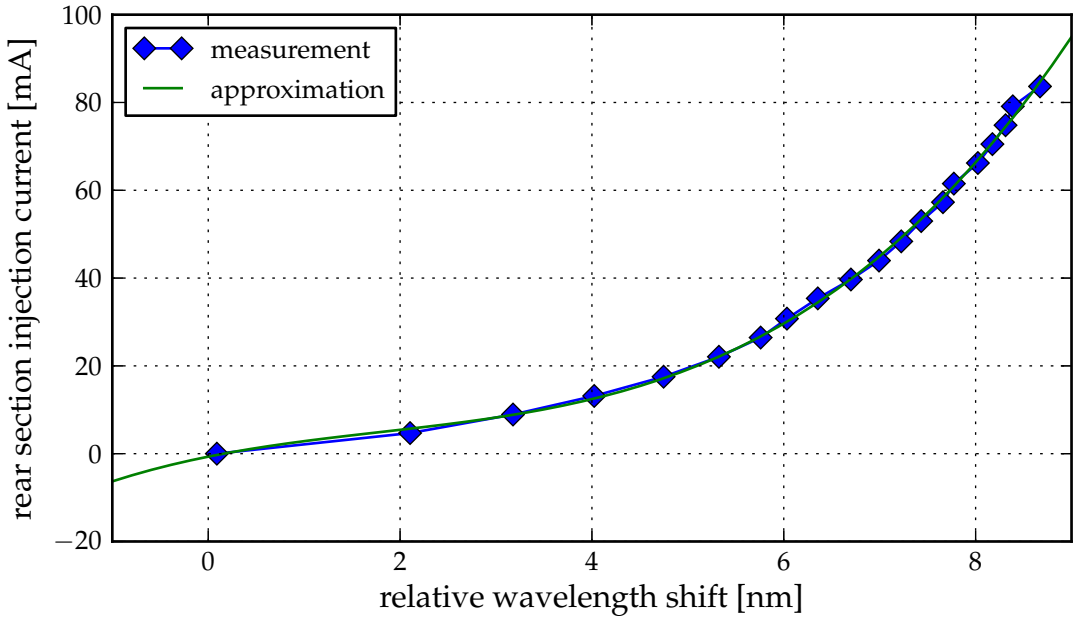

Figure B.4: Rear grating behaviour

Acronyms

μC	micro controller
ADC	analog-to-digital converter
ADSL	asymmetric digital subscriber line
AlQ	aluminium quaternary
AM	amplitude modulation
AON	active optical network
APD	avalanche photo diode
AR	anti reflection
ATM	asynchronous transfer mode
AWG	arrayed waveguide grating
BER	bit error rate
BLS	broadband light source
BPSK	binary phase shift keying
CD	chromatic dispersion
CDM	code division multiplexing
CDR	clock and data recovery
CO	central office
CPE	customer premises equipment
CRPAT	compliant random pattern
CW	continuous wave
CWDM	coarse WDM
DAC	digital-to-analog converter
DBR	distributed Bragg reflector
DD	direct detection
DDS	direct digital synthesis
DeMUX	demultiplexer
DFT	digital Fourier transformation
DOCSIS	Data Over Cable Service Interface Specification
DS	downstream
DS-DBR	digital supermode - distributed Bragg reflector
DSP	digital signal processor / processing
ECC	embedded communication channel
EDFA	erbium doped fibre amplifier

EPON	Ethernet PON
FDM	frequency division multiplexing
FFT	fast Fourier transformation
FPGA	field programmable gate array
FSAN	full service access network
FSR	free spectral range
FTTB	fibre-to-the-business / building
FTTC	fibre-to-the-curb
FTTCab	fibre-to-the-cabinet
FTTH	fibre-to-the-home
FTTN	fibre-to-the-node / neighbourhood
FTTP	fibre-to-the-premises, includes FTTH and FTTB
GbE	Gigabit Ethernet
GPON	Gigabit PON
HFC	hybrid fibre coax
HFT	high dynamic range flattop
IEEE	Institute of Electrical and Electronics Engineers
IL	insertion loss
IL-FPLD	injection-locked Fabry-Perot laser diode
ISDN	integrated services digital network
iTLA	integrated tunable laser assembly
ITU	International Telecommunication Union
LA	limiting amplifier
LC	little connector
LD	laser diode
LED	light emitting diode
LOS	loss of signal
LPF	low-pass filter
MAC	media access control
MEMS	micro-electromechanical systems
MFL	multi-frequency laser
MG-Y	modulated grating Y-branch
MGT	multi-Gigabit transceiver
MMI	multi-mode interferometer
MQW	multi-quantum well
MUX	multiplexer
MZM	Mach-Zehnder modulator
NENBW	normalized equivalent noise bandwidth
NGA	next-generation access

NGOA	next generation optical access
OAM	operations, administration and maintenance
OCDMA	optical code division multiple access
ODN	optical distribution network
OFDMA	orthogonal frequency-division multiple access
ONT	optical network termination
ONU	optical network unit
OOK	on-off keying
OPM	optical performance monitoring
OSA	optical spectrum analyser
OTDR	optical time-domain reflectometer
P-I	output power vs. injection current
P2MP	point-to-multi-point
PC	personal computer
PD	photo diode
PIN	positive intrinsic negative diode
PLOAM	physical layer OAM
PON	passive optical network
PRBS	pseudo-random bit stream
RD	running disparity
REAM	reflective electro-absorption modulator
RN	remote node
ROSA	receiver optical sub-assembly
RSOA	reflective semiconductor optical amplifier
RSSI	received signal strength indicator
RX	receiver
SCM	subcarrier multiplexing
SDM	space division multiplexing
SFP	small form factor pluggable
SFW	single fibre working
SG-DBR	sampled grating - distributed Bragg reflector
SG-Y	sampled grating Y-branch
SMSR	side-mode suppression ratio
SNR	signal-to-noise ratio
SOA	semiconductor optical amplifier
SONET	synchronous optical network
SSMF	standard single-mode optical fibre
TDMA	time division multiple access
TEC	thermoelectric cooler
TIA	transimpedance amplifier
TOSA	transmitter optical sub-assembly

TV	television
TWDM	time and wavelength division multiplexing
TX	transmitter
UDWDM	ultra dense WDM
US	upstream
VCSEL	vertical-cavity surface-emitting laser
VDSL	very-high-bit-rate digital subscriber line
VHDL	very high speed integrated circuit hardware description
VOA	variable optical attenuator
WBF	wavelength blocking filter
WDM	wavelength division multiplexing
WR	wavelength routed
WS	wavelength selected
XFP	10 Gigabit Small Form Factor Pluggable
XG-PON1	10-Gigabit-capable passive optical network generation 1

List of Figures

List of Tables

Bibliography

[1] ITU-T, *G.983.x - Broadband optical access systems based on Passive Optical Networks (PON)*, ITU-T, Jan. 2005. [Online]. Available: http://www.itu.int/rec/T-REC-G.983.1/en.

[2] J. Nielsen. (5th Apr. 1998). Nielsen's Law of Internet Bandwidth, [Online]. Available: http://www.useit.com/alertbox/980405.html (visited on 26/07/2012).

[3] T. Kuroda, 'Current status on super HDTV development in Japan', in *Proc. IEEE Int Broadband Multimedia Systems and Broadcasting (BMSB) Symp*, 2010. DOI: 10.1109/ISBMSB.2010.5463174. [Online]. Available: http://ieeexplore.ieee.org/stamp/stamp.jsp?arnumber=5463174.

[4] K. Kitayama, X. Wang and N. Wada, 'OCDMA Over WDM PON—Solution Path to Gigabit-Symmetric FTTH', *J. Lightwave Technol.*, vol. 24, no. 4, p. 1654, Apr. 2006. [Online]. Available: http://jlt.osa.org/abstract.cfm?URI=jlt-24-4-1654.

[5] D. Qian, J. Hu, P. Ji, T. Wang and M. Cvijetic, '10-Gb/s OFDMA-PON for Delivery of Heterogeneous Services', in *Optical Fiber Communication Conference and Exposition and The National Fiber Optic Engineers Conference*, Optical Society of America, 2008, OWH4. [Online]. Available: http://www.opticsinfobase.org/abstract.cfm?URI=OFC-2008-OWH4.

[6] Y. Mochida, 'Technologies for local-access fibering', *IEEE Communications Magazine*, vol. 32, no. 2, pp. 64–73, 1994. DOI: 10.1109/35.259801. [Online]. Available: http://ieeexplore.ieee.org/stamp/stamp.jsp?arnumber=259801.

[7] A. Banerjee, Y. Park, F. Clarke, H. Song, S. Yang, G. Kramer, K. Kim and B. Mukherjee, 'Wavelength-division-multiplexed passive optical network (WDM-PON) technologies for broadband access: a review [Invited]', *Journal of Optical Networking*, vol. 4, no. 11, pp. 737–758, Nov. 2005. DOI: 10.1364/JON.4.000737.

[8] D. Breuer, C. Lange, E. Weis, M. Eiselt, M. Roppelt, K. Grobe, J.-P. Elbers, S. Dahlfort, F. Cavaliere and D. Hood, 'Requirements and Solutions for Next-Generation Access', VDE VERLAG GmbH, May 2011. [Online]. Available: http://www.vde-verlag.de/proceedings-de/453346012.html.

[9] IEEE, *802.3ah-2004 - IEEE Standard for Information Technology- Telecommunications and Information Exchange Between Systems- Local and Metropolitan Area Networks-Specific Requirements Part 3: Carrier Sense Multiple Access With Collision Detection (CSMA/CD) Access Method and Physical Layer Specifications Amendment: Media Access Control Parameters, Physical Layers, and Management Parameters for Subscriber Access Networks*, Sep. 2004. DOI: 10.1109/IEEESTD.2004.94617.

[10] ITU-T, *G.984.x - Gigabit-capable passive optical networks (GPON): General characteristics*, ITU-T, Mar. 2008. [Online]. Available: http://www.itu.int/rec/T-REC-G.984.1/en.

[11] IDATE. (Jul. 2009). FTTx Market Report, [Online]. Available: http://www.telecoms.com/files/2009/09/world-fttx-market-idate200908.pdf.

[12] C. F. Lam, *Passive Optical Networks: Principles and Practice*, 1st ed. Academic Press, Oct. 2007, ISBN: 9780123738530.

[13] ITU-T, *G.987.x - 10-Gigabit-capable passive optical network (XG-PON) systems*, ITU-T, Jun. 2012. [Online]. Available: http://www.itu.int/rec/T-REC-G.987.1/en.

[14] IEEE, *802.3av-2009 - IEEE Standard for Information technology - Telecommunications and information exchange between systems - Local and metropolitan area networks - Specific requirements Part 3: Carrier Sense Multiple Access with Collision Detection (CSMA/CD) Access Method and Physical Layer Specifications Amendment 1: Physical Layer Specifications and Management Parameters for 10 Gb/s Passive Optical Networks*, Oct. 2009. DOI: 10.1109/IEEESTD.2009.5294950.

[15] H. Suzuki, M. Fujiwara, T. Suzuki, N. Yoshimoto, H. Kimura and M. Tsubokawa, 'Wavelength-Tunable DWDM-SFP Transceiver with a Signal Monitoring Interface and Its Application to Coexistence-Type Colorless WDM-PON', in *Proc. 33rd European Conf Optical Communication - Post-Deadline Papers (published 2008) and Exhibition of*, 2007, pp. 1–2. [Online]. Available: http://ieeexplore.ieee.org/stamp/stamp.jsp?arnumber=5760071.

[16] S. Smolorz, H. Rohde, E. Gottwald, D. W. Smith and A. Poustie, 'Demonstration of a Coherent UDWDM-PON with Real-Time Processing', in *National Fiber Optic Engineers Conference*, Optical Society of America, 2011, PDPD4. [Online]. Available: http://www.opticsinfobase.org/abstract.cfm?URI=NFOEC-2011-PDPD4.

[17] S. Kamei, 'Recent Progress on Athermal AWG Wavelength Multiplexer', in *Optical Fiber Communication Conference*, Optical Society of America, 2009, OWO1. [Online]. Available: http://www.opticsinfobase.org/abstract.cfm?URI=OFC-2009-OWO1.

[18] ITU-T, *G-series Recommendations - Supplement 39 - Optical system design and engineering considerations*, Dec. 2008. [Online]. Available: http://www.itu.int/rec/T-REC-G.Sup39-200812-I.

[19] ——, *G.698.x - Multichannel seeded DWDM applications with single-channel optical interfaces*, Feb. 2012. [Online]. Available: http://www.itu.int/rec/T-REC-G.698.3/en.

[20] W. Lee, M. Y. Park, S. H. Cho, J. Lee, C. Kim, G. Jeong and B. W. Kim, 'Bidirectional WDM-PON based on gain-saturated reflective semiconductor optical amplifiers', *IEEE Photonics Technology Letters*, vol. 17, no. 11, pp. 2460–2462, 2005. DOI: 10.1109/LPT.2005.858148. [Online]. Available: http://ieeexplore.ieee.org/stamp/stamp.jsp?arnumber=1522353.

[21] N. Calabretta, M. Presi, R. Proietti, G. Contestabile and E. Ciaramella, 'A novel bidirectional WDM/TDM-PON using DPSK downstream signals and a custom AWG', in *Proc. 33rd European Conf Optical Communication (ECOC) and Ehxibition of*, 2007, pp. 1–2. [Online]. Available: http://ieeexplore.ieee.org/stamp/stamp.jsp?arnumber=5758388.

[22] C. Arellano, C. Bock, K.-D. Langer and J. Prat, 'Optical Network Units based on Semiconductor Optical Amplifiers in Single-Wavelength Single-Fiber Access Networks', VDE VERLAG GmbH, 10th Dec. 2005. [Online]. Available: http://www.vde-verlag.de/proceedings-de/453339008.html.

[23] P. Healey, P. Townsend, C. Ford, L. Johnston, P. Townley, I. Lealman, L. Rivers, S. Perrin and R. Moore, 'Spectral slicing WDM-PON using wavelength-seeded reflective SOAs', *Electronics Letters*, vol. 37, no. 19, pp. 1181–1182, 2001. DOI: 10.1049/el:20010786. [Online]. Available: http://ieeexplore.ieee.org/stamp/stamp.jsp?arnumber=953335.

[24] N. Deng, C.-K. Chan and L.-K. Chen, 'A centralized-light-source WDM access network utilizing inverse-RZ downstream signal with upstream data remodulation', *Optical Fiber Technology*, vol. 13, no. 1, pp. 18–21, 2007, ISSN: 1068-5200. DOI: 10.1016/j.yofte.2006.03.006. [Online]. Available: http://www.sciencedirect.com/science/article/pii/S1068520006000198.

[25] H. S. Chung, B. K. Kim, H. Park, S. H. Chang, M. J. Chu and K. J. Kim, 'Effects of inverse-RZ and Manchester code on a wavelength re-used WDM-PON', in *Proc. 19th Annual Meeting of the IEEE Lasers and Electro-Optics Society LEOS 2006*, 2006, pp. 298–299. DOI: 10.1109/LEOS.2006.279066. [Online]. Available: http://ieeexplore.ieee.org/stamp/stamp.jsp?arnumber=4054175.

[26] M. Presi, R. Proietti, K. Prince, G. Contestabile and E. Ciaramella, 'A 80 km reach fully passive WDM-PON based on reflective ONUs', *Opt. Express*, vol. 16, no. 23, pp. 19 043–19 048, Nov. 2008. DOI: 10.1364/OE.16.019043. [Online]. Available: http://www.opticsexpress.org/abstract.cfm?URI=oe-16-23-19043.

[27] E. Wong, K. L. Lee and T. Anderson, 'Directly Modulated Self-Seeding Reflective SOAs as Colorless Transmitters for WDM Passive Optical Networks', in *Optical Fiber Communication Conference and Exposition and The National Fiber Optic Engineers Conference*, Optical Society of America, 2006, PDP49. [Online]. Available: http://www.opticsinfobase.org/abstract.cfm?URI=OFC-2006-PDP49.

[28] F.-T. An, K. S. Kim, D. Gutierrez, S. Yam, E. Hu, K. Shrikhande and L. G. Kazovsky, 'SUCCESS: a next-generation hybrid WDM/TDM optical access network architecture', *IEEE/OSA Journal of Lightwave Technology*, vol. 22, no. 11, pp. 2557–2569, 2004. DOI: 10.1109/JLT.2004.836768. [Online]. Available: http://ieeexplore.ieee.org/stamp/stamp.jsp?arnumber=1353388.

[29] P. W. Shumate, 'Fiber-to-the-Home: 1977–2007', *J. Lightwave Technol.*, vol. 26, no. 9, pp. 1093–1103, May 2008. [Online]. Available: http://jlt.osa.org/abstract.cfm?URI=jlt-26-9-1093.

[30] Full Service Access Network Organization. (16th Jul. 2012). Industry Experts in FSAN Agree on Technology for NG-PON2 for Greater System Capability and Enhanced Services, [Online]. Available: www.fsan.org/news/ (visited on 26/07/2012).

[31] P. Chanclou, A. Cui, F. Geilhardt, H. Nakamura and D. Nesset, 'Network operator requirements for the next generation of optical access networks', *Network, IEEE*,

vol. 26, no. 2, pp. 8–14, Mar. 2012, ISSN: 0890-8044. DOI: 10.1109/MNET.2012.6172269.

[32] D. R. Anderson, L. M. Johnson and F. G. Bell, *Troubleshooting Optical Fiber Networks - Understanding and Using Optical Time-Domain Reflectometers*. Academic Press, 2004, ISBN: 978-0-080-49236-0.

[33] K. Tanaka, H. Izumita, N. Tomita and Y. Inoue, 'In-service individual line monitoring and a method for compensating for the temperature-dependent channel drift of a WDM-PON containing an AWGR using a 1.6 μm tunable OTDR', in *Integrated Optics and Optical Fibre Communications, 11th International Conference on, and 23rd European Conference on Optical Communications (Conf. Publ. No.: 448)*, vol. 3, Sep. 1997, 295–298 vol.3. DOI: 10.1049/cp:19971548.

[34] J. Lee, J. Park, J. G. Shim, H. Yoon, J. H. Kim, K. Kim, J. Byun and N. Park, 'In-service monitoring of 16 port x 32 wavelength bi-directional WDM-PON systems with a tunable, coded optical time domain reflectometry', *Opt. Express*, vol. 15, no. 11, pp. 6874–6882, May 2007. DOI: 10.1364/OE.15.006874. [Online]. Available: http://www.opticsexpress.org/abstract.cfm?URI=oe-15-11-6874.

[35] G. W. Schinn, H. Chen, R. Baribault, M. Leclerc, S. Perron, B. Ruchet, E. Morin-Drouin and E. Thomassin, 'Widely Tunable SOA-Based OTDR Employing a Cost-Effective Source Configuration', in *Optical Fiber Communication Conference*, Optical Society of America, 2012, JW2A.36. [Online]. Available: http://www.opticsinfobase.org/abstract.cfm?URI=OFC-2012-JW2A.36.

[36] J. Park, J. Baik and C. Lee, 'Fault-detection technique in a WDM-PON', *Opt. Express*, vol. 15, no. 4, pp. 1461–1466, Feb. 2007. DOI: 10.1364/OE.15.001461. [Online]. Available: http://www.opticsexpress.org/abstract.cfm?URI=oe-15-4-1461.

[37] K. W. Lim, E. S. Son, K. Han and Y. Chung, 'Fault localization in WDM passive optical network by reusing downstream light sources', *Photonics Technology Letters, IEEE*, vol. 17, no. 12, pp. 2691–2693, Dec. 2005, ISSN: 1041-1135. DOI: 10.1109/LPT.2005.859178.

[38] S.-B. Park, O. Jung, H. Shin, D. Shin, S. Hwang, Y. Oh and C. Shim, 'Optical fault monitoring method using broadband light source in WDM-PON', *Electronics Letters*, vol. 42, no. 4, pp. 239–241, Feb. 2006, ISSN: 0013-5194. DOI: 10.1049/el:20063958.

[39] J. H. Lee, Y.-G. Han, S. B. Lee and C. H. Kim, 'WDM-PON Architecture with C-Band OLT, L-Band ONU, and U-Band Monitoring Based on FP-LDs Wavelength-Locked by a Single, Depolarized, CW Supercontinuum', in *Optical Fiber Communication Conference and Exposition and The National Fiber Optic Engineers Conference*, Optical Society of America, 2007, OTuG3. [Online]. Available: http://www.opticsinfobase.org/abstract.cfm?URI=OFC-2007-OTuG3.

[40] E. Wong, X. Zhao and C. J. Chang-Hasnain, 'Novel Fault Monitoring and Localization Scheme in WDM-PONs with Upstream VCSEL Transmitters', in *Optical Fiber Communication Conference and Exposition and The National Fiber Optic Engineers Conference*, Optical Society of America, 2007, OThE3. [Online]. Available: http://www.opticsinfobase.org/abstract.cfm?URI=OFC-2007-OThE3.

[41] U. Hilbk, M. Burmeister, B. Hoen, T. Hermes, J. Saniter and F.-J. Westphal, 'Selective OTDR Measurements at the central office of individual fiber links in a PON', in *Conference on Optical Fiber Communications*, Optical Society of America, 1997, TuK3. [Online]. Available: http://www.opticsinfobase.org/abstract.cfm?URI=OFC-1997-TuK3.

[42] K. Yuksel, V. Moeyaert, M. Wuilpart and P. Megret, 'Optical layer monitoring in Passive Optical Networks (PONs): A review', in *10th Anniversary International Conference on Transparent Optical Networks, 2008. ICTON 2008.*, vol. 1, Jun. 2008, pp. 92–98. DOI: 10.1109/ICTON.2008.4598379.

[43] K. Nakama, K. Shimmo, H. Yamamoto, K. Nakamura, M. Hori, M. Kawazu, H. Nagata, N. Komaba, Y. Arima, S. Nagasaka, Y. Satoh and Y. Sasaki, 'Compact multichannel optical power monitor module for DWDM networks using a novel glass diffraction grating', in *Optical Communication, 2001. ECOC '01. 27th European Conference on*, vol. 3, 2001, 426–427 vol.3. DOI: 10.1109/ECOC.2001.989698.

[44] Maxim Integrated Products, *DS1843 - Fast Sample-and-Hold Circuit*, Feb. 2012. [Online]. Available: http://datasheets.maximintegrated.com/en/ds/DS1843.pdf.

[45] J. Teeter and R. Dalton, 'Measurement of burst mode optical power over multiple bursts', Patent US 7414234, 19th Aug. 2008.

[46] G. Hill, P. Chidgey, F. Kaufhold, T. Lynch, O. Sahlen, M. Gustavsson, M. Janson, B. Lagerstrom, G. Grasso, F. Meli, S. Johansson, J. Ingers, L. Fernandez, S. Rotolo, A. Antonielli, S. Tebaldini, E. Vezzoni, R. Caddedu, N. Caponio, F. Testa, A. Scavennec, M. O''Mahony, J. Zhou, A. Yu, W. Sohler, U. Rust and H. Herrmann, 'A transport

network layer based on optical network elements', *Lightwave Technology, Journal of*, vol. 11, no. 5, pp. 667–679, May 1993, ISSN: 0733-8724. DOI: 10.1109/50.233232.

[47] S. Schmid, S. Morasca, D. Scarano and H. Herrmann, 'High-performance integrated acousto-optic channel analyzer', in *Conference on Optical Fiber Communications*, Optical Society of America, 1997, TuC3. [Online]. Available: http://www.opticsinfobase.org/abstract.cfm?URI=OFC-1997-TuC3.

[48] S. K. Shin, C.-H. Lee and Y. C. Chung, 'A novel frequency and power monitoring method for WDM network', in *Optical Fiber Communication Conference*, Optical Society of America, 1998, WJ7. [Online]. Available: http://www.opticsinfobase.org/abstract.cfm?URI=OFC-1998-WJ7.

[49] Y. Chung and L. Stulz, 'Synchronized etalon filters for standardizing WDM transmitter laser wavelengths', *Photonics Technology Letters, IEEE*, vol. 5, no. 2, pp. 186–189, Feb. 1993, ISSN: 1041-1135. DOI: 10.1109/68.195999.

[50] K. Park, S. K. Shin and Y. Chung, 'Simple monitoring technique for WDM networks', *Electronics Letters*, vol. 35, no. 5, pp. 415–417, Mar. 1999, ISSN: 0013-5194. DOI: 10.1049/el:19990260.

[51] K. Park, S. Shin, H. Ji, H. Woo and Y. Chung, 'A multi-wavelength locker for WDM system', in *Optical Fiber Communication Conference, 2000*, vol. 2, 2000, 73–75 vol.2. DOI: 10.1109/OFC.2000.868244.

[52] C. C. K. Chan, *Optical Performance Monitoring: Advanced Techniques for Next-Generation Photonic Networks*. Academic Press, 2010, ISBN: 0123749506.

[53] G. Rossi, T. Dimmick and D. Blumenthal, 'Optical performance monitoring in reconfigurable WDM optical networks using subcarrier multiplexing', *Lightwave Technology, Journal of*, vol. 18, no. 12, pp. 1639–1648, 2000, ISSN: 0733-8724. DOI: 10.1109/50.908673.

[54] H. Ji, K. Park, J. Lee, H. Chung, E. Son, K. Han, S. Jun and Y. Chung, 'Optical performance monitoring techniques based on pilot tones for WDM network applications', *J. Opt. Netw.*, vol. 3, no. 7, pp. 510–533, Jul. 2004. DOI: 10.1364/JON.3.000510. [Online]. Available: http://jon.osa.org/abstract.cfm?URI=jon-3-7-510.

[55] I. Glover and P. Grant, *Digital Communications*, 3rd ed. Pearson Education, 2009, ISBN: 978-0-273-71830-7.

[56] Analog Devices, Inc., *ADN2891 - Limiting Amplifier Datasheet*, Jul. 2005. [Online]. Available: http://www.analog.com/static/imported-files/data_sheets/ADN2891.pdf.

[57] J. Baik, K. Park, T. Oh and C.-H. Lee, 'Analysis of Penalty Due to Low-Frequency Intensity Modulation in Optical Transmission Systems', *J. Lightwave Technol.*, vol. 21, no. 12, p. 3300, Dec. 2003. [Online]. Available: http://jlt.osa.org/abstract.cfm?URI=jlt-21-12-3300.

[58] M. Murphy, F. Barany and M. O'Flanagan, 'AN-658 Optical Channel Identification on the ADN284x Laser Drivers (Part I)', *Analog Devices*, 2003. [Online]. Available: http://www.analog.com/static/imported-files/application_notes/901607208AN658_0.pdf.

[59] A. X. Widmer and P. A. Franaszek, 'A DC-Balanced, Partitioned-Block, 8B/10B Transmission Code', *IBM Journal of Research and Development*, vol. 27, no. 5, pp. 440–451, 1983. DOI: 10.1147/rd.275.0440. [Online]. Available: http://ieeexplore.ieee.org/stamp/stamp.jsp?arnumber=5390392.

[60] American National Standard for Information Systems, *ANSI X3.230-1994 - Information Technology - Fibre Channel Physical and Signaling Interface. (FC-PH)*, 1994.

[61] H. Frazier, 'The 802.3z Gigabit Ethernet Standard', *Network, IEEE*, vol. 12, no. 3, pp. 6–7, May 1998, ISSN: 0890-8044. DOI: 10.1109/65.690946.

[62] D. Rife and R. Boorstyn, 'Single tone parameter estimation from discrete-time observations', *IEEE Transactions on Information Theory*, vol. 20, no. 5, pp. 591–598, 1974. DOI: 10.1109/TIT.1974.1055282. [Online]. Available: http://ieeexplore.ieee.org/stamp/stamp.jsp?arnumber=1055282.

[63] F. Harris, 'On the use of windows for harmonic analysis with the discrete Fourier transform', *Proceedings of the IEEE*, vol. 66, no. 1, pp. 51–83, 1978, ISSN: 0018-9219. DOI: 10.1109/PROC.1978.10837.

[64] A. H. Nuttall, 'Some windows with very good sidelobe behavior', *Acoustics, Speech and Signal Processing, IEEE Transactions on*, vol. 29, no. 1, pp. 84–91, 1981, ISSN: 0096-3518. DOI: 10.1109/TASSP.1981.1163506.

[65] G. Heinzel, A. Rüdiger and R. Schilling, 'Spectrum and spectral density estimation by the Discrete Fourier transform (DFT), including a comprehensive list of window functions and some new flat-top windows', *Max-Planck-Institut für Gravitationsphysik, Hannover*, 15th Feb. 2002. [Online]. Available: http://pubman.mpdl.mpg.de/pubman/faces/viewItemFullPage.jsp?itemId=escidoc:152164:1.

[66] SFF Committee, *INF-8074i Specification for SFP (Small Formfactor Pluggable) Transceiver*, 21st May 2001. [Online]. Available: ftp://ftp.seagate.com/sff/INF-8074.PDF.

[67] ——, *SFF-8477 Specification for Tunable XFP for ITU Frequency Grid Applications*, 4th Dec. 2009. [Online]. Available: ftp://ftp.seagate.com/sff/SFF-8477.PDF.

[68] A. Yariv and P. Yeh, *Photonics - Optical Electronics in Modern Communications*, 6th ed. Oxford University Press, Incorporated, 2007, ISBN: 978-0-195-17946-0.

[69] S.-R. Mun, J.-H. Moon, S.-M. Oh and C.-H. Lee, 'A Self Wavelength Tracking Method for a Cost Effective WDM-PON with Tunable Lasers', in *Optical Fiber Communication Conference*, Optical Society of America, 2010, OWG7. [Online]. Available: http://www.opticsinfobase.org/abstract.cfm?URI=OFC-2010-OWG7.

[70] M. Roppelt, K. Grobe, M. Eiselt and J.-P. Elbers, 'Investigation of Wavelength Control Schemes in WDM-PONs', VDE VERLAG GmbH, May 2011. [Online]. Available: http://www.vde-verlag.de/proceedings-de/453346029.html.

[71] S. H. Lee, A. Wonfor, R. V. Penty, I. H. White, G. Busico, R. Cush and M. Wale, 'Self-Configuring Athermal Tunable DS-DBR Laser for Passive Optical Networks', in *Conference on Lasers and Electro-Optics*, Optical Society of America, 2010, CWN5. [Online]. Available: http://www.opticsinfobase.org/abstract.cfm?URI=CLEO-2010-CWN5.

[72] S. Pachnicke, M. Roppelt, A. Wonfor, J. Zhu, R. Penty, M. Eiselt and J.-P. Elbers, 'Centralized, Pilot-Tone-Based Wavelength-Locking for WDMPON with 1 GbE Data Rate', in *Photonic Networks, 14. 2013 ITG Symposium. Proceedings*, May 2013, pp. 1–4.

[73] L. Coldren, G. Fish, Y. Akulova, J. Barton, L. Johansson and C. Coldren, 'Tunable semiconductor lasers: a tutorial', *Lightwave Technology, Journal of*, vol. 22, no. 1, pp. 193–202, Jan. 2004, ISSN: 0733-8724. DOI: 10.1109/JLT.2003.822207.

[74] P. Debernardi, B. Kogel, K. Zogal, P. Meissner, M. Maute, M. Ortsiefer, G. Bohm and M.-C. Amann, 'Modal Properties of Long-Wavelength Tunable MEMS-VCSELs With Curved Mirrors: Comparison of Experiment and Modeling', *Quantum Electronics, IEEE Journal of*, vol. 44, no. 4, pp. 391–399, 2008, ISSN: 0018-9197. DOI: 10.1109/JQE.2007.914773.

[75] Oclaro Inc., *LambdaFLEX iTLA TL5000VCJ Integrable Tunable Laser Assembly with variable output power - Datasheet*, Mar. 2011. [Online]. Available: http://oclaro.com/datasheets/TL5000VCJ_Datasheet_-_D00091-PB_[07].pdf.

[76] JDS Uniphase Corporation, *CW-TOSA Integrable Tunable Laser Assemblies*, 1st Sep. 2011. [Online]. Available: http://www.jdsu.com/productliterature/5205t-5206t-itla-ds-cms-ae.pdf.

[77] D. De Felipe, C. Zawadzki, Z. Zhang, W. Brinker, H. Klein, F. Soares, M. Moehrle, N. Keil and N. Grote, 'Polymer hybrid integrated devices for WDM-PON', in *Opto-Electronics and Communications Conference (OECC), 2012 17th*, 2012, pp. 232–233. DOI: 10.1109/OECC.2012.6276456.

[78] J.-O. Wesström, S. Hammerfeldt, J. Buus, R. Siljan, R. Laroy and H. de Vries, 'Design of a widely tunable modulated grating Y-branch laser using the additive Vernier effect for improved super-mode selection', in *Semiconductor Laser Conference, 2002. IEEE 18th International*, 2002, pp. 99–100. DOI: 10.1109/ISLC.2002.1041137.

[79] Oclaro Inc., 'Tunable Technology - TL3000 DS-DBR', Powerpoint presentation received by e-mail, May 2010.

[80] S. Lee, A. Wonfor, R. Penty, I. White, G. Busico, R. Cush and M. Wale, 'Uncooled DWDM transmission system using tunable laser sources with anti-mode-hop control protocol', in *Photonics Conference (PHO), 2011 IEEE*, Oct. 2011, pp. 218–219. DOI: 10.1109/PHO.2011.6110504.

[81] Finisar Corp., *S7600 Integrable Tunable Laser Assembly Product Specification*, Dec. 2011. [Online]. Available: http://finisar.com/sites/default/files/pdf/7600001-S7600%20Integrable%20Tunable%20Laser%20Assembly-RevB.pdf.

[82] J. Wesström, G. Sarlet, S. Hammerfeldt, L. Lundqvist, P. Szabo and P.-J. Rigole, 'State-of-the-art performance of widely tunable modulated grating Y-branch lasers', in *Optical Fiber Communication Conference*, Optical Society of America, 2004, TuE2. [Online]. Available: http://www.opticsinfobase.org/abstract.cfm?URI=OFC-2004-TuE2.

[83] S. Lee, A. Wonfor, R. Penty, I. White, G. Busico, R. Cush and M. Wale, 'Athermal colourless C-band optical transmitter for passive optical networks', in *Optical Communication (ECOC), 2010 36th European Conference and Exhibition on*, Sep. 2010, pp. 1–3. DOI: 10.1109/ECOC.2010.5621108.

[84] M. Roppelt, F. Pohl, K. Grobe, M. H. Eiselt and J.-P. Elbers, 'Tuning Methods for Uncooled Low-Cost Tunable Lasers in WDM-PON', in *National Fiber Optic Engineers Conference*, Optical Society of America, 2011, NTuB1. [Online]. Available: http://www.opticsinfobase.org/abstract.cfm?URI=NFOEC-2011-NTuB1.

[85] M. Roppelt, M. H. Eiselt, K. Grobe and J.-P. Elbers, 'Tuning of an SG-Y Branch Laser for WDM-PON', in *Optical Fiber Communication Conference*, Optical Society of America, 2012, OW1B.4. [Online]. Available: http://www.opticsinfobase.org/abstract.cfm?URI=OFC-2012-OW1B.4.

[86] ITU-T, *ITU-T G.694.1 - Spectral grids for WDM applications: DWDM frequency grid*, Feb. 2012. [Online]. Available: http://www.itu.int/rec/T-REC-G.694.1-201202-I/en.

[87] M. Eiselt and M. Roppelt, 'An optical frequency locking method and device for optical data transmission', EU Patent EP2573961 A1, 27th Mar. 2013.